

THE UNIVERSITY OF TULSA
THE GRADUATE SCHOOL

MULTIPOINT FLUX APPROXIMATION METHODS FOR A NUMERICAL WELL
TESTING RESERVOIR SIMULATOR

by
Mohammadreza Mohammadnia Firoozabad

A dissertation submitted in partial fulfillment of
the requirements for the degree of Doctor of Philosophy
in the Discipline of Petroleum Engineering

The Graduate School
The University of Tulsa

2017

THE UNIVERSITY OF TULSA
THE GRADUATE SCHOOL

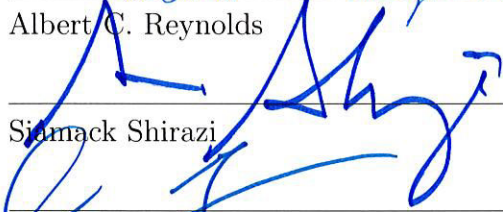
MULTIPOINT FLUX APPROXIMATION METHODS FOR A NUMERICAL WELL
TESTING RESERVOIR SIMULATOR

by
Mohammadreza Mohammadnia Firoozabad

A DISSERTATION
APPROVED FOR THE DISCIPLINE OF
PETROLEUM ENGINEERING

By Dissertation Committee


_____, Chair
Albert C. Reynolds



Siamack Shirazi



Rami Younis



Fahim Forouzanfar

ABSTRACT

Mohammadreza Mohammadnia Firoozabad (Doctor of Philosophy in Petroleum Engineering)

Multipoint flux approximation methods for a numerical well testing reservoir simulator

Directed by Albert C. Reynolds

99+ pp., Chapter 10: Conclusions

(254 words)

In order to match pressure transient data, a simulator must be able to calculate well bottomhole pressures highly accurately. Our objective is to develop discretizations that can be used to develop a thermal compositional simulator sufficiently accurate for well testing purposes. By sufficient accuracy, we mean that the wellbore pressure as a function of time and its derivative computed from the pressure by a standard finite difference approximation would match well with the pressure and its derivative obtained from an analytical solution if they were available. To do so, we develop a new near-well local grid refinement within a base Cartesian grid and design discretization schemes using multipoint flux approximations (MPFA's) to obtain a numerical solution sufficiently accurate for well-test analysis. We establish conditions that guarantee monotonicity for the specific MPFA schemes used. Although monotonicity in and of itself does not guarantee that pressure solutions will not exhibit nonphysical oscillations, monotone schemes do avoid decoupling of the solution which is a major cause of nonphysical oscillations in the pressure solution. Because we use local grid refinement within a Cartesian grid, there exist no previous results on monotonicity that apply directly to our discrete system. Thus, in this work, we derive criteria for discrete monotonicity for the proposed grid system, and then investigate the monotonicity regions of different MPFA methods as functions of permeability anisotropy and

grid geometry properties. To investigate the effects of the violation of a discrete maximum principle, we conduct tests on homogeneous and heterogeneous media, for both isotropic and anisotropic permeability fields. Finally, we demonstrate that second order convergence of the complete numerical scheme can be obtained under appropriate conditions.

ACKNOWLEDGEMENTS

I would like to express my deepest appreciation to my advisor, Dr. Albert C. Reynolds, Jr., Professor of Petroleum Engineering and Mathematical Science at The University of Tulsa, for his constant guidance and encouragement, without which this work would not be possible. I also would like to thank Dr. Fahim Forouzanfar, Dr. Rami Younis and Dr. Siamack Shirazi for serving on my committee. Their comments and suggestion are deeply appreciated. I appreciate Mrs. Judy Teal for helping me with many things during my study at TU.

I gratefully acknowledge financial support from PETROBRAS, the member companies of TUPREP, the Graduate School and Petroleum Engineering department of The University of Tulsa.

I want to Thank all my friends from the Petroleum Engineering department for being there for me. I was lucky to meet all of you.

This work is dedicated to my parents, Mohammad Ali and Sousan, for their unconditional love.

TABLE OF CONTENTS

ABSTRACT	iii
ACKNOWLEDGEMENTS	v
TABLE OF CONTENTS	vii
LIST OF TABLES	viii
LIST OF FIGURES	xii
CHAPTER 1: INTRODUCTION	1
1.1 Literature Review	1
1.2 Research Objectives and Approach	5
CHAPTER 2: GRID REFINEMENT AROUND THE WELL	7
2.1 Radial Grid System	7
2.1.1 <i>Transmissibility Calculations</i>	9
2.2 Well Index Equation	12
2.3 Radial Grid Refinement	13
CHAPTER 3: POLYGONAL NEAR-WELL GRID REFINEMENT	22
CHAPTER 4: MULTIPOINT FLUX APPROXIMATION	28
4.1 Potential Gradient and Flux Approximation	30
4.2 Transmissibility Calculations for the O-method	33
4.3 Transmissibility Calculations for the L-method	40
CHAPTER 5: MONOTONICITY FOR MPFA METHODS	46
5.1 Maximum Principle	47
5.2 Monotonicity Criteria	50
5.2.1 <i>Monotonicity for the O-method</i>	70
5.2.2 <i>Monotonicity for the L-method</i>	71
5.3 Effect of Skin Zone on Monotonicity Regions for the L-method	75
CHAPTER 6: CONVERGENCE AND NUMERICAL TESTS FOR THE L-METHOD	82
6.1 Convergence	82
6.1.1 <i>Boundary Conditions Implementation</i>	84

6.1.2	<i>Analytical Solution</i>	86
6.1.3	<i>Convergence Behavior</i>	89
6.2	Numerical Tests for the L-method	91
CHAPTER 7: CARTESIAN GRID REFINEMENT		95
7.1	Monotonicity Criteria	95
7.2	Convergence	105
7.3	Numerical Tests for the L-method	108
CHAPTER 8: GRID REFINEMENT ACCURACY IN WELL TESTING		115
8.1	Single Phase Production-Buildup	115
8.1.1	<i>Validation with an Analytical Solution</i>	118
8.2	Violation of Monotonicity	119
8.3	Injection-Falloff	120
8.3.1	<i>Single Phase Oil Injection</i>	121
8.3.2	<i>Water Injection</i>	123
8.3.3	<i>Effect of Near-Well Cells</i>	125
8.3.4	<i>CO₂ Injection</i>	125
8.3.5	<i>Violation of Sufficient Monotonicity Criteria</i>	127
CHAPTER 9: SUMMARY AND CONCLUSIONS		130
NOMENCLATURE		132
BIBLIOGRAPHY		132
APPENDIX A: SOLUTION ON LAPLACE'S EQUATION		137

LIST OF TABLES

2.1	The initial reservoir fluid composition at the reference depth.	19
4.1	Assembling the coefficients of two sub-interfaces of area A_1 and A_2	40
5.1	The nonzero entries of the i th row of the matrix A	55
5.2	The nonzero entries of the i th row of the matrix B	56
5.3	Sufficient conditions for $B^{-1} \geq 0$	57
5.4	The nonzero entries of the i th row of the matrix C	58
5.5	Sufficient conditions for $CB^{-1} \geq 0$	60
5.6	Conditions for $A^{-1} \geq 0$	61
7.1	The nonzero entries of the i th row of matrix A	103
7.2	The nonzero entries of the i th row of matrix B	103
7.3	The nonzero entries of the i th row of matrix C	104
8.1	The initial reservoir fluid composition at the reference depth.	121

LIST OF FIGURES

2.1	Well model in radial grid.	13
2.2	Irregularly shaped grid and the fictitious grid.	15
2.3	2 irregularly shaped grids and the fictitious grids.	17
2.4	Permeability approximation in radial grid refinement.	18
2.5	Log-log diagnostic plot of drawdown (left) and buildup (right) data.	20
3.1	Octagonal grid refinement around the well.	23
3.2	Hexadecagonal grid refinement around the well.	24
3.3	Hexadecagonal Grid Structure.	25
3.4	Log-log diagnostic plot of drawdown (left) and buildup (right) data.	26
3.5	Log-log diagnostic plot of drawdown (left) and buildup (right) data.	27
4.1	Two Pairs of K-orthogonal and non-K-orthogonal grid cells.	28
4.2	Triangle ABC with linear potential.	31
4.3	Three possible interaction regions in a hexadecagonal refinement.	34
4.4	Possible interaction regions in the hexadecagonal grid structure.	34
4.5	An interaction region between N grid cells.	35
4.6	The two sub-interfaces between gridblocks 1 and 3.	39
4.7	Possible interaction regions for a sub-interface in the L-method.	41
4.8	The interaction region in the L-method.	42
5.1	Hexadecagonal grid refinement around the well.	51
5.2	Local numbering and the interaction regions (a) for grid cells located in the first and the third quadrants and (b) for grid cells located in the second and the fourth quadrants.	51

5.3	Flow directions through 8 sub-interfaces of cell 1 located in the first and the third quadrants.	52
5.4	A set of irregular hexadecagonal grids for determining transmissibilities for flow into and out of cells $i, i + 1, \dots, i + 15$	54
5.5	Global numbering of a gridblock and its 8 neighboring cells for three different locations in the ring.	55
5.6	Interaction region of four trapezoidal grids.	63
5.7	Interaction region of four trapezoidal gridblocks.	67
5.8	The parameters of the monotonicity criteria for $i \neq 16l, 16l - 15$ as a function of geometric ratio, α , with the permeability ratio of $k_x/k_y = 2$ and $\Delta x/\Delta y = 1$, using the O-method.	72
5.9	The parameter t_5 of criterion $t_5 < 0$ for the last cell in each ring ($i = 16l$) as a function of geometric ratio, α , with $k_x/k_y = 2$ and $\Delta x/\Delta y = 1$, using the O-method.	73
5.10	The parameters of the monotonicity criteria for $i \neq 16l, 16l - 15$ as a function of geometric ratio, α with the permeability ratio of 2 and $\Delta x/\Delta y = 1$, using the L-method.	74
5.11	The parameters of the monotonicity criteria for the last cell in each ring ($i = 16l$) as a function of geometric ratio, α with the permeability ratio of 2 and $\Delta x/\Delta y = 1$, using the L-method.	75
5.12	The parameters of the monotonicity criteria for the first cell in each ring ($i = 16l - 15$) as a function of geometric ratio, α with the permeability ratio of 2 and $\Delta x/\Delta y = 1$, using the L-method.	76
5.13	Monotonicity regions of hexadecagonal grids using the L-method.	77
5.14	A set of irregular hexadecagonal grids with a skin zone shown in grey.	78
5.15	Monotonicity regions of hexadecagonal grids with a skin zone using the L-method.	80
5.16	Monotonicity regions of hexadecagonal grids using the L-method.	81

6.1	An isosceles trapezoidal grid cell	83
6.2	A boundary cell with 8 neighboring cells including 3 imaginary cells.	85
6.3	Convergence behaviour of the L-method, aspect ratio equals 1.	90
6.4	Convergence behaviour of the L-method.	91
6.5	Pressure solutions for grid cells with the aspect ratio of 1 and a geometric ratio of 1.3.	93
6.6	Pressure solutions for grid cells with the aspect ratio of 3 and the geometric ratio of 1.3.	94
6.7	Pressure solutions for grid cells of a heterogenous medium and the geometric ratio of 1.3, $\sqrt{k_x/k_y} = \Delta x/\Delta y$	94
7.1	18 rectangular cells in the x - y plane with y in the vertical direction, (a) before and (b) after refinement.	96
7.2	An interaction region containing three cells.	96
7.3	An interaction region containing four cells.	97
7.4	A cell from category one and its neighboring cells.	100
7.5	A cell from category two and its neighboring cells.	101
7.6	Cartesian grid refinement in the x -direction.	105
7.7	Hybrid grid refinements with (a) 4, (b) 8, (c) 16 and (d) 32 divisions in the θ direction.	106
7.8	A hybrid grid refinement with 16 divisions in the θ direction with the modified boundary.	107
7.9	Convergence behaviour of the L-method, for various values of aspect ratio ($\Delta x/\Delta y$) and permeability ratio (k_x/k_y).	109
7.10	The hybrid grid system with paths emanating from the center.	111
7.11	Pressure solutions for grid cells with the aspect ratio $\Delta x/\Delta y = 1$ and a geometric ratio of $\alpha = r_{i+1/2}/r_{i-1/2} = 1.3$	112
7.12	Pressure solutions for grid cells with the aspect ratio $\Delta x/\Delta y = 3$ and a geometric ratio of $\alpha = r_{i+1/2}/r_{i-1/2} = 1.3$	113

7.13	Pressure solutions for grid cells of a heterogenous medium and the geometric ratio of 1.3, $\sqrt{k_x/k_y} = \Delta x/\Delta y$	114
8.1	Log-log diagnostic plot of drawdown (left) and buildup (right) data.	117
8.2	Complete drawdown period.	119
8.3	Log-log diagnostic plot of drawdown (left) and buildup (right) data.	119
8.4	Log-log diagnostic plot of drawdown (left) and buildup (right) data.	120
8.5	Log-log diagnostic plot of oil injection (left) and falloff (right) data, oil injection into an oil reservoir.	122
8.6	Complete oil injection period.	122
8.7	Log-log diagnostic plot of water injection (left) and falloff (right) data.	123
8.8	Complete water injection period.	124
8.9	Total mobility value of the cells in the first ring around the well as a function of injection time.	125
8.10	Log-log diagnostic plot of water injection (left) and falloff (right) data.	126
8.11	Log-log diagnostic plot of CO ₂ injection (left) and falloff (right) data.	127
8.12	Semi-log plot - CO ₂ injection.	128
8.13	Log-log diagnostic plot of CO ₂ injection (left) and falloff (right) data.	129

CHAPTER 1

INTRODUCTION

Characterizing the physical nature of a subsurface oil reservoir is one of the major problems in petroleum engineering. Pressure transient testing of wells is one of the most common ways to obtain information about the reservoir characteristics. Interpretation of transient well testing pressure or rate data gives an independent evaluation of average in-situ permeability and skin factor. In particular, the assessment of skin factor is important to determine if corrective action (stimulation) may be necessary. Conventional transient well testing analysis assumes single-phase flow in the porous media and is based mostly on analytical or semi-analytical solutions. For general multi-phase flow problems, analytical solutions for the wellbore response during a well test are not available. Thus we propose using a reservoir simulator in place of an analytical solution as a forward model to analyze well-test pressure data by nonlinear regression analysis (history matching). To effectively use a simulator to match pressure transient data, the simulator must be able to generate highly accurate wellbore pressures during the first minutes and hours of the well test. To accomplish this goal, we develop multipoint flux approximations for use in a compositional reservoir simulator with refined polygonal grids around a vertical or horizontal well.

1.1 Literature Review

The three-phase flow of oil, gas and water in a porous-permeable medium can be described by a system of highly nonlinear partial differential equations which apply throughout the spatial domain in which flow occurs [8]. For the problems of interest here, the set of partial differential equations represent the conservation of mass of each chemical species (component) and the conservation of energy [13, 20]. As the governing equations cannot

be solved analytically, they are replaced by discretized equations which are typically derived from the finite-volume approach. To derive the finite-volume equations, the spatial domain is partitioned into gridblocks (cells) and mass conservation and energy conservation are enforced on every gridblock. The constitutive equations represented by Fourier's law of thermal conduction and Darcy's law suitably modified to allow non-Darcy flow in the gas phase [19] are incorporated into the conservation equations. To close the problem, we assume thermodynamic equilibrium on each gridblock at all times, which requires that the fugacity of component i in the oil phase is equal to the fugacity of component i in the gas phase. Initial and boundary conditions are also required to define the final discretized set of equations that represent three-phase flow and transport in a hydrocarbon reservoir. The code that solves the discretized system of equations to obtain an approximation solution, e.g., pressure, temperature, phase compositions and phase saturations at each gridblock, is referred to as a reservoir simulator. In most commercial reservoir simulators, e.g., Eclipse 100 and IMEX [38, 26], the grid is based on corner point geometry.

Virtually all reservoir simulators in existence were developed for field scale simulation of reservoirs containing multiple wells, where wells are incorporated into the simulator using source/sink terms with the relationship between a well's rates, its wellbore pressure and pressure at gridblocks penetrated by the well modeled by a Peaceman equation [33, 34] which does not yield correct solutions at the early times of interest in well testing. When the purpose of reservoir simulation is simply to make correct reservoir management decisions, it is not necessary to calculate wellbore pressures and rates highly accurately. However, to effectively use a simulator to match pressure transient data, which is our objective, the simulator must be able to generate highly accurate wellbore pressures during the first minutes and hours of the well test, in order to be useful for the estimation of reservoir properties by analysis of the well-test pressure data. Generally, the only option for improving the accuracy of wellbore rates and pressures in a commercial simulator is to use a hybrid grid where, in Cartesian gridblocks that are penetrated by a well, a refined r - θ grid is introduced [35]. The r - θ grid enables the replacement of Peaceman's equation by a discretized approximation

of the correct physical boundary condition which applies at the surface area of the wellbore. Unfortunately, as shown in our work, the r - θ refinement introduces other computational inaccuracies which render the radial refinement of limited use when the objective is to develop a reservoir simulator of sufficient accuracy so that it can be used in place of an analytical solution for the analysis of well test data. More specifically, our objective is to develop a reservoir simulator which generates solutions which would match essentially exactly the true analytical solution for wellbore pressures and rates as a function of time. We will refer to a simulator which has this high accuracy as a well-testing reservoir simulator. Of course, the true solution is not known, otherwise, we would not need to build a reservoir simulator. Thus, we can only check the accuracy of our simulator for a limited number of cases.

Bernd Heinrich [24] introduced the method of perpendicular bisectors (PEBI) and Z.E. Heinemann [23] used this method to generate 2D grid cells that conform to the reservoir geometry. In the PEBI method, the connection line between each two neighboring grid center points is perpendicular to the interface of the two cells. This method is theoretically sound for a reservoir with a heterogeneous permeability field provided that the permeability field is isotropic. For anisotropic media, a K-orthogonal grid provides an accurate solution only in the specific case where the permeability ratio (anisotropy ratio) is constant throughout the reservoir and even in this case the permeability ratio needs to be specified prior to grid construction. In K-orthogonal grids, the grid boundaries are specified such that $\mathbf{K} \cdot \vec{n}$ is parallel to the connection line between the two corresponding cell nodes, where, \mathbf{K} is the permeability tensor and \vec{n} is the normal to each cell interface.

To overcome the inadequacy of standard r - θ grid refinement and PEBI grids, we introduce here a near wellbore grid that is similar to an r - θ grid except the circles (or ellipses) are replaced by concentric polygons. When using polyhedral grid cells, we apply a discrete finite-volume formulation using multipoint flux approximations (MPFA's). These methods are also called control-volume distributed (CVD) finite-volume schemes. Different discretization methods for non-K-orthogonal grids with heterogeneous and anisotropic permeability fields were introduced by I Aavatsmark et al. [1] and Michael G Edwards et al.

[14], independently, and later, studied in depth by I Aavatsmark et al. [2] and Michael G Edwards et al. [15]. The basic O-method, which is the most popular MPFA method, requires continuity of flux and potential at the cell interfaces and uses the edge midpoint as the continuity point for the potential. The (CVD) MPFA methods are classified by the quadrature parameterization which is determined by the points at which we enforce continuity. For the O-methods, the choice of points where pressure continuity is enforced can influence the monotonicity and convergence of the scheme. The resulting set of so-called MPFA-O(η) methods use triangular pressure support (TPS) to approximate the pressure gradient in each subcell and thus, may be referred to an TPS-MPFA method. We show that with TPS-MPFA, we can obtain more accurate well testing solutions than are obtainable with local grid refinement based on an r - θ grid. Moreover, unlike the two-point flux approximations commonly used with the r - θ grid, MPFA schemes apply when the permeability field is anisotropic and, in fact, can be used when the permeability tensor is non-diagonal. However, it is important to ensure that the MPFA scheme is monotone because monotonicity tends to prevent nonphysical oscillations in the pressure solutions [31] even though monotonicity cannot guarantee that there will be no spurious oscillations in the pressure solution. Michael G Edwards et al. [17] indicated that monotonicity is sufficient to avoid decoupling which can directly lead to nonphysical oscillations in the solution. If the system of linear equations for the MPFA pressure solution involves an M-matrix, then the pressure solution can be guaranteed to be non-oscillatory [16]. While a monotone matrix is not necessarily an M-matrix, a non-monotone matrix cannot be an M-matrix and this provides another reason to establish the monotonicity of an MPFA scheme. While TPS-MPFA type methods, which only have pointwise continuity of pressure, are used in our work, we note that there exist schemes with full-pressure support (FPS) which have full pressure continuity across each interface. The FPS-MPFA schemes appear to be more robust than TPS-MPFA implementations in that FPS-MPFA do not result in extreme nonphysical oscillations in the pressure solution even though they do not necessarily satisfy a maximum principle.

Researchers have proposed different MPFA methods to avoid oscillatory solutions.

Qian-Yong Chen et al. [11] introduced the enriched multipoint flux approximation (EMPFA) for general diffusion problems on polygonal grids. I Aavatsmark et al. [6] proposed a compact MPFA method for quadrilateral grids called the L-method. They showed that the monotonicity regions of the EMPFA and the L-method are larger than the O-methods. Markus Wolff et al. [40] investigated the application of L-method in 3D for two-phase problems. As noted above, [16] presented a new family of CVD (MPFA) schemes with full pressure support (FPS). They showed schemes with (FPS) minimize oscillations in pressure solutions. Sissel Mundal et al. [30] studied the numerical convergence behaviour of different MPFA schemes on anisotropic, heterogeneous, near-well flow using flexible (unstructured) grids. They showed that the two-point flux approximation scheme does not converge for porous media with high anisotropy. However, they observed quadratic convergence for the pressure on logarithmically refined grids, using various MPFA schemes.

Our primary objective is to show that the thermal, compositional reservoir simulator described in [20], can be made sufficiently accurate for well testing purposes via the MPFA-based grid refinement developed here.

1.2 Research Objectives and Approach

As the first part of this work, we will develop a grid structure that satisfies the following objectives:

- 1- Models the near-well phenomena without causing any inconsistency in transmissibility calculations.
- 2- Uses a simple Cartesian grid system as the base coarse grid.
- 3- Causes minimal or no oscillations in the pressure derivatives for well-testing purposes.
- 4- Is robust to high anisotropy and heterogeneity.
- 5- Models the skin zone around the well.
- 6- Improves the computational cost of simulation by:
 - a) Minimizing the total number of grid cells.
 - b) Minimizing the number of cells which uses an MPFA method for transmissibility

calculations.

The grid refinement method we present here is two-and-a-half-dimensional which is sufficient for our purposes, because the simulator in which it is employed only allows wells which are either vertical or horizontal. In this method, the host cell is refined in a two dimensional plane and then it is projected parallel to the well. As a result, grid cell faces are perpendicular to the well direction. To avoid nonphysical oscillations in the discrete solution, we investigate monotonicity properties for different MPFA methods. The monotonicity criteria developed for general quadrilateral grids by J.M. Nordbotten et al. [31] are not applicable for the structure of the grid refinement we present in this work. Therefore, we need to derive criteria for discrete monotonicity for the grid and then investigate the monotonicity regions of different MPFA methods as functions of permeability anisotropy and grid geometry properties. Different discrete maximum principles and their relation to monotonicity have been discussed in previous studies [39, 31]. As we mentioned in Chapter 5, J.M. Nordbotten et al. [31] defined a discrete version of the maximum principle as follows. A discretization method which results in a discrete system of equations satisfies the discrete maximum principle if the system matrix “for any subgrid” with homogeneous Dirichlet boundary conditions is monotone (the inverse matrix is positive). Eirik Keilegavlen et al. [28] claimed that this version of the discrete maximum principle will be stronger compared to another formulation of discrete maximum principle, where only the matrix for the main grid is monotone [28]. In other words, even though none of these two definitions guarantees that there will be no spurious oscillations in the pressure solution, only the discrete version of the maximum principle defined by J.M. Nordbotten et al. [31] is sufficient to avoid decoupling which can directly lead to nonphysical oscillations in the solution and the weak version of the discrete maximum principle, where only the matrix for the main grid is monotone, does not necessarily avoid decoupling. To see the effects of the violation of maximum principle, we conduct tests on homogenous and heterogenous media, for both isotropic and anisotropic permeability fields.

CHAPTER 2

GRID REFINEMENT AROUND THE WELL

2.1 Radial Grid System

In a reservoir with isotropic permeabilities in the areal direction, the flow near a vertical well is predominantly radial. Therefore, a radial grid system can model the near-well flow efficiently and accurately. For radial systems, the size of the grid boundaries increases geometrically according to the following equation.

$$r_{i+\frac{1}{2}} = \alpha r_{i-\frac{1}{2}}, \quad (2.1)$$

where

$$\alpha = \left(\frac{r_{\text{out}}}{r_{\text{in}}} \right)^{\frac{1}{n_r}}, \quad (2.2)$$

n_r is the number of gridblocks in the radial direction, r_{in} is the minimum radius, and r_{out} is the maximum radius. Generally, we set r_{in} equal to the wellbore radius, r_w . However, by doing this, the outer radius of the first ring around the well is specified automatically as αr_w which for cases with high number of rings, is relatively small. In some cases, we specify the first few rings manually and use the outer radius of the last one as r_{in} to specify α . For example, in some well testing cases, well gridbocks with small volumes can cause numerical inaccuracies in pressure analysis. To fix this, we specify the size of the well gridblocks manually and the geometric ratio, α , is defined using the outer radius of the first ring. In the derivation presented here, we consider a gridblock (i, j, k) centering the gridpoint (r_i, θ_j, z_k) where point (r, θ, z) in the gridblock or on its boundary satisfy

$$r_{i-\frac{1}{2}} \leq r \leq r_{i+\frac{1}{2}}, \theta_{j-\frac{1}{2}} \leq \theta \leq \theta_{j+\frac{1}{2}} \text{ and } z_{k-\frac{1}{2}} \leq z \leq z_{k+\frac{1}{2}}. \quad (2.3)$$

In order to determine an approximate definition of r_i , it is reasonable to consider an incompressible fluid and assume only radial flow. Then, there is no pressure changes in the θ and z directions on grid block (i, j, k) . The volumetric average pressure of the gridblock is

$$\begin{aligned}\bar{p} &= \frac{1}{V} \int_V p dV = \frac{2}{(r_{i+\frac{1}{2}}^2 - r_{i-\frac{1}{2}}^2) \Delta\theta_j \Delta z_k} \int_{z_{k-\frac{1}{2}}}^{z_{k+\frac{1}{2}}} \int_{\theta_{j-\frac{1}{2}}}^{\theta_{j+\frac{1}{2}}} \int_{r_{i-\frac{1}{2}}}^{r_{i+\frac{1}{2}}} p(r) r dr d\theta dz \\ &= \frac{2}{(r_{i+\frac{1}{2}}^2 - r_{i-\frac{1}{2}}^2)} \int_{r_{i-\frac{1}{2}}}^{r_{i+\frac{1}{2}}} p(r) r dr,\end{aligned}\tag{2.4}$$

where $\Delta\theta_j = \theta_{j+\frac{1}{2}} - \theta_{j-\frac{1}{2}}$ and $\Delta z_k = z_{k+\frac{1}{2}} - z_{k-\frac{1}{2}}$ is the thickness of the gridblock. In field units, under steady-state pure radial conditions, the radial pressure distribution in the gridblock is

$$p(r) - p_{i-\frac{1}{2}} = \frac{-q\mu}{1.127 \times 10^{-3} k \Delta\theta_j \Delta z_k} \ln \left(\frac{r}{r_{i-\frac{1}{2}}} \right),\tag{2.5}$$

where, $p_{i-\frac{1}{2}}$ is the pressure at $r_{i-\frac{1}{2}}$ and q is positive for injection, i.e., for flow in the positive r -direction and negative for production. Note we have assume here a homogeneous isotropic permeability field. Substituting Eq. 2.5 into Eq. 2.4 gives

$$\bar{p} - p_{i-\frac{1}{2}} = \frac{-2q\mu}{1.127 \times 10^{-3} k \Delta\theta_j \Delta z_k (r_{i+\frac{1}{2}}^2 - r_{i-\frac{1}{2}}^2)} \int_{r_{i-\frac{1}{2}}}^{r_{i+\frac{1}{2}}} \ln \left(\frac{r}{r_{i-\frac{1}{2}}} \right) r dr.\tag{2.6}$$

To compute the integral, in the right hand side of Eq. 2.6, we use integration by part:

$$\int_{r_{i-\frac{1}{2}}}^{r_{i+\frac{1}{2}}} \ln \left(\frac{r}{r_{i-\frac{1}{2}}} \right) r dr = \left[\frac{1}{2} r^2 \ln \left(\frac{r}{r_{i-\frac{1}{2}}} \right) \right]_{r_{i-\frac{1}{2}}}^{r_{i+\frac{1}{2}}} - \int_{r_{i-\frac{1}{2}}}^{r_{i+\frac{1}{2}}} \frac{1}{2} r dr.\tag{2.7}$$

Simplifying Eq. 2.7 leads to

$$\int_{r_{i-\frac{1}{2}}}^{r_{i+\frac{1}{2}}} \ln \left(\frac{r}{r_{i-\frac{1}{2}}} \right) r dr = \frac{1}{2} (r_{i+\frac{1}{2}})^2 \ln \left(\frac{r_{i+\frac{1}{2}}}{r_{i-\frac{1}{2}}} \right) - \frac{1}{4} (r_{i+\frac{1}{2}}^2 - r_{i-\frac{1}{2}}^2).\tag{2.8}$$

By substituting Eq. 2.8 into Eq. 2.6, we have the final equation for the volumetric average pressure of the gridblock:

$$\bar{p} - p_{i-\frac{1}{2}} = \frac{-q\mu}{1.127 \times 10^{-3} k \Delta\theta_j z_k} \left[\frac{r_{i+\frac{1}{2}}^2}{r_{i+\frac{1}{2}}^2 - r_{i-\frac{1}{2}}^2} \ln \left(\frac{r_{i+\frac{1}{2}}}{r_{i-\frac{1}{2}}} \right) - \frac{1}{2} \right]. \quad (2.9)$$

If we assume that the pressure at r_i is equal to the volumetrically averaged pressure of the gridblock (i.e., $p(r_i) = \bar{p}$), then Eq. 2.5 leads to

$$\bar{p} - p_{i-\frac{1}{2}} = \frac{-q\mu}{1.127 \times 10^{-3} k \Delta\theta_j z_k} \ln \left(\frac{r_i}{r_{i-\frac{1}{2}}} \right). \quad (2.10)$$

By comparing Eqs. 2.9 and 2.10,

$$\ln \left(\frac{r_i}{r_{i-\frac{1}{2}}} \right) = \frac{r_{i+\frac{1}{2}}^2}{r_{i+\frac{1}{2}}^2 - r_{i-\frac{1}{2}}^2} \ln \left(\frac{r_{i+\frac{1}{2}}}{r_{i-\frac{1}{2}}} \right) - \frac{1}{2}. \quad (2.11)$$

and by using the definition of α from Eq 2.1, Eq. 2.11 can be simplified to

$$\ln \left(\frac{r_i}{r_{i-\frac{1}{2}}} \right) = \frac{\alpha^2}{\alpha^2 - 1} \ln(\alpha) - \frac{1}{2}. \quad (2.12)$$

Then, the radius of the grid point is

$$r_i = r_{i-\frac{1}{2}} \exp \left(\frac{\alpha^2}{\alpha^2 - 1} \ln(\alpha) - \frac{1}{2} \right). \quad (2.13)$$

2.1.1 Transmissibility Calculations

In transmissibility calculations for radial grids, it is assumed that the components of the permeability tensor are in the r , θ and z directions. That is, the permeability tensor \mathbf{K} is diagonal with its diagonal entries equal to k_r , k_θ and k_z . The flow rate out of a gridblock boundaries across any surface A can be expressed in an integral form as

$$q = -1.127 \times 10^{-3} \iint_A \frac{\mathbf{K}}{\mu} \nabla \Phi \cdot \vec{n} dA, \quad (2.14)$$

where \vec{n} is the unit outward normal to A . To calculate the flow rate between gridblocks (i, j, k) and $(i + 1, j, k)$, we assume that the flow in the radial direction is constant through any cross sectional area $r\Delta\theta_j\Delta z_k$. Thus, the flowrate for a single-phase flow, through cross sectional area $r\Delta\theta_j\Delta z_k$, is

$$q_r = q_r(r, \theta_j, z_k) = -1.127 \times 10^{-3} \frac{k_r(r, \theta_j, z_k)}{\mu} r \Delta\theta_j \Delta z_k \left. \frac{\partial\Phi}{\partial r} \right|_r, \quad (2.15)$$

where $\frac{\partial\Phi}{\partial r}$ is the potential gradient in the r-direction. By rearranging and integrating Eq. 2.15 from r_i to r_{i+1} , the flow rate between gridblocks (i, j, k) and $(i + 1, j, k)$ is

$$q_{i+\frac{1}{2},j,k} = q(r_{i+\frac{1}{2}}, \theta_j, z_k) = -1.127 \times 10^{-3} \frac{1}{\mu} \frac{\Delta\theta_j \Delta z_k (\Phi_{i+1,j,k} - \Phi_{i,j,k})}{\frac{1}{k_{r,i,j,k}} \ln \frac{r_{i+\frac{1}{2}}}{r_i} + \frac{1}{k_{r,i+1,j,k}} \ln \frac{r_{i+1}}{r_{i+\frac{1}{2}}}}. \quad (2.16)$$

The transmissibility coefficient between gridblocks (i, j, k) and $(i + 1, j, k)$ must be defined such that

$$q_{i+\frac{1}{2},j,k} = -T_{i+\frac{1}{2},j,k} (\Phi_{i+1,j,k} - \Phi_{i,j,k}). \quad (2.17)$$

By comparing Eqs. 2.16 and 2.17, the transmissibility coefficient in the r-direction, related to the interface between the two gridblocks, can be obtained:

$$T_{i+\frac{1}{2},j,k} = \frac{1.127 \times 10^{-3} \Delta\theta_j \Delta z_k}{\mu \left(\frac{1}{k_{r,i,j,k}} \ln \frac{r_{i+\frac{1}{2}}}{r_i} + \frac{1}{k_{r,i+1,j,k}} \ln \frac{r_{i+1}}{r_{i+\frac{1}{2}}} \right)}. \quad (2.18)$$

To find an expression for the transmissibility coefficient in the angular direction, the differential form of Darcy's Law for the velocity in the θ -direction,

$$u_\theta(r) = -1.127 \times 10^{-3} \frac{k_\theta}{\mu} \frac{\partial\Phi}{\partial s} = -1.127 \times 10^{-3} \frac{k_\theta}{\mu} \frac{\partial\Phi}{r \partial\theta}, \quad (2.19)$$

is used. By rearranging and integrating Eq. 2.19 from θ_j to $\theta_{j+\frac{1}{2}}$ and from $\theta_{j+\frac{1}{2}}$ to θ_{j+1} , respectively,

$$1.127 \times 10^{-3} \frac{1}{\mu} \int_{\Phi_{i,j,k}}^{\Phi_{i,j+\frac{1}{2},k}} d\Phi = - \int_{\theta_j}^{\theta_{j+\frac{1}{2}}} \frac{u_\theta(r)r}{k_\theta} d\theta, \quad (2.20)$$

and

$$1.127 \times 10^{-3} \frac{1}{\mu} \int_{\Phi_{i,j+\frac{1}{2},k}}^{\Phi_{i,j+1,k}} d\Phi = - \int_{\theta_{j+\frac{1}{2}}}^{\theta_{j+1}} \frac{u_\theta(r)r}{k} d\theta. \quad (2.21)$$

By combining and rearranging the two equations,

$$u_\theta(r) = - \frac{1.127 \times 10^{-3}}{\mu r} \frac{\Phi_{i,j+1,k} - \Phi_{i,j,k}}{\frac{\theta_{j+\frac{1}{2}} - \theta_j}{k_{\theta,j}} + \frac{\theta_{j+1} - \theta_{j+\frac{1}{2}}}{k_{\theta,j+1}}}. \quad (2.22)$$

The flow rate through the interface between gridblocks (i, j, k) and $(i, j + 1, k)$ is obtained by integrating Eq. 2.22 from $r_{i-1/2}$ to $r_{i+1/2}$ and from $z_{k-1/2}$ to $z_{k+1/2}$:

$$q_{j+\frac{1}{2}} = - \frac{1.127 \times 10^{-3} \ln \left(\frac{r_{i+\frac{1}{2}}}{r_{i-\frac{1}{2}}} \right) \Delta z_k}{\mu \left(\frac{\theta_{j+\frac{1}{2}} - \theta_j}{k_{\theta,i,j,k}} + \frac{\theta_{j+1} - \theta_{j+\frac{1}{2}}}{k_{\theta,i,j+1,k}} \right)} (\Phi_{i,j+1,k} - \Phi_{i,j,k}). \quad (2.23)$$

Therefore, the transmissibility coefficient in the θ -direction can be expressed as

$$T_{i,j+\frac{1}{2},k} = \frac{2 \times 1.127 \times 10^{-3} \ln \left(\frac{r_{i+\frac{1}{2}}}{r_{i-\frac{1}{2}}} \right) \Delta z_k}{\mu \left(\frac{\Delta \theta_j}{k_{\theta,i,j,k}} + \frac{\Delta \theta_{j+1}}{k_{\theta,i,j+1,k}} \right)}. \quad (2.24)$$

According to Eq. 2.14, the vertical flow rate through any cross sectional area with the area of $\frac{\Delta \theta_j}{2} (r_{i+1/2}^2 - r_{i-1/2}^2)$ can be expressed as:

$$q_z = q_z(r_i, \theta_j, z) = -1.127 \times 10^{-3} \frac{\Delta \theta_j (r_{i+\frac{1}{2}}^2 - r_{i-\frac{1}{2}}^2)}{2\mu} k_z \frac{\partial \Phi}{\partial z} \Big|_z. \quad (2.25)$$

By rearranging Eq. 2.25 and integrating from z_k to z_{k+1} , then rearranging again, we find that

$$q_{k+\frac{1}{2}} = -1.127 \times 10^{-3} \frac{\Delta \theta_j (r_{i+\frac{1}{2}}^2 - r_{i-\frac{1}{2}}^2)}{\mu \left(\frac{z_{k+\frac{1}{2}} - z_k}{k_{z,i,j,k}} + \frac{z_{k+1} - z_{k+\frac{1}{2}}}{k_{z,i,j,k+1}} \right)} (\Phi_{i,j,k+1} - \Phi_{i,j,k}). \quad (2.26)$$

Thus, the vertical transmissibility coefficient is expressed by

$$T_{i,j,k+\frac{1}{2}} = \frac{1.127 \times 10^{-3} \Delta\theta_j \left(r_{i+\frac{1}{2}}^2 - r_{i-\frac{1}{2}}^2 \right)}{\mu \left(\frac{z_{k+\frac{1}{2}} - z_k}{k_{z,i,j,k}} + \frac{z_{k+1} - z_{k+\frac{1}{2}}}{k_{z,i,j,k+1}} \right)}. \quad (2.27)$$

2.2 Well Index Equation

The formulation of the well index equation assumes that the flow at the well sandface follows Darcy's law. The general expression for the pressure as a function of radius for incompressible radial flow through a cross sectional area $r\Delta\theta\Delta z$, under pure radial flow conditions is

$$p(r) - p_{wf} = \frac{-q\mu}{1.127 \times 10^{-3} k_r \Delta\theta \Delta z} \ln \left(\frac{r}{r_w} \right), \quad (2.28)$$

where again q is negative for production. In cylindrical grids, the grid point of the inner-most gridblock, grid block $(1, j, k)$, is located where the pressure is equal to the volumetrically averaged pressure of that gridblock (Fig. 2.1), so according to Eq. 2.10 and the fact that

$$r_{1/2} = r_w,$$

$$p_{1,j,k} - p_{wf} = \left(\frac{-q_{1,j,k}\mu}{1.127 \times 10^{-3} \Delta\theta_j \Delta z_k k_{r,1,j,k}} \right) \ln \left(\frac{r_1}{r_w} \right). \quad (2.29)$$

According to Eq. 2.13,

$$r_1 = r_w \exp \left(\frac{\alpha^2}{\alpha^2 - 1} \ln(\alpha) - \frac{1}{2} \right), \quad (2.30)$$

where

$$\alpha = \frac{r_{i+\frac{1}{2}}}{r_{i-\frac{1}{2}}} = \frac{r_{\frac{3}{2}}}{r_w}, \quad (2.31)$$

for all i . The well index (WI) is defined by

$$WI_{1,j,k} = 1.127 \times 10^{-3} \frac{\Delta\theta_j k_{r,1,j,k} \Delta z_k}{\ln \left(\frac{r_1}{r_w} \right)}. \quad (2.32)$$

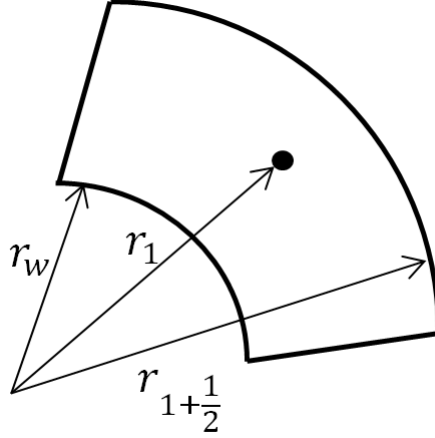


Figure 2.1: Well model in radial grid.

2.3 Radial Grid Refinement

A radial grid system, or more generally, a cylindrical coordinate system can model near-well flow accurately. However, a pure radial grid system cannot be applicable for the entire reservoir, unless the reservoir is cylindrical. [36] used a rectangular grid system with a radial grid refinement around the well to represent flow in the vicinity of the wellbore and in regions far from the well.

Using a hybrid gridblock with a cylindrical grid system around the well creates irregularly shaped grids between the last r - θ gridblock and adjacent Cartesian gridblocks. As shown by the shaded gridblock in Fig. 2.2a, such gridblocks have a curvilinear surface on one side and a flat surface on the other. The basic idea for this procedure is given by [36] and [18].

In order to calculate the transmissibility coefficient at the curvilinear surface in the radial direction between a radial grid and an irregularly shaped grid, the irregularly shaped grid is replaced by a radial grid with the same “angle” and area. Following Eq. 2.13, the radius of the center of the imaginary cell, $r_{n_r+1,j}^*$ is calculated as

$$r_{n_r+1,j}^* = r_{n_r+\frac{1}{2}} \exp \left(\frac{(\alpha_j^*)^2}{(\alpha_j^*)^2 - 1} \ln(\alpha_j^*) - \frac{1}{2} \right), \quad (2.33)$$

where

$$\alpha_j^* = \frac{r_{n_r+\frac{3}{2},j}^*}{r_{n_r+\frac{1}{2}}} \quad (2.34)$$

and $r_{n_r+\frac{3}{2},j}^*$ is the radius of the outer boundary of the imaginary radial gridblock. Here, $j = 1, 2, 3, 4$ specifies the grid cell index in the angular direction. As we showed later, unless the rectangular grid is square ($\Delta l = \Delta w$), the four irregular cells have different areas. Therefore, $r_{n_r+\frac{3}{2},j}^*$ is not necessarily equal for all four cells. The area of the irregularly shaped block is

$$A_j = \frac{\Delta l \Delta w}{4} - \frac{\Delta \theta_j r_{n_r+\frac{1}{2}}^2}{2}, \quad (2.35)$$

where $\Delta \theta_j$ is the angle between the two lines that separate the cell in the angular direction and Δl and Δw are the dimensions of the rectangular gridblock (See Fig. 2.2a). The area of the imaginary radial grid is

$$A_j = \frac{\Delta \theta_j}{2} \left(r_{n_r+\frac{3}{2},j}^{*2} - r_{n_r+\frac{1}{2}}^2 \right). \quad (2.36)$$

By comparing Eqs. 2.35 and 2.36, we compute the radius of the outer boundary of the imaginary radial gridblock:

$$r_{n_r+\frac{3}{2},j}^* = \sqrt{\frac{\Delta l \Delta w}{2 \Delta \theta_j}}. \quad (2.37)$$

Using Eq. 2.18, the transmissibility in the radial direction between the gridblock centered at (n_r, j, k) and the irregular grid block is

$$T_{n_r+\frac{1}{2},j,k} = \frac{1.127 \times 10^{-3} \Delta \theta_j \Delta z_k}{\mu \left(\frac{1}{k_{r,n_r,j,k}} \ln \frac{r_{n_r+\frac{1}{2}}}{r_{n_r}} + \frac{1}{k_{r,n_r+1,j,k}} \ln \frac{r_{n_r+1}^*}{r_{n_r+\frac{1}{2}}} \right)}, \quad (2.38)$$

where $r_{n_r+1}^*$ is given by Eq. 2.40.

To determine the transmissibility in the radial direction at the flat surface of the shaded gridblock, the irregular grid is replaced by an imaginary rectangular grid with the

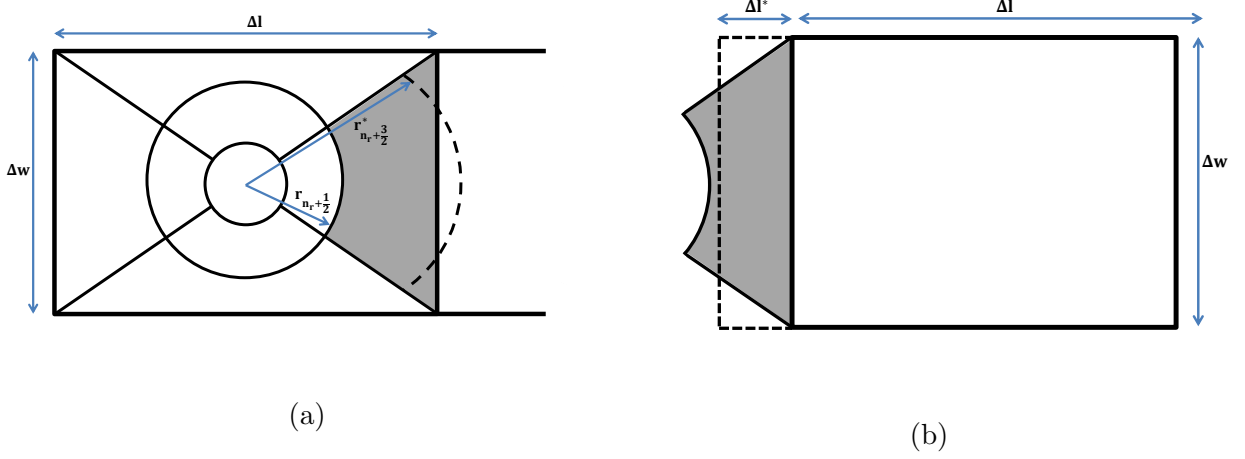


Figure 2.2: Irregularly shaped grid and the fictitious grid.

same area (see Fig. 2.2b). The area of the imaginary rectangular grid is

$$A_j = \Delta l_j^* \Delta w. \quad (2.39)$$

By comparing Eqs. 2.35 and 2.39, we compute the length of the imaginary rectangular grid,

$$\Delta l_j^* = \frac{A_j}{\Delta w} = \frac{\Delta l}{4} - \frac{\Delta \theta_j r_{n_r+\frac{1}{2}}^2}{2\Delta w}. \quad (2.40)$$

We use the transmissibility equation between two rectangular grid cells to calculate the transmissibility between the irregular cell and its neighboring rectangular cell, as follows:

$$T_{n_r+\frac{3}{2},j,k} = \frac{2.254 \times 10^{-3} \Delta w \Delta z_k}{\mu \left(\frac{\Delta l_j^*}{k_{r,n_r+1,j,k}} + \frac{\Delta l}{k_{l,\text{neighbor}}} \right)}. \quad (2.41)$$

where, $k_{l,\text{neighbor}}$ is the permeability of the neighboring rectangular cell in the l direction in the Cartesian coordinate system. Note that in Eq. 2.41, we use $k_{r,n_r+1,j,k}$, which is the permeability of the irregularly shaped cell in the radial direction, as an approximation of the permeability of that cell in the direction of l in the Cartesian coordinate system.

To calculate the transmissibility between two irregularly shaped grids in the θ direction, these two grids are replaced by two imaginary radial grids, shown in Fig. 2.3. The area

of the sum of these two imaginary grids is equal to the total area of the irregularly shaped grids. Since $\Delta\theta_j + \Delta\theta_{j+1} = \pi$, the sum of the area of these two adjacent irregularly shaped blocks is calculated by subtracting the half of the area of the inner circle from the half of the area of the rectangle, as follows:

$$A_{n_r+1,j,k} + A_{n_r+1,j+1,k} = \frac{\Delta w \Delta l}{2} - \frac{\pi r_{n_r+\frac{1}{2}}^2}{2}, \quad (2.42)$$

The sum of the area of the imaginary radial grids is

$$A_{n_r+1,j,k} + A_{n_r+1,j+1,k} = \frac{\pi}{2} \left(r_{n_r+\frac{3}{2}}^{**2} - r_{n_r+\frac{1}{2}}^2 \right). \quad (2.43)$$

By comparing Eqs. 2.42 and 2.43, the radius of the outer boundary of the imaginary grids,

$$r_{n_r+\frac{3}{2}}^{**} = \sqrt{\frac{\Delta w \Delta l}{\pi}}. \quad (2.44)$$

By substituting $r_{n_r+\frac{3}{2}}^{**}$ into Eq. 2.24, the transmissibility in the angular direction between two irregularly shaped gridblocks is

$$T_{n_r+1,j+\frac{1}{2},k} = \frac{2.254 \times 10^{-3} \ln \left(\frac{r_{n_r+\frac{3}{2}}^*}{r_{n_r+\frac{1}{2}}} \right) \Delta z_k}{\mu \left(\frac{\Delta\theta_j}{k_{\theta,n_r+1,j,k}} + \frac{\Delta\theta_{j+1}}{k_{\theta,n_r+1,j+1,k}} \right)}. \quad (2.45)$$

The above method of approximation to calculate the two transmissibilities at the boundaries of the irregularly shaped block considers two different points as the center of the gridblock. These two points cannot both represent the actual center of the irregular grid where the pressure is equal to the volumetrically averaged pressure of the gridblock. The inconsistency in transmissibility calculations at the boundaries of coarse and refined grids causes problems when used in a reservoir simulator when we wish to obtain numerical solutions that produce pressure and pressure derivatives sufficiently accurate for well testing purposes.

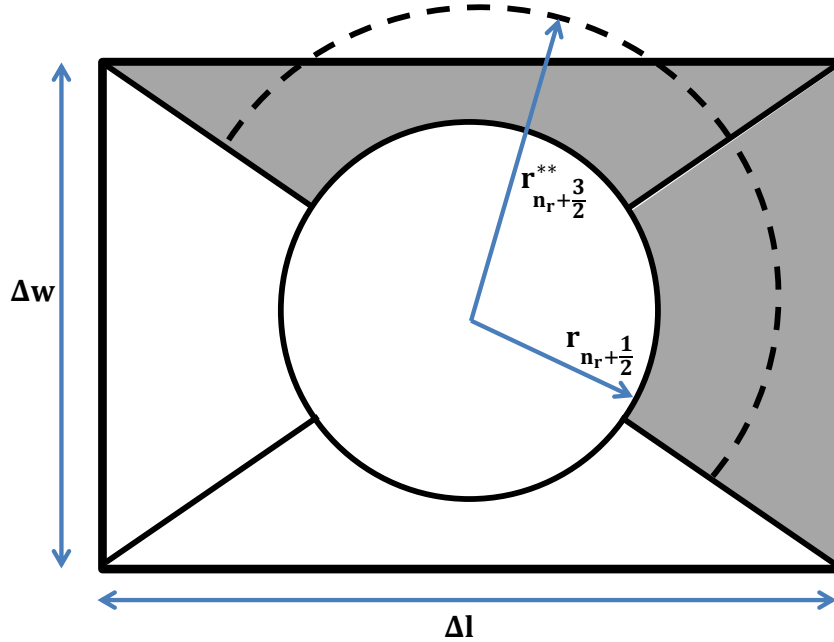


Figure 2.3: 2 irregularly shaped grids and the fictitious grids.

A second major problem of r - θ refinement around a well arises because, in the cylindrical grid system, the principal permeability values are in the radial, angular and vertical directions. However, the principal permeabilities of a fine grid model used for upscaling generally are expressed in Cartesian coordinates. In order to use a radial grid refinement around the well, the principal permeability values have to be transformed to the permeability values in the r, θ and z directions. If the permeability field is isotropic, it is unchanged by the transformation. However if the permeability field is anisotropic in planes perpendicular to the wellbore, even if the permeability is a tensor where all the off-diagonal components are zero, this transformation can cause inaccuracies in the transmissibility calculations. This lack of accuracy in transmissibilities can introduce a significant error in the simulation of anisotropic reservoirs [36].

To illustrate the problem introduced by r - θ refinement when permeability is anisotropic in the r - θ plane, we assume that the r - θ plane coincides with the x - y plane as shown in Fig. 2.4, where the grid only contains four refinements in the θ -direction. In this case, we

can approximate k_r and k_θ as shown in Fig. 2.4. Specifically, we calculate the permeability values in the r and θ directions, based on the number of refinements in the angular direction. In Fig. 2.4, if the line connecting the well to the center of the grid is in the x-direction, then

$$k_r = k_x, \text{ and } k_\theta = k_y. \quad (2.46)$$

This approximate procedure for assigning k_r and k_θ based on k_x and k_y becomes completely unrealistic if, for example, we use 16 divisions (grid refinements) in the θ -direction as we do for the MPFA methods introduced later.

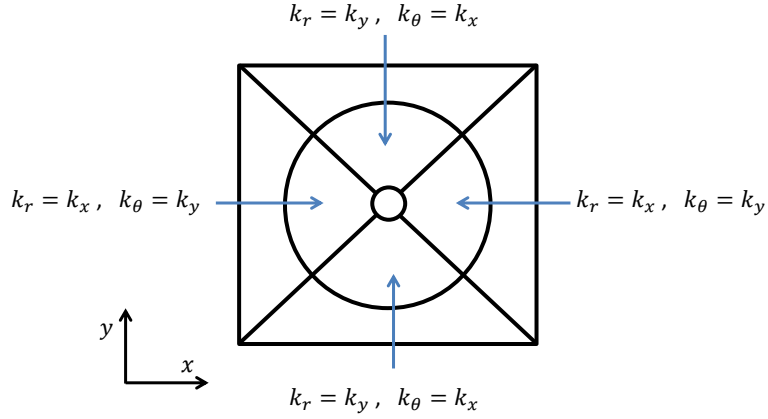


Figure 2.4: Permeability approximation in radial grid refinement.

In a radial grid without any angular division, we specify the permeability value in the r direction using the geometric mean of the permeability values in the x and y directions, i.e.,

$$k_r = \sqrt{k_x k_y}. \quad (2.47)$$

The Eclipse 300 simulator [38] uses a similar approach described here to calculate the transmissibility between the irregularly shaped grid and adjacent Cartesian gridblock.

To show the problem, we use this local grid refinement scheme, described here, to approximate the pressure solution for a transient three-dimensional single-phase radial flow problem. We use a Cartesian $11 \times 11 \times 5$ grid with $\Delta x = \Delta y = 600$ ft and $\Delta z = 15$ ft grid

and the well gridblock is refined into 20 rings in the r -direction and 4 slices in the θ -direction, where $\Delta\theta = \frac{\pi}{2}$. A production well with a wellbore radius of 0.5 ft is located in the center of the reservoir. The skin factor is set equal to zero. The initial reservoir pressure at the reference depth (7067.5 ft) is 5500 psi and the composition of the reservoir fluid is given in Table 8.1.

Table 2.1: The initial reservoir fluid composition at the reference depth.

Component	Mole Percent	Component	Mole Percent
N ₂	1.0194	CO ₂	0.2302
C ₁	54.8065	C ₂	8.2977
C ₃	4.4832	IC ₄	0.9975
NC ₄	2.2909	IC ₅	0.8440
NC ₅	1.2606	C ₆₊	25.7700

The well is set to a constant liquid production rate of 1,000 RB/day for one day followed by a two day pressure buildup test. The reservoir fluid is liquid throughout the simulation. The case under study is a 75 ft thick reservoir which is divided into five homogeneous layers with equal thicknesses (15 ft), porosity (0.2) and permeability values (100 md in the x and y directions and 10 md in the z direction). The well is fully penetrating and there is no flow in the vertical direction. In Fig. 2.5, the Δp curve is a log-log plot of Δp which is the difference between the initial reservoir pressure and the bottom hole pressure at the same datum, versus the flowing time. The $d\Delta p/d\ln t$ curve is the derivative of the pressure drop with respect to the natural logarithm of time. Following D. Bourdet et al. [10], it is calculated numerically as follows:

$$\left(\frac{d\Delta p}{d\ln t}\right)_i = \frac{t_i}{t_{i+1} - t_{i-1}} \left(\frac{\Delta p_i - \Delta p_{i-1}}{t_i - t_{i-1}} (t_{i+1} - t_i) + \frac{\Delta p_{i+1} - \Delta p_i}{t_{i+1} - t_i} (t_i - t_{i-1}) \right). \quad (2.48)$$

In the diagnostic plot of buildup data, we plot $\Delta p = p_{ws}(\Delta t) - p_{wf,s}$ and $d\Delta p/d\ln t_e$ versus shut-in time Δt . Here, t_e is Agarwal's equivalent time defined by $t_e = (t\Delta t)/(t + \Delta t)$, where t is the producing time. Throughout, $p_{ws}(\Delta t)$ denotes the shut-in pressure as a function of shut-in time, Δt , and $p_{wf,s}$ denotes the pressure at the instant of shut-in. For a homogeneous reservoir containing a slightly-compressible, constant-compressibility, single-

phase fluid of constant viscosity and a constant rock compressibility, the wellbore pressure during drawdown at time t , $p_{wf}(t)$, is given by

$$p_{wf}(t) = p_i - \frac{162.6qB_o\mu}{kh} \left(\log t + \log \left(\frac{k}{\phi c_t \mu r_w^2} \right) - 3.23 + 0.87s \right), \quad (2.49)$$

where s is the skin factor and, in Eq. 2.49, we assume a thin skin. From Eq. 2.49, it follows that

$$\frac{d(p_i - p_{wf}(t))}{d \ln t} = \frac{70.61qB_o\mu}{kh}. \quad (2.50)$$

The standard log-log diagnostic plot of drawdown/buildup data presented in Fig. 2.5, shows a hump in the pressure derivative curve between 0.4 and 6.0 hours. The radius of investigation for the time period where the hump appears is 228 to 312 ft which are the locations of the inner and outer boundaries of the irregularly shaped block (shaded area in Fig. 2.2). Fig. 2.5 compares $p_{wf}(t)$ computed from Eq. 2.49, the results of our compositional simulator (CS) with r - θ refinement and the results of Eclipse when we use a Cartesian grid with radial grid refinement around the well. In particular, the pressure derivative from both reservoir simulators indicates that Eclipse result and our CS result are in good agreement but fail to match the solution of Eq. 2.49. The lack of agreement between the simulators and the correct pressure derivative is due directly to the way the transmissibilities for irregularly shaped grids are calculated.

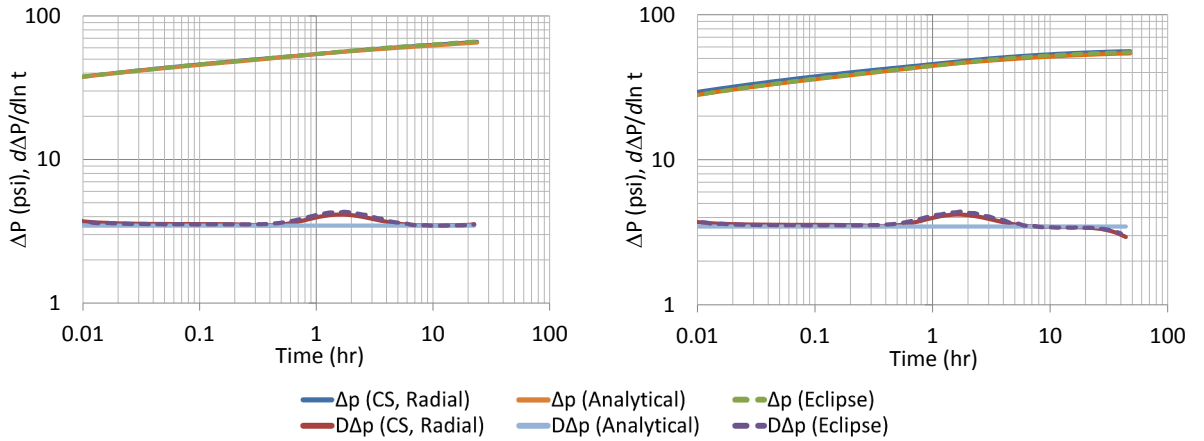


Figure 2.5: Log-log diagnostic plot of drawdown (left) and buildup (right) data.

For this example, we can minimize the oscillation in the pressure derivative curve, by adjusting the number of rings, inner radius of the first ring and outer radius of the last ring. However, we cannot remove the oscillation from the pressure derivative curve and it will always be non-negligible.

CHAPTER 3

POLYGONAL NEAR-WELL GRID REFINEMENT

In order to model the near-well phenomena efficiently without causing any inconsistency in transmissibility calculations, a polygonal grid is used to refine the grid around the well. The base coarse grid and its neighboring grids, are a set of rectangular gridblocks, shown with bold lines in Figs. 3.1 and 3.2. In the grid refinement procedures presented in this work, we refine the coarse well gridblock and its 8 coarse rectangular neighboring gridblocks. Two types of grid structures have been proposed in this refinement method. In the first type, the host cell is refined into a set of irregular octagons as shown in Fig. 3.1. Each adjacent rectangular grid block is refined into nine rectangular grids. In order to keep the size of all nine rectangular fine grids equal, we have to modify the structure of the octagonal grids. We create these octagons in such a way that each side of a host cell, containing an octagonal refinement, is separated into three equal parts. Let's call the 8 coarse rectangular cells around the well gridblock as ring 1 and the next 12 cells around the cells in ring 1 as ring 2. These 12 cells are not shown in the figure. As shown in Fig. 3.1, after refining each rectangular neighboring gridblock, located in ring 1, into 9 refined rectangular cells, each outer boundary of these 8 coarse cells is divided into 3 parts. This means that the other coarse gridblocks in ring 2 that share a boundary with gridblocks in ring 1, now are connected to three refined rectangular cells. Thus, this type of grid structure connects a grid to three refined Cartesian grids. Consequently, the size of the outermost refined grid cell is one-ninth of the size of the adjacent coarse rectangular grid.

In the MPFA technique, it is assumed that potential gradient in each grid cell is constant. Therefore, increasing the number of refinements in the angular direction represents the radial behavior of flow near the well more accurately. In the second type, we

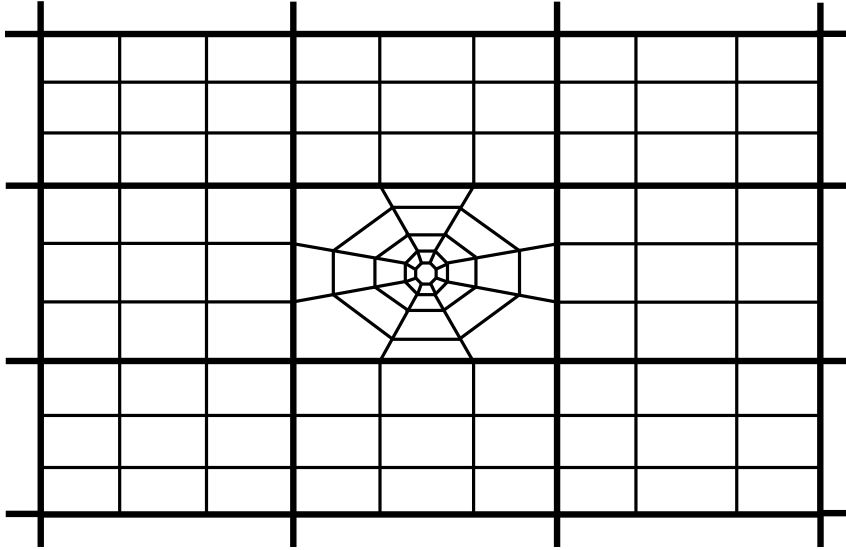


Figure 3.1: Octagonal grid refinement around the well.

consider a hexadecagonal grid refinement where the well grid cell is refined into a set of irregular hexadecagons (16-sided polygons). Note that the area between each two adjacent hexadecagons is divided into 16 trapezoidal grids. Here, we refine the coarse well grid block and its 8 coarse neighboring gridblocks. Each rectangular gridblock, that is adjacent to a well gridblock containing a hexadecagonal refinement, is refined into a set of rectangular grids, as shown in Fig. 3.2. Each base Cartesian gridblock adjacent to a well gridblock that lies immediately east, west, north or south if the well gridblock is divided into ten gridblocks. A base Cartesian gridblock immediately northeast, northwest, southeast or southwest of the well gridblock is subdivided into seven rectangular gridblocks; see Fig. 3.2. The other coarse base gridblocks (not shown in Fig. 3.2) are not refined. In this grid refinement technique, even with a square host cell, the 16 trapezoidal grids between two adjacent hexadecagons are not of equal area. This refinement was chosen because it can accurately approximate r - θ refinement, mitigate the numerical errors that arise when r - θ refinement is applied within a Cartesian grid and at the same time, the numerical errors can be reduced because MPFA can be used with a polygonal grid but cannot be used with an r - θ grid. We use an example later to show that the octagonal refinement is inferior to hexadecagonal refinement and all work presented here, is based on the hexadecagonal refinement.

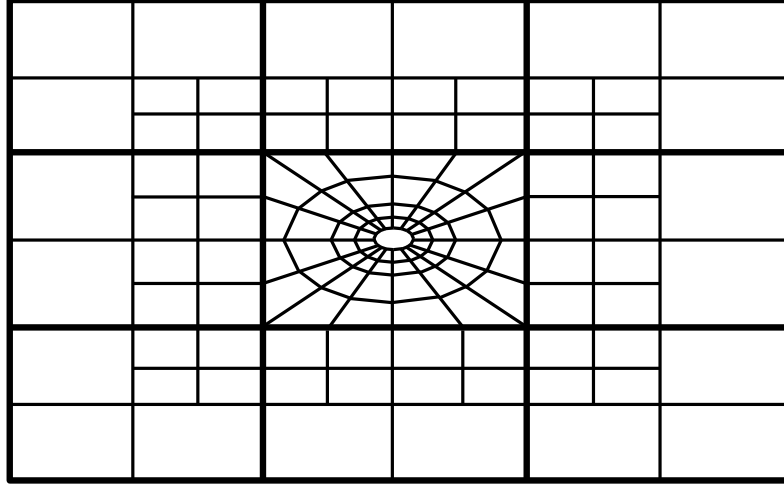


Figure 3.2: Hexadecagonal grid refinement around the well.

Two-dimensional flow near a point source well in an infinite-acting anisotropic porous medium has elliptical equipotential curves. Therefore, adjusting the structure of hexadecagonal grids based on the near-well elliptical flow pattern is expected to simulate the flow behavior more accurately. To modify the grid to conform to “elliptical flow,” each hexadecagon is generated in such a way that all 16 vertices are located on an ellipse (see Fig. 3.3) given by the following equation.

$$\frac{x^2}{a^2} + \frac{y^2}{b^2} = 1, \quad (3.1)$$

where $a = \frac{1}{2}l_{i+\frac{1}{2}}$, $b = \frac{\Delta y}{\Delta x}a$ and $l_{i+\frac{1}{2}}$ is the length of the i th hexadecagon in the x -direction, i.e., the length of the x -axis of the ellipse in which the hexadecagon is inscribed. The wellbore is replaced by a hexadecagon with the same area, i.e., πr_w^2 . This hexadecagon is also constructed based on an ellipse given by Eq. 3.1.

We define the geometric ratio as $\alpha = l_{i+\frac{1}{2}}/l_{i-\frac{1}{2}}$, and regardless of the value of $\Delta y/\Delta x$, α is calculated as follows:

$$\alpha = \left(\frac{l_{\max}}{l_w} \right)^{\frac{1}{N_r}} = \left(\frac{l_{N_r+\frac{1}{2}}}{l_w} \right)^{\frac{1}{N_r}}, \quad (3.2)$$

where N_r is the number of hexadecagons, l_w is the length of the hexadecagon that represents the wellbore and l_{\max} is the length of the last hexadecagon. l_{\max} is calculated in such a way

that an ellipse given by Eq. 3.1 with $a_{N_r+\frac{3}{2}} = \frac{1}{2}\alpha l_{\max}$ and $b_{N_r+\frac{3}{2}} = \frac{\Delta y}{\Delta x} a_{N_r+\frac{3}{2}}$ has the same area as the Cartesian cell containing the well, i.e.,

$$\pi a_{N_r+\frac{3}{2}} b_{N_r+\frac{3}{2}} = \Delta x \Delta y. \quad (3.3)$$

In this way, the area between the last hexadecagon and the boundaries of the Cartesian cell is equal to the area between the last hexadecagon and an imaginary hexadecagon with $l_{N_r+\frac{3}{2}} = \alpha l_{\max}$. To calculate l_{\max} , we rewrite Eq. 3.3 as $\pi a_{N_r+\frac{3}{2}}^2 = \Delta x^2$ and since $a_{N_r+\frac{3}{2}} = \frac{1}{2}\alpha l_{\max}$, the length of the last hexadecagon can be written as a function of Δx , i.e.,

$$l_{\max} = \frac{2\Delta x}{\alpha\sqrt{\pi}}. \quad (3.4)$$

Substituting Eq. 3.4 into Eq. 3.2 yields

$$\alpha = \left(\frac{2\Delta x}{\sqrt{\pi} l_w} \right)^{\frac{1}{N_r+1}}. \quad (3.5)$$

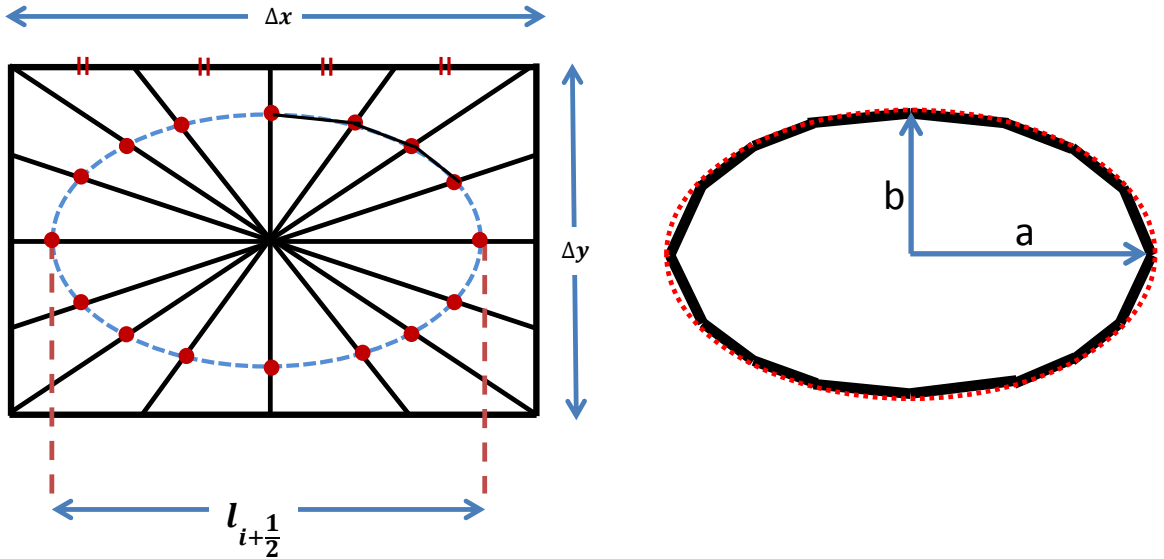


Figure 3.3: Hexadecagonal Grid Structure.

As discussed in detail later, if the well is vertical and the k_x and k_y of a refined

gridblock are known, it is optional to choose Δx and Δy of the base coarse Cartesian grid so that

$$\frac{k_x}{\Delta x^2} = \frac{k_y}{\Delta y^2}. \quad (3.6)$$

If $k_x = k_y = k$, then it is appropriate to use $\Delta x = \Delta y$ and the ellipses become circles. Now we consider the same drawdown-buildup test example considered before but we now use a hexadecagonal refinement system with the MPFA scheme introduced later and Δx and Δy are chosen so that Eq.3.6 holds where $k_x = k_y = 100$ md. Numerical results from the simulator using this refinement method are compared with the one using radial grid refinement. Similar to the previous example, the reservoir is homogenous and isotropic and the reservoir model is a Cartesian $11 \times 11 \times 5$ grid with $\Delta x = \Delta y = 600$ feet and $\Delta z = 15$ ft. The grid cell around the well is replaced by 20 hexadecagonal grids in the radial direction and 16 divisions in the angular direction. The size of the grid boundaries increases geometrically. Each adjacent rectangular gridblock is refined into a set of rectangular grids.

Fig. 3.4 shows the log-log diagnostic plot of drawdown and buildup data. Unlike radial grid refinement, hexadecagonal grid refinement does not create oscillations in the pressure derivatives. Having demonstrated the utility of hexadecagonal refinement within a Cartesian gridblock containing a well, the remainder of the paper is devoted to developing the procedure for calculating the transmissibilities and investigating the monotonicity of the MPFA formulations.

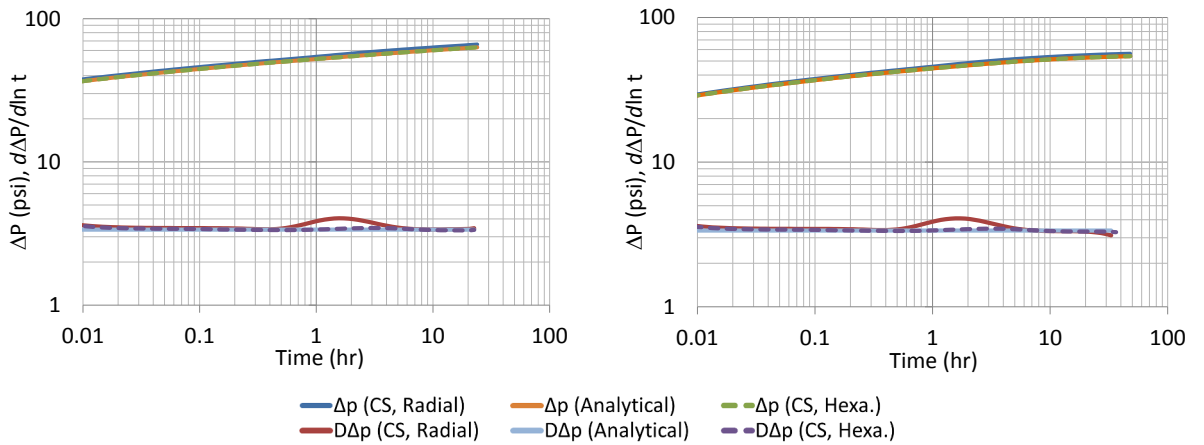


Figure 3.4: Log-log diagnostic plot of drawdown (left) and buildup (right) data.

Fig. 3.5 compares the numerical results of the previous example using the hexadecagonal refinement system with a similar case using an octagonal refinement. The pressure derivative results for the case with hexadecagonal refinement are closer to the analytical solution and in fact the results from the octagonally refined grid, still show a very small pressure hump in the time period from 0.4 to 6.0 hours. Because of this, all results from this point on will consider only the hexadecagonal refinement.

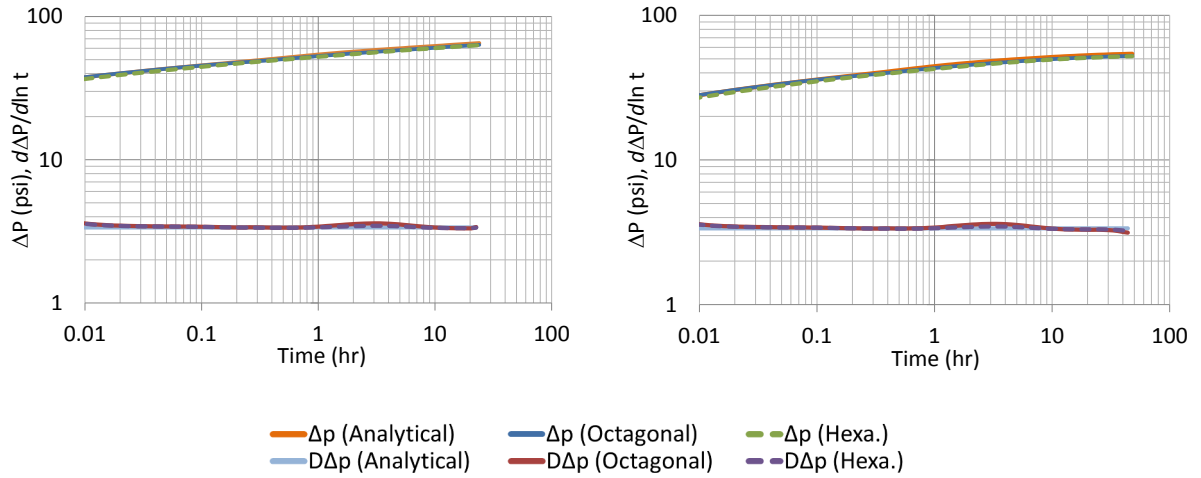


Figure 3.5: Log-log diagnostic plot of drawdown (left) and buildup (right) data.

CHAPTER 4

MULTIPOINT FLUX APPROXIMATION

The two-point flux approximation is the simplest technique to evaluate the flux. This scheme is still used in most commercial reservoir simulators. However, it does not provide accurate and consistent solutions except for K-orthogonal grids where a two-point flux approximation method has an exact solution [3]. Given a permeability tensor \mathbf{K} , K-orthogonal grid is one where the normal, \vec{n} , to each cell interface between any pair of cells, is such that $\mathbf{K} \cdot \vec{n}$ is parallel to the vector joining the two cell nodes. Fig. 4.1 shows two pairs of K-orthogonal and non-K-orthogonal grid cells.

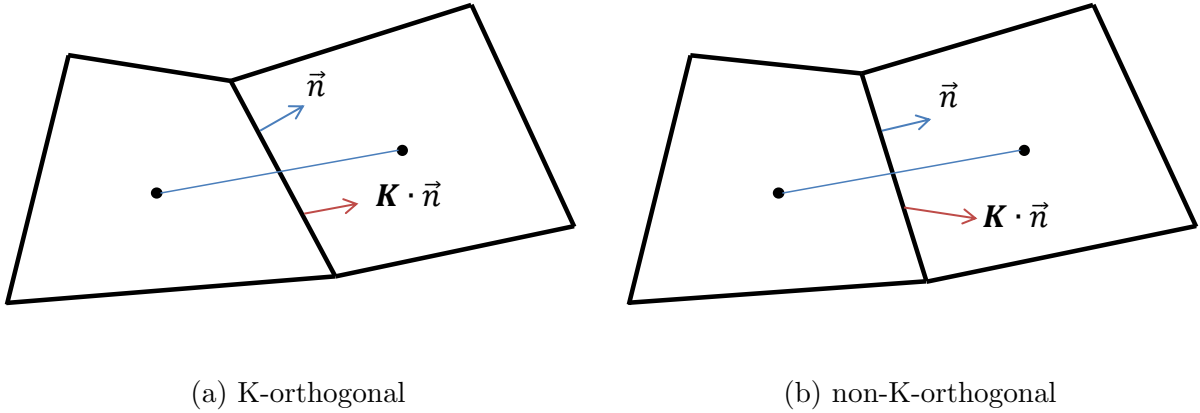


Figure 4.1: Two Pairs of K-orthogonal and non-K-orthogonal grid cells.

For a K-orthogonal grid, the flow across any surface is only a function of potentials at the two cell nodes, i.e., the flow rate of a single-phase fluid between cells i and j can be represented by:

$$q_{ij} = T_{ij}(p_i - p_j), \quad (4.1)$$

where T_{ij} is the transmissibility coefficient between cells i and j . Here, T_{ij} is a function of the permeability values and the geometry of the two cells. A transmissibility formulation for

rectangular cells is given by K. Aziz et al. [9] and a set of transmissibility formulations for a radial grid system can be found in O.A. Petrosa et al. [36]. Following D. Gunasekera et al. [22], the transmissibility between two K-orthogonal cells with indices i and j , with constant anisotropy, in field unit is given by

$$T_{ij} = \frac{1.127 \times 10^{-3} A_{ij}}{\mu \left(\frac{l_i}{\|\mathbf{K}_i \cdot \mathbf{n}_{ij}\|} + \frac{l_j}{\|\mathbf{K}_j \cdot \mathbf{n}_{ij}\|} \right)}, \quad (4.2)$$

where A_{ij} is the area of the cell interface between cells i and j , \mathbf{n}_{ij} is the normal to the cell interface, \mathbf{K}_i and \mathbf{K}_j are the permeability tensors of cells i and j , respectively and l_i and l_j are the distance between the interface and the center of cells i and j along the line that connects the centers of the two cells, respectively. For isotropic reservoirs, i.e. $k_x = k_y$ in each cell, Eq. 4.2 is reduced to the following equation.

$$T_{ij} = \frac{1.127 \times 10^{-3} A_{ij}}{\mu \left(\frac{l_i}{k_i} + \frac{l_j}{k_j} \right)}, \quad (4.3)$$

where k_i and k_j are the permeability values of cells i and j .

It is possible to generate K-orthogonal grids only if the anisotropy ratio is constant throughout the field. For a non-K-orthogonal grid in two spatial dimensions, more than two potential points are necessary to obtain an accurate first-order linear approximation of the potential in each gridblock. Therefore, to discretize the flow equations, more than two grid points are required. A multipoint flux approximation (MPFA) method was introduced by I. Aavatsmark et al. [2] to solve control-volume formulations on polygonal and triangular grid cells in 2D. With MPFA methods more than two pressure points are used for the flux evaluation. Generally, MPFA methods are more accurate but they increase the computational cost of the simulation Q. Y. Chen et al. [12] and can encounter convergence and monotonicity issues. MPFA methods consider anisotropy and general geometry (I. Aavatsmark et al. [2]) and, in fact, can be applied for general permeability tensors. The O-method, which is the most popular MPFA method, assumes the continuity of flux and potential at the cell

interfaces. The basic O-method uses the edge midpoint as the continuity point for the potential. I. Aavatsmark et al. [6] introduced a compact MPFA method for quadrilateral grids called the L-method. This method uses fewer pressure points in transmissibility calculations. They showed that the monotonicity region of the L-method is larger than the monotonicity region for the O-methods and for Cartesian local grid refinements, where the host cells are subdivided into a Cartesian grid of refined cells, the solutions of the L-method provide more accurate solutions for heterogeneous systems than the O-method.

4.1 Potential Gradient and Flux Approximation

The basic assumption of any MPFA method is that the potential gradient $\nabla\Phi$ in each grid is constant. Under this assumption, the potential at any point in gridblock l is given by

$$\Phi_l(x) = \phi_l + (x - x_l) \cdot \nabla\Phi_l, \quad (4.4)$$

where ϕ_l is the value of Φ_l at a point x_l in the gridblock under consideration and $\nabla\Phi_l$ is the constant potential gradient in cell l . Note that in Eq. 4.4 and similar equations that follow the dot denotes the dot (inner) product. Consider two linearly independent vectors $v_{AB} = B - A$ and $v_{AC} = C - A$ (Fig. 4.2). It is assumed that Φ is linear inside the triangle which is created by vectors v_{AB} and v_{AC} (A, B and C are any three non-colinear points all inside or on the boundary of a specific gridblock). Vectors v'_{AB} and v'_{AC} are in the outward direction to the triangle $\triangle ABC$ and v'_{AB} and v'_{AC} respectively are normal to v_{AB} and v_{AC} , with $\|v'_{AB}\|_2 = \|v_{AB}\|_2$ and $\|v'_{AC}\|_2 = \|v_{AC}\|_2$. Because the points A, B and C colinear, the two vectors v'_{AB} and v'_{AC} are linearly independent and may be used as a basis to express the potential gradient vector, i.e.,

$$\nabla\Phi = \alpha v'_{AB} + \beta v'_{AC} \quad (4.5)$$

within the gridblock containing points A, B and C. The potentials at points B and C are

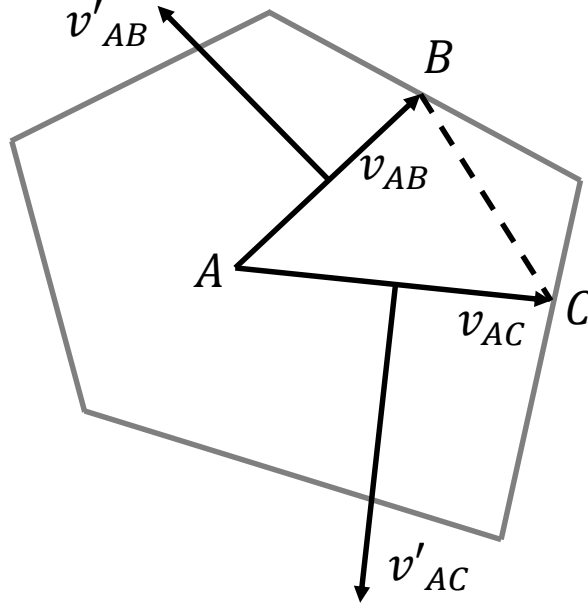


Figure 4.2: Triangle ABC with linear potential.

determined from Eq. 4.4 as follows:

$$\Phi_B = \Phi_A + v_{AB} \cdot \nabla \Phi, \quad (4.6)$$

and

$$\Phi_C = \Phi_A + v_{AC} \cdot \nabla \Phi. \quad (4.7)$$

By substituting the potential gradient from Eq. 4.5 into Eqs. 4.6 and 4.7, rearranging and simplifying using $v_{AB} \cdot v'_{AB} = 0$ and $v_{AC} \cdot v'_{AC} = 0$, we have

$$\Phi_B - \Phi_A = v_{AB} \cdot (\alpha v'_{AB} + \beta v'_{AC}) = \beta v_{AB} \cdot v'_{AC}, \quad (4.8)$$

and

$$\Phi_C - \Phi_A = v_{AC} \cdot (\alpha v'_{AB} + \beta v'_{AC}) = \alpha v_{AC} \cdot v'_{AB}. \quad (4.9)$$

The area of a triangle in two-dimensional space whose vertices are the points A , B and C is calculated as follows: The dot product of two vectors v_{AB} and v'_{AC} is given by

$$v_{AB} \cdot v'_{AC} = \|v_{AB}\| \|v'_{AC}\| \cos(\theta + \pi/2) = \|v_{AB}\| \|v_{AC}\| \cos(\theta + \pi/2), \quad (4.10)$$

where θ is the angle between v_{AB} and v_{AC} . From trigonometric identities we have,

$$\cos(\pi/2 + \theta) = -\sin(\theta). \quad (4.11)$$

By substituting Eq. 4.11 into Eq. 4.10, we have

$$v_{AB} \cdot v'_{AC} = -\|v_{AB}\| \|v_{AC}\| \sin(\theta). \quad (4.12)$$

Using the formula that the area of a triangle is $(1/2)hb$, where h is the height and b is the length of the base, the area of triangle ABC is given by

$$F = \frac{1}{2} \|v_{AB}\| \|v_{AC}\| \sin(\theta). \quad (4.13)$$

Combining Eqs. 4.13 and 4.12, we obtain

$$F = -\frac{1}{2} (v_{AB} \cdot v'_{AC}). \quad (4.14)$$

Similarly, we can show that

$$F = -\frac{1}{2} (v_{AB} \cdot v'_{AC}) = -\frac{1}{2} (v_{AC} \cdot v'_{AB}). \quad (4.15)$$

We substitute Eq. 4.15 into Eqs. 4.8 and 4.9 and rearrange the resulting equations to obtain

$$\alpha = -\frac{\Phi_C - \Phi_A}{2F}, \text{ and } \beta = -\frac{\Phi_B - \Phi_A}{2F}. \quad (4.16)$$

Using Eq. 4.16 in Eq. 4.5, the potential gradient becomes

$$\nabla\Phi = -\frac{\Phi_C - \Phi_A}{2F} v'_{AB} - \frac{\Phi_B - \Phi_A}{2F} v'_{AC}. \quad (4.17)$$

The flowrate from the gridblock l across an interface i of gridblock l may be determined from

$$q_{il} = -n_i^T A_i K_l \nabla \Phi_l, \quad (4.18)$$

where K_l is the absolute permeability tensor of gridblock l , A_i is the area of interface i and n_i is the outward unit normal vector to the interface. By assuming that A, B and C are any three non-colinear points inside the gridblock and using Eq. 4.17, the flowrate equation can be rewritten as

$$\begin{aligned} q_{il} &= -n_i^T A_i K_l \left(-\frac{\Phi_C - \Phi_A}{2F} v'_{AB} - \frac{\Phi_B - \Phi_A}{2F} v'_{AC} \right) \\ &= (n_i^T A_i K_l v'_{AB}) \frac{\Phi_C - \Phi_A}{2F} + (n_i^T A_i K_l v'_{AC}) \frac{\Phi_B - \Phi_A}{2F}. \end{aligned} \quad (4.19)$$

4.2 Transmissibility Calculations for the O-method

We construct an interaction region between a collection of grid cells with one common vertex, by connecting the cell centers of each two neighboring cells through a point on the interface. In the hexadecagonal grid structure, the interaction region can be either between three, four or five grid cells. The examples of the three possible interaction regions are shown in Fig. 4.3. The triangle with dashed sides in Fig. 4.4a shows an interaction region for three grid cells centered P_1, P_2, P_3 where all three gridblocks have a common vertex at the point O . Fig. 4.4b shows an interaction region for four grid cells centered P_1, P_2, P_3 and P_4 and Fig. 4.4c shows an interaction region for five grid cells centered P_1, P_2, P_3, P_4 and P_5 . In these figures, no complete gridblock is shown. In Fig. 4.5, $P_l, l = 1, 2, \dots, N$ represent the centers of N distinct gridblocks. N is the number of gridblocks in the interaction region.

We consider the interaction region between N grid blocks with grid points $P_l, l = 1, 2, \dots, N$. We will need to use the forward integer function $p(l)$ and the backward integer function $m(l)$, where are defined as

$$p(l) = \begin{cases} l + 1 & \text{if } l < N; \\ 1 & \text{if } l = N, \end{cases} \quad (4.20)$$

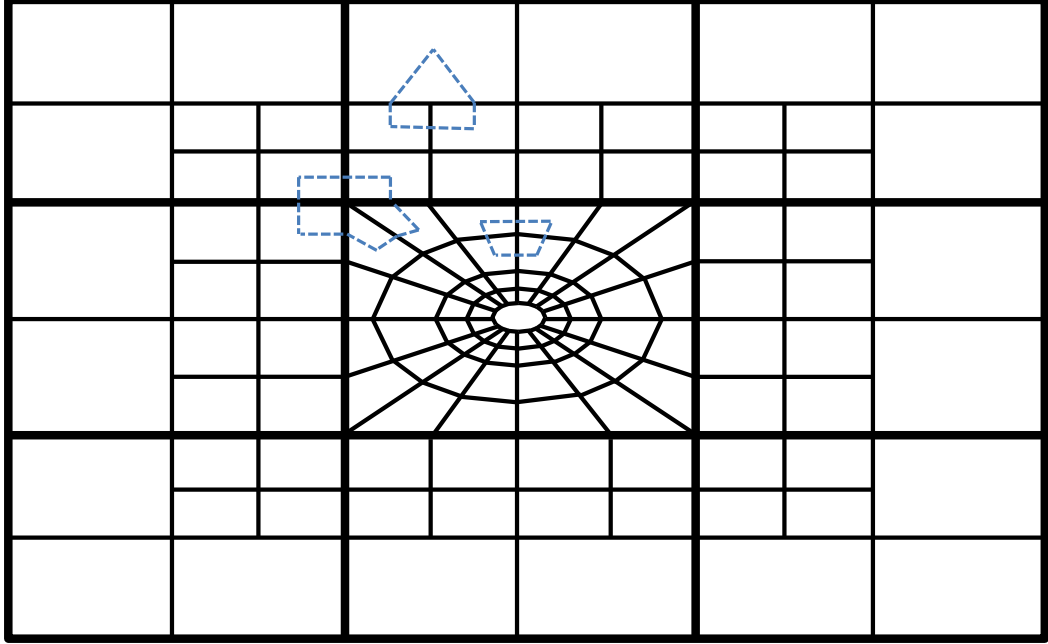


Figure 4.3: Three possible interaction regions in a hexadecagonal refinement.

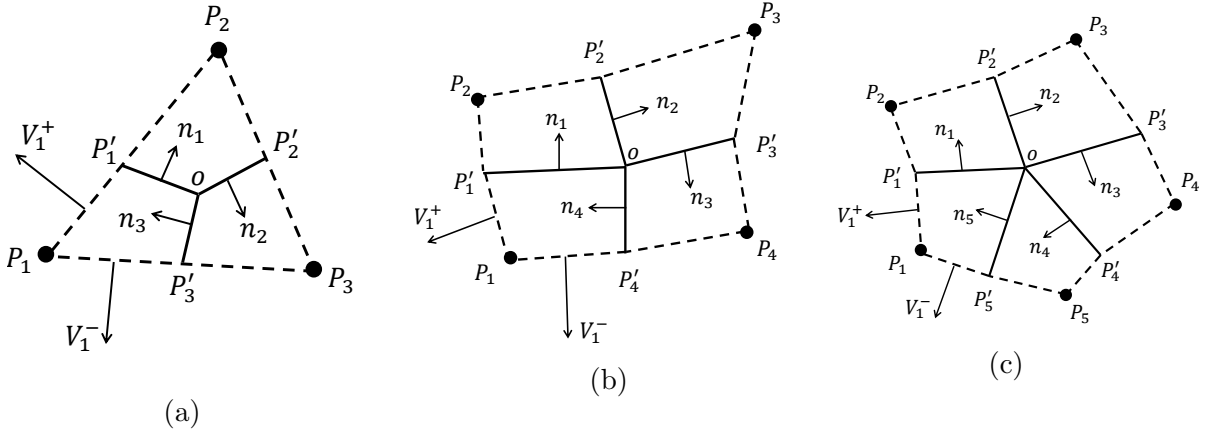


Figure 4.4: Possible interaction regions in the hexadecagonal grid structure.

and

$$m(l) = \begin{cases} l - 1 & \text{if } l > 1; \\ N & \text{if } l = 1, \end{cases} \quad (4.21)$$

where N is the number of grid blocks in the interaction region. It is clear that $m(p(l)) = p(m(l)) = l$.

As mentioned earlier, it is assumed that the potential gradient in each gridblock

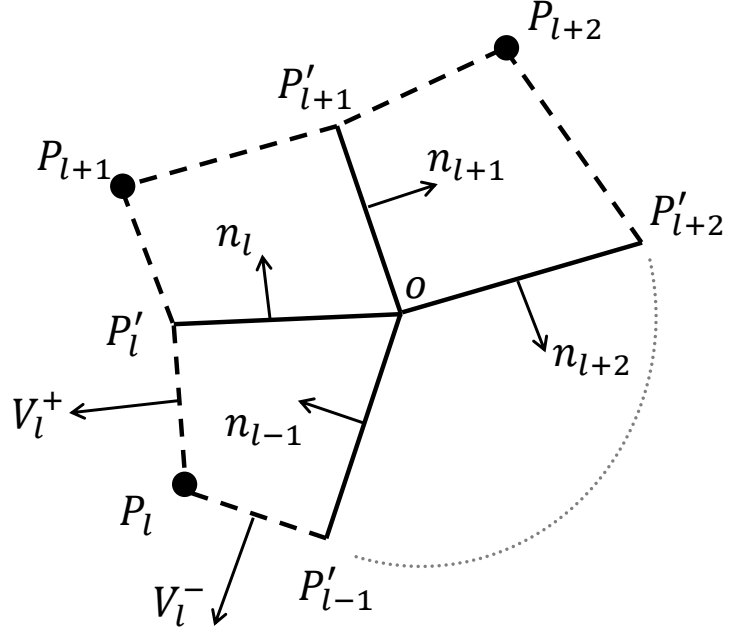


Figure 4.5: An interaction region between N grid cells.

is constant. Since triangle $P_l P'_l P'_{m(l)}$ is located inside gridblock l with a constant pressure gradient, the potential gradient in triangle $P_l P'_l P'_{m(l)}$ is also constant. Comparing this triangle with the triangle ABC in the previous part, we can obtain a similar equation as Eq. 4.17 to approximate the potential gradient.

Vectors v_l^+ and v_l^- are in the outward direction to the triangle $P_l P'_l P'_{m(l)}$ and v_l^+ and v_l^- respectively are normal to $(P'_l - P_l)$ and $(P'_{m(l)} - P_l)$, with $\|v_l^+\| = \|P'_l - P_l\|$ and $\|v_l^-\| = \|P'_{m(l)} - P_l\|$. Using Eq. 4.17, the potential gradient of gridblock l centered at P_l is approximated as

$$\nabla\Phi_l = -\frac{\Phi'_{m(l)} - \Phi_l}{2F_l}v_l^+ - \frac{\Phi'_l - \Phi_l}{2F_l}v_l^-, \quad (4.22)$$

where $\Phi'_{m(l)}$, Φ_l and Φ'_l , respectively, are the potentials at points $P_{m(l)}$, P_l and P'_l , and F_l is the area of the triangle $P'_{m(l)}P_lP'_l$. Similarly to Eq. 4.19, using Eq 4.22 in Eq. 4.18 gives that

the flowrate from/to the gridblock l across the sub-interface i can be determined from

$$q_{il} = (n_i^T A_i K_l v_l^+) \left(\frac{\Phi'_{m(l)} - \Phi_l}{2F_l} \right) + (n_i^T A_i K_l v_l^-) \left(\frac{\Phi'_l - \Phi_l}{2F_l} \right). \quad (4.23)$$

where $l = i, p(i)$. Sub-interface i is a part of the interface between gridblocks $l = i$ and $l = p(i)$, which is located inside the interaction region. The flow through other part of the interface is computed using another interaction region. Note that the flow through the sub-interface i is not necessarily out of the gridblock l . The direction of the flow is determined based on the direction of the normal vector \vec{n}_i . Then, the flow rate through the sub-interface computed based on the pressure gradient of the gridblock on one side of the sub-interface has the same direction as the one computed based on the pressure gradient of the gridblock on the other side. In the approach used in this work, the direction of normal vectors are clock-wise in each interaction region.

We define a new scalar coefficient which is a function of geometry and permeability of the grid, as follows:

$$w_{il}^\pm = \frac{n_i^T A_i K_l v_l^\pm}{2F_l}. \quad (4.24)$$

Then, Eq. 4.23 can be simplified to

$$q_{il} = w_{il}^+ (\Phi'_{m(l)} - \Phi_l) + w_{il}^- (\Phi'_l - \Phi_l). \quad (4.25)$$

The continuity condition is used to eliminate the potentials at the gridblock interfaces from the flowrate equations. From Eq. 4.25, we can calculate the flowrate through sub-interface i using the potential gradients of the two adjacent gridblocks. Since, sub-interface i is between gridblocks $l = i$ and $l = p(i)$, the flowrate continuity equation for sub-interface i can be written as

$$q_{i,i} = q_{i,p(i)}, \quad i = 1, 2, \dots, N. \quad (4.26)$$

By substituting Eq. 4.25 into Eq. 4.26 and rearranging the resulting equation, we obtain

$$\begin{aligned} & w_{ii}^+ \Phi'_{m(i)} + w_{ii}^- \Phi'_i - (w_{ii}^+ + w_{ii}^-) \Phi_i \\ &= w_{i,p(i)}^+ \Phi'_i + w_{i,p(i)}^- \Phi'_{p(i)} - (w_{i,p(i)}^+ + w_{i,p(i)}^-) \Phi_{p(i)}, \end{aligned} \quad (4.27)$$

where $i = 1, 2, \dots, N$. For example, in an interaction region containing four gridblocks ($N = 4$), shown in Fig. 4.4b, the flowrate continuity equation over the interface ($i = 1$) and between gridblocks $l = 1$ and $l = 2$ can be written as follows:

$$q_{1,1} = q_{1,2}. \quad (4.28)$$

Here, both $q_{1,1}$ and $q_{1,2}$ are in the direction of \vec{n}_1 . From Eq. 4.27, the flowrate continuity equation becomes

$$\begin{aligned} & w_{1,1}^+ \Phi'_4 + w_{1,1}^- \Phi'_1 - (w_{1,1}^+ + w_{1,1}^-) \Phi_1 \\ &= w_{1,2}^+ \Phi'_1 + w_{1,2}^- \Phi'_2 - (w_{1,2}^+ + w_{1,2}^-) \Phi_2. \end{aligned} \quad (4.29)$$

Eq. 4.27 holds for all sub-interfaces in the interaction region. If we define $\Phi = (\Phi_1, \Phi_2, \dots, \Phi_N)^T$ and $\Phi' = (\Phi'_1, \Phi'_2, \dots, \Phi'_N)^T$, then the system of Eq. 4.29 for all sub-interfaces in the interaction region becomes

$$A\Phi + B\Phi' = C\Phi + D\Phi', \quad (4.30)$$

where $A = (a_{ij})$, $B = (b_{ij})$, $C = (c_{ij})$ and $D = (d_{ij})$ are $N \times N$ matrices with non-zero components as follows:

$$a_{ii} = - (w_{ii}^+ + w_{ii}^-), \quad (4.31)$$

$$b_{ii} = w_{ii}^-, \quad b_{im(i)} = w_{ii}^+, \quad (4.32)$$

$$c_{ip(i)} = - (w_{ip(i)}^+ + w_{ip(i)}^-), \quad (4.33)$$

and

$$d_{ii} = w_{ip(i)}^+, \quad d_{ip(i)} = w_{ip(i)}^-. \quad (4.34)$$

where $p(i)$ and $m(i)$, respectively, are the forward and the backward integer functions defined earlier in Eqs 4.20 and 4.21. All entries of A , B , C and D not defined by Eqs. 4.31- 4.34 are zero. By rearranging Eq. 4.30 we obtain,

$$\Phi' = (B - D)^{-1}(C - A)\Phi. \quad (4.35)$$

The transmissibility coefficient of the potential of the gridblock l associated with sub-interface i , t_{il} , is defined implicitly by

$$q_i = \sum_{l=1}^N t_{il}\Phi_l, \quad (4.36)$$

where q_i is the flowrate through sub-interface i . If we define $Q = (q_1, q_2, \dots, q_N)^T$, for any interaction region of Fig. 4.4, then we can write a system of Eq. 4.36 as

$$Q = T\Phi, \quad (4.37)$$

where $T = (t_{il})$ is the transmissibility matrix for the interaction region, where element t_{il} is the transmissibility coefficient of the gridblock l associated with sub-interface i . Combining Eqs. 4.30 and 4.37 and rewriting in a matrix form gives

$$\begin{cases} A\Phi + B\Phi' = T\Phi, \\ C\Phi + D\Phi' = T\Phi. \end{cases} \quad (4.38)$$

By substituting Φ' from Eq 4.35 into Eq. 4.38, the transmissibility matrix can be expressed as follows:

$$T = B(B - D)^{-1}(C - A) + A = D(B - D)^{-1}(C - A) + C. \quad (4.39)$$

The transmissibility coefficients for the interfaces are computed by assembling the coefficients of two sub-interfaces (Fig. 4.6). Note that the transmissibility of an interface is not necessarily the summation of two coefficients calculated from each interaction region. For example, in Fig. 4.6, the normal vector of interface 1 (red segment associated with area

A_1 , n_1 , is oriented toward P_1 and the normal vector of interface 2, n_2 , is in the opposite direction. This means the flowrate values calculated for each part of the interface, consisting of the sum of the two sub-interfaces of area A_1 and A_2 , are in the opposite directions. In order to calculate the total flowrate, one set of coefficients has to be subtracted from the other set. For special cases, such as where the interfaces are near the reservoir boundary, the transmissibility coefficients are obtained from only one interaction region. Table 4.1 shows

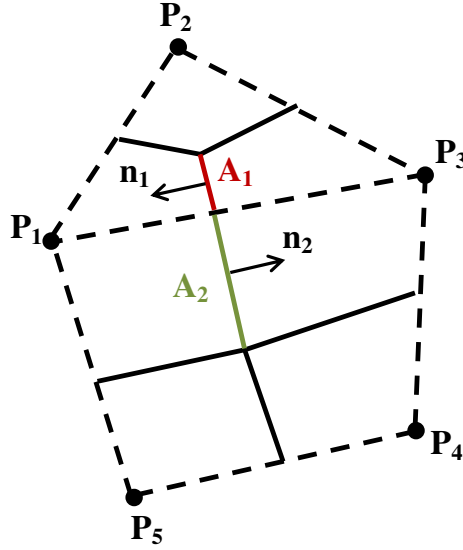


Figure 4.6: The two sub-interfaces between gridblocks 1 and 3.

how to calculate the coefficients of two sub-interfaces from the example in Fig. 4.6. The second and the third columns of this table are the calculated transmissibility coefficients from the first and the second interaction regions. Here, the first interaction region is the triangle with vertices P_1 , P_2 and P_3 and the second interaction region is the quadrilateral with vertices P_1 , P_3 , P_4 and P_5 . The last column is the final transmissibility coefficients used to calculate the flow from gridblock 1 to gridblock 3.

The flow rate from gridblock 1 to gridblock 3 through the interface consisting of the two sub-interfaces with area A_1 and A_2 is

$$q = (-t_{1,1} + t_{2,1})\Phi_1 - t_{1,2}\Phi_2 + (-t_{1,3} + t_{2,3})\Phi_3 + t_{2,4}\Phi_4 + t_{2,5}\Phi_5. \quad (4.40)$$

Table 4.1: Assembling the coefficients of two sub-interfaces of area A_1 and A_2 .

Grid Point Index	Interaction region 1	Interaction region 2	Transmissibility Coefficients
P_1	$t_{1,1}$	$t_{2,1}$	$-t_{1,1} + t_{2,1}$
P_2	$t_{1,2}$		$-t_{1,2}$
P_3	$t_{1,3}$	$t_{2,3}$	$-t_{1,3} + t_{2,3}$
P_4		$t_{2,4}$	$t_{2,4}$
P_5		$t_{2,5}$	$t_{2,5}$

Note that after multiplying the transmissibility coefficients from the first interaction region by (-1), the flow direction through both sub-interfaces is from gridblock 1 to 3. Then, if the flowrate computed from Eq. 4.41 is positive, the direction of the flow is from gridblock 1 to 3. Eq. 4.41 can also be written

$$q = -t_{1,2}(\Phi_2 - \Phi_1) + (-t_{1,3} + t_{2,3})(\Phi_3 - \Phi_1) + t_{2,4}(\Phi_4 - \Phi_1) + t_{2,5}(\Phi_5 - \Phi_1), \quad (4.41)$$

because the summation of transmissibility coefficients,

$$-t_{1,1} + t_{2,1} - t_{1,2} - t_{1,3} + t_{2,3} + t_{2,4} + t_{2,5} = 0. \quad (4.42)$$

4.3 Transmissibility Calculations for the L-method

I. Aavatsmark et al. [6] proposed a compact MPFA method for quadrilateral grids called the L-method. This method uses a similar approach to compute the transmissibility coefficients, as the one discussed previously, but it uses fewer pressure points in transmissibility calculations. Unlike the O-methods, where we use continuity points at the sub-interfaces in the interaction regions, the L-method assumes full potential continuity on the sub-interfaces. Fig. 4.7a shows an interaction region between three cells, in which we wish to compute the transmissibility coefficients, containing two sub-interfaces, shown by the red and blue line segments. The boundaries of the interaction regions are depicted using dashed lines. To specify an interaction region between three cells, each two neighboring cells are connected by a curve that passes through the midpoint of the interface between two cells and the cells along the diagonal are connected by a curve that goes through the common point (vertex)

of the three cells. For each sub-interface, there are two possible interaction regions. Fig. 4.7 shows the two possible interaction regions for the sub-interface between cells 1 and 2, shown by the blue line segment.

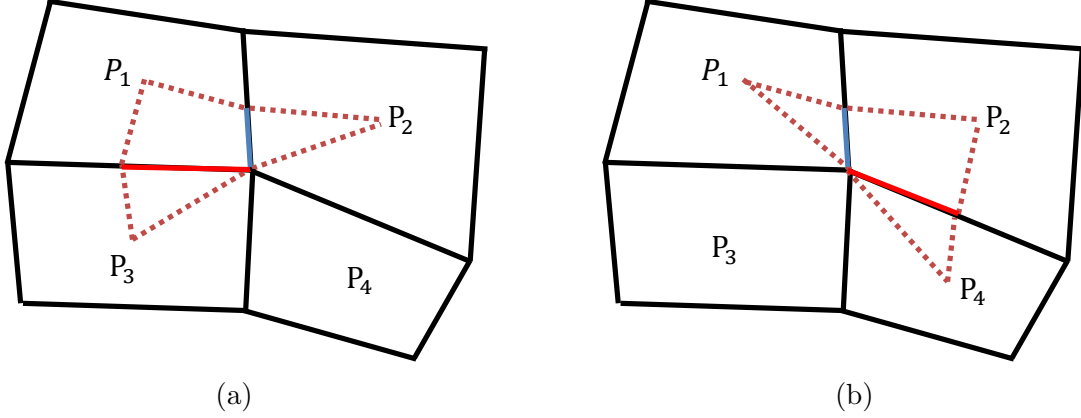


Figure 4.7: Possible interaction regions for a sub-interface in the L-method.

I. Aavatsmark et al. [6] proposed a technique for how to choose the interaction region. First, the transmissibility coefficients of the sub-interface are computed using both possible interaction regions. Interaction regions are labeled based on the cell index of the “middle” cell. For example, the interaction region shown in Fig. 4.7a is labeled as interaction region 1 and the one in Fig. 4.7b is called interaction region 2. The flow rate through the blue sub-interface, shown in Fig. 4.7a, is computed using the interaction region 1:

$$q = t_1\Phi_1 + t_2\Phi_2 + t_3\Phi_3, \quad (4.43)$$

and the flow rate through the blue sub-interface, shown in Fig. 4.7b, is computed using the interaction region 2:

$$q = t'_1\Phi_1 + t'_2\Phi_2 + t'_4\Phi_4, \quad (4.44)$$

where the transmissibility coefficients t_i are computed from interaction region 1 and the transmissibility coefficients t'_i are computed from interaction region 2. To determine which interaction region (1 or 2) should be chosen to compute the transmissibility coefficients for

the blue sub-interface, we compare the absolute values of t_1 and t'_2 . If $t_1 < t'_2$, then we use all the transmissibility coefficients computed from the interaction region 1 for the blue sub-interface, otherwise, we use the coefficients from interaction region 2. Note that this technique choose the interaction region for each sub-interface separately and even though there are two sub-interfaces in each interaction region, if an interaction region is chosen for one sub-interface, it does not mean that the same interaction region is used to compute the transmissibility coefficients for the other sub-interface in that interaction region.

Similar to the O-method, to calculate the transmissibility coefficients of the L-method, we assume that the potential gradient in each cell is constant. Fig. 4.8 shows one of the two possible interaction regions for the L-method. Vectors v_l^+ and v_l^- , for $l = 1, 2, 3$, are defined as normal to $(P'_l - P_l)$ and $(P'_{m(l)} - P_l)$ respectively, with lengths chosen so that $\|v_l^+\| = \|P'_l - P_l\|$ and $\|v_l^-\| = \|P'_{m(l)} - P_l\|$, v_4 is defined as the vector connecting P_1 to P'_2 , i.e., $v_4 = P'_2 - P_1$ and F_l is defined as the area of the triangle $P'_{m(l)}P_lP'_l$ (see Fig. 4.8). Here $m(l)$ is the backward integer function which is defined in Eq. 4.21, where in this case $N = 3$. Then, Eq. 4.22 can be used to approximate the potential gradient of gridblock l .

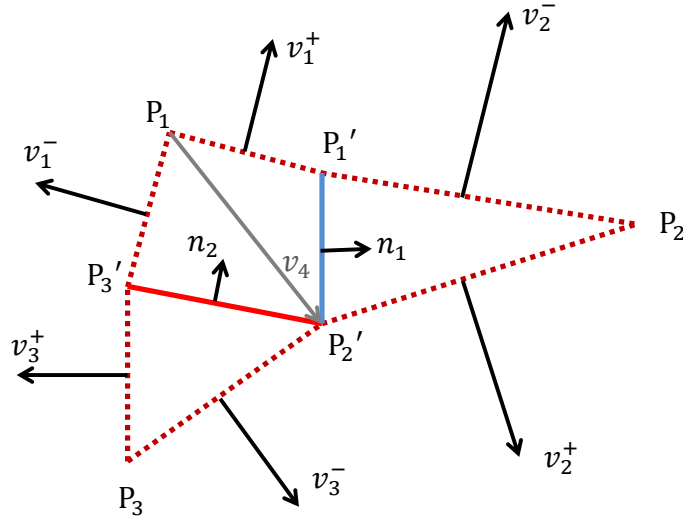


Figure 4.8: The interaction region in the L-method.

We use Eq. 4.25 to determine the flowrate from gridblock l across sub-interface i . Here, n_i is defined as the unit normal vector to sub-interface i , in such a way that n_1 is

toward cell 2 and n_2 is toward cell 1. The flowrate continuity equations for sub-interfaces 1 and 2 respectively are $q_1 = q_{1,1} = q_{1,2}$ and $q_2 = q_{2,1} = q_{2,3}$. Using Eq. 4.25, the two continuity equations can be written as follows:

$$q_1 = q_{1,1} = w_{1,1}^+ \Phi'_3 + w_{1,1}^- \Phi'_1 - (w_{1,1}^+ + w_{1,1}^-) \Phi_1 = w_{1,2}^+ \Phi'_1 + w_{1,2}^- \Phi'_2 - (w_{1,2}^+ + w_{1,2}^-) \Phi_2 = q_{1,2}, \quad (4.45)$$

$$q_2 = q_{2,1} = w_{2,1}^+ \Phi'_3 + w_{2,1}^- \Phi'_1 - (w_{2,1}^+ + w_{2,1}^-) \Phi_1 = w_{2,3}^+ \Phi'_2 + w_{2,3}^- \Phi'_3 - (w_{2,3}^+ + w_{2,3}^-) \Phi_3 = q_{2,3}. \quad (4.46)$$

Since we assume full potential continuity on the sub-interfaces in the L-method, we can calculate the potential at any point on the sub-interface using the potential gradient and the potential at any point in the cell. Then, the potential at P'_2 can be written as a function of the potential at P_1 and the potential gradient in cell 1. Using Eq. 4.6, Φ'_2 is calculated as follows:

$$\Phi'_2 = \Phi_1 + v_4 \cdot \nabla \Phi_1, \quad (4.47)$$

where $\nabla \Phi_1$ is constant throughout the cell containing P_1 . By substituting $\nabla \Phi_1$ from Eq. 4.22 into Eq 4.47, we have:

$$\Phi'_2 = \Phi_1 - v_4 \cdot \left(\frac{\Phi'_3 - \Phi_1}{2F_1} v_1^+ - \frac{\Phi'_1 - \Phi_1}{2F_1} v_1^- \right). \quad (4.48)$$

We introduce a new scalar coefficient which is only a function of geometry, as follows:

$$x^\pm = \frac{v_4 \cdot v_1^\pm}{2F_1}. \quad (4.49)$$

Then, Eq. 4.48 can be simplified to

$$\Phi'_2 = (1 + x^+ + x^-) \Phi_1 - x^+ \Phi'_3 - x^- \Phi'_1. \quad (4.50)$$

Finally, using Eq. 4.50 to eliminate Φ'_2 , the two continuity equations in Eqs. 4.45 and 4.46

can be written as functions of $\Phi_1, \Phi_2, \Phi_3, \Phi'_1$ and Φ'_3 , i.e.,

$$\begin{aligned} & (w_{1,1}^+ + w_{1,2}^- x^+) \Phi'_3 + (w_{1,1}^- + w_{1,2}^- x^- - w_{1,2}^+) \Phi'_1 \\ &= (w_{1,1}^+ + w_{1,1}^- + w_{1,2}^- (1 + x^+ + x^-)) \Phi_1 - (w_{1,2}^+ + w_{1,2}^-) \Phi_2, \end{aligned} \quad (4.51)$$

$$\begin{aligned} & (w_{2,1}^+ + w_{2,3}^+ x^+ - w_{2,3}^-) \Phi'_3 + (w_{2,1}^- + w_{2,3}^+ x^-) \Phi'_1 \\ &= (w_{2,1}^+ + w_{2,1}^- + w_{2,3}^+ (1 + x^+ + x^-)) \Phi_1 - (w_{2,3}^+ + w_{2,3}^-) \Phi_3. \end{aligned} \quad (4.52)$$

We define $\Phi = [\Phi_1, \Phi_2, \Phi_3]^T$ and $\Phi' = [\Phi'_1, \Phi'_3]^T$ to write the two continuity equations of Eqs. 4.51 and 4.52 in matrix form.

$$A\Phi' = B\Phi, \quad (4.53)$$

where,

$$A = \begin{bmatrix} (w_{1,1}^- + w_{1,2}^- x^- - w_{1,2}^+) & (w_{1,1}^+ + w_{1,2}^- x^+) \\ (w_{2,1}^- + w_{2,3}^+ x^-) & (w_{2,1}^+ + w_{2,3}^+ x^+ - w_{2,3}^-) \end{bmatrix}, \quad (4.54)$$

$$B = \begin{bmatrix} (w_{1,1}^+ + w_{1,1}^- + w_{1,2}^- (1 + x^+ + x^-)) & -(w_{1,2}^+ + w_{1,2}^-) & 0 \\ (w_{2,1}^+ + w_{2,1}^- + w_{2,3}^+ (1 + x^+ + x^-)) & 0 & -(w_{2,3}^+ + w_{2,3}^-) \end{bmatrix}. \quad (4.55)$$

By defining $\mathbf{q} = [q_1, q_2]^T$ and considering the left hand sides of Eqs. 4.45 and 4.46, we have

$$\mathbf{q} = C\Phi' + D\Phi, \quad (4.56)$$

where,

$$C = \begin{bmatrix} w_{1,1}^- & w_{1,1}^+ \\ w_{2,1}^- & w_{2,1}^+ \end{bmatrix}, \quad (4.57)$$

$$D = \begin{bmatrix} -(w_{1,1}^+ + w_{1,1}^-) & 0 & 0 \\ -(w_{2,1}^+ + w_{2,1}^-) & 0 & 0 \end{bmatrix}. \quad (4.58)$$

By defining t_{ij} as the transmissibility coefficient of the potential at the grid point in cell j for computing the flowrate through the sub-interface i , the flowrate through sub-interfaces

1 and 2 are calculated as follows:

$$q_i = t_{i1}\Phi_1 + t_{i2}\Phi_2 + t_{i3}\Phi_3, \quad i = 1, 2, \quad (4.59)$$

or in matrix form,

$$\mathbf{q} = T\Phi, \quad (4.60)$$

where,

$$T = \begin{bmatrix} t_{11} & t_{12} & t_{13} \\ t_{21} & t_{22} & t_{23} \end{bmatrix}. \quad (4.61)$$

We assume the matrix A in Eq. 4.53 is nonsingular. Then,

$$\Phi' = A^{-1}B\Phi. \quad (4.62)$$

Substituting Φ' from Eq. 4.62 into Eq. 4.56 yields

$$\mathbf{q} = CA^{-1}B\Phi + D\Phi, \quad (4.63)$$

and it follows that

$$T = CA^{-1}B + D. \quad (4.64)$$

CHAPTER 5

MONOTONICITY FOR MPFA METHODS

Generally, discretized systems of finite volume equations based on multipoint flux approximation techniques are not guaranteed to be monotone. As discussed in the introduction, monotone schemes tend to prevent nonphysical oscillations in the discrete solution even though there is no theoretical guarantee that a monotone MPFA method will not generate spurious oscillations in the pressure solution. In multi-phase flow simulations, such oscillations can result in wrong flux directions and convergence issues in non-linear solvers. Moreover, for a grid cell where the pressure is close to the bubble-point, this problem may lead to a diverging solution due to undesirable phase transitions. E. Keilegavlen et al. [27] claimed that it is only possible to investigate the monotonicity properties theoretically for single-phase flow, but the single-phase flow results can be used in two-phase flow simulations.

MPFA methods are derived under the assumption that the potential gradient in each grid is constant, and when this assumption is valid, the MPFA solution is exact and monotonicity is not relevant. However, in regions where the potential gradient is not constant, MPFA introduces an error that leads to nonphysical oscillatory solutions, and for this reason, it is important to investigate monotonicity.

J.M. Nordbotten et al. [31] developed sufficient monotonicity criteria based on a discrete maximum principle for general quadrilateral grids. They investigated the monotonicity regions of a case with uniform parallelogram grid cells and a homogeneous medium for the class of nine-point schemes as a function of permeability and geometrical properties. E. Keilegavlen et al. [28] proved that the sufficient conditions developed in [31] are also necessary. However, the grid system presented in this work is not covered by the grid structures considered previously by [31, 28]. Specifically, the general approach to establish monotonicity given

by [31], must be customized to account for the grid ordering and to account for the fact that the refined polygonal grid is imbedded in a Cartesian grid so, unlike the cases considered by [31], the aspect ratio $\Delta x/\Delta y$ and the number of rings directly affect the monotonicity conditions, i.e., previous results on monotonicity are not directly applicable for the discrete MPFA used in our work.

5.1 Maximum Principle

Two-dimensional incompressible flow of a single-phase liquid through a porous medium is described by the following partial differential equation:

$$-\nabla \cdot \frac{1}{\mu} (\mathbf{K} \nabla p(x, y)) = q(x, y) \text{ for } (x, y) \text{ in } \Omega \subseteq R^2, \quad (5.1)$$

$$p(x, y) = \gamma(x, y) \text{ in } \partial\Omega, \quad (5.2)$$

where $\partial\Omega$ denotes the boundary of the domain Ω , $\mathbf{K} = \mathbf{K}(x, y)$ is a symmetric permeability tensor, q acts as a source term and the viscosity μ is assumed to be constant. Without loss of generality, we assume $\mu = 1$ for the purposes of our discussion of the maximum (minimum) principle. Also note that Eq. 5.1 neglects the effects of gravity. Theorem 1 which follows is given in [25].

Theorem 1. *Let $u(x)$ be in $C^2(D)$ where the domain D is a open subset of R^n and assume that the following differential inequality is satisfied:*

$$Lu(x) \equiv - \sum_{ij} a_{ij} \frac{\partial^2 u}{\partial x_i \partial x_j} - \sum_j b_j \frac{\partial u}{\partial x_j} \geq 0 \quad (\leq 0) \quad (5.3)$$

for all x in D , where the symmetric matrix $a_{ij} = a_{ij}(x)$ is locally uniformly positive definite in D (that is, for any compact set $D' \subset D$, $\sum_{i,j} a_{ij}(x) \eta_i \eta_j$ is positive and uniformly bounded away 0 for all $x \in D'$ and all $\eta \in R^n$ with $\|\eta\|_2 = 1$) and the coefficients a_{ij} and $b_j = b_j(x)$ are locally bounded (bounded around every point). If u takes on a minimum (maximum)

value M at some x_0 , in D , then $u(x) = M$ for all x in D .

Let ∂D denote the boundary of D and assume u is continuous on $D \cup \partial D$ and that the assumptions of Theorem 1 apply with $Lu \geq 0$. Then the theorem states that u cannot take on a minimum M in the interior of D , unless u is equal to M throughout D , and in this case, u takes on its minimum on ∂D . On the other hand, if u does not take on a minimum at some point in D , then the continuity of u implies that u takes on its global minimum (over $D \cup \partial D$) on ∂D . Similarly if the left hand side of Eq. 5.3 is nonpositive, then u takes on its maximum M on ∂D and if $u(x_0) = M$ at some x_0 in the interior of D , then $u = M$ at all points in D . In the preceding discussion, the word interior is actually superfluous because D is a domain means D is an open connected set.

In the Cartesian coordinate system, the term $\mathbf{K}\nabla p$ in Eq. 5.1 is a vector whose components are

$$\sum_j \mathbf{k}_{ij} \frac{\partial p(x)}{\partial x_j}, \quad (5.4)$$

where the elements of the permeability tensor \mathbf{K} are denoted by \mathbf{k}_{ij} . The left-hand side of Eq. 5.1 (with $\mu = 1$) in a Cartesian coordinate system is given by

$$-\sum_{ij} \mathbf{k}_{ij} \frac{\partial^2 p}{\partial x_j \partial x_i} - \sum_j \left(\sum_i \frac{\partial \mathbf{k}_{ij}}{\partial x_i} \right) \frac{\partial p}{\partial x_j}. \quad (5.5)$$

It follows that Eq. 5.1 can be written as

$$-\sum_{ij} \mathbf{k}_{ij} \frac{\partial^2 p}{\partial x_i \partial x_j} - \sum_j \left(\sum_i \frac{\partial \mathbf{k}_{ij}}{\partial x_i} \right) \frac{\partial p}{\partial x_j} = q. \quad (5.6)$$

Suppose that the source term, $q(x)$, is a non-negative continuous function on the domain Ω and the permeability tensor, \mathbf{K} is symmetric and continuously differentiable in Ω . Then, Theorem 1 implies that the solution $p(x)$ of Eq. 5.6 has no strict local minimum at any x in Ω . This means that there is no point $x_0 \in \Omega$ and domain $\omega \subset \Omega$ such that $p(x_0) < p(x)$ for all other $x \in \omega$, i.e., $p(x)$ has no strict local minima in Ω .

Suppose on an arbitrary domain $\omega \subset \Omega$, we impose zero Dirichlet boundary conditions ($p = 0$ on the boundary of ω) for Eq. 5.1 or equivalently Eq. 5.6. If q is non-negative on ω , then Theorem 1 implies that the solution $p(x)$ of Eq. 5.1 has no minimum in ω and since $p = 0$ on the boundary, the solution p is non-negative in ω . It follows that

$$q \geq 0 \Rightarrow p \geq 0 \quad \text{in } \omega. \quad (5.7)$$

In reservoir simulation, the reservoir is discretized into control volumes and a unique pressure value is assigned to each grid point. For simplicity, let $\Omega \subseteq R^2$. A discrete approximation to Eq. 5.1 defined on a grid $\Omega_h \subseteq \bar{\Omega} = \Omega \cup \partial\Omega$, given zero pressure on the boundary of grid points ($\Omega_h \cap \partial\Omega$), results in a system of linear equations which can be represented by

$$Ap = q, \quad (5.8)$$

where A is the matrix of coefficients, and p and q respectively, represent the column vectors of the pressure and the source/sink terms of the grid cells. Even though Theorem 1 holds for the elliptic equation (Eq. 5.1), there is no guarantee that a discrete version of the maximum (minimum) principle holds for Eq 5.8. However, as discussed below, there exists an analogous discrete maximum (minimum) principle for Eq. 5.8.

Definition 1. A real $n \times n$ matrix B is said to be monotone if for all $x \in R^n$, $Bx \geq 0$ implies $x \geq 0$. It is easy to prove the following theorem.

Theorem 2. *Let B be a nonsingular $n \times n$ matrix then B is monotone if and only if $B^{-1} \geq O$, where O denotes the $n \times n$ null matrix.*

Theorem 2 implies that if A in Eq. 5.8 is monotone, then

$$q \geq 0 \Rightarrow p \geq 0. \quad (5.9)$$

Following J.M. Nordbotten et al. [31], a discrete version of the maximum principle can be stated as follows: Let $Ap = q$ be a discrete approximation to Eq. 5.1 on any subgrid

bounded by a closed Jordan curve with zero pressure specified on the boundary. Then the matrix A must satisfy the monotonicity property ($A^{-1} \geq 0$). In [31], this “discrete maximum principle” is referred to as property MD.

Definition 2. A discretization method which results in a discrete system of equations which satisfies property MD is said to be monotone.

Although, the discrete maximum principle (property MD) is a natural discrete analogue of Theorem 1, there is no proof that property MD guarantees no nonphysical oscillations in the pressure solutions. However, previous studies have shown that monotone schemes tend to prevent spurious oscillations [17, 27].

To satisfy property MD, for any subset of grid points, the matrix A in Eq. 5.8 should be constructed in such a way that $p \geq 0$ whenever $q \geq 0$, or, equivalently, such that $p \geq 0$ whenever $Ap \geq 0$. The definition of a monotone matrix implies that monotonicity of the matrix A for all subgrids with homogenous Dirichlet conditions is a sufficient criterion to ensure that the discrete version of maximum principle is preserved in the discretization.

5.2 Monotonicity Criteria

To study the monotonicity of the MPFA method on the grid structure of Fig. 3.2, we first derive sufficient criteria for discrete monotonicity and then investigate which parameters affect the transmissibility coefficients. Here, we consider a set of irregular hexadecagons where the area between each two adjacent hexadecagons is divided into 16 trapezoidal grids. As in the numerical well testing simulator, permeability heterogeneities are confined to the coarsest Cartesian grid. In particular, k_x and k_y are uniform on the refined grid of each gridblock penetrated by a well where hexadecagonal grid refinement is used, see Fig. 3.2 which is represented here as Fig. 5.1.

Fig. 5.2a shows the local numbering of neighboring cells and four interaction regions for the cell whose center is at the point labeled 1 in the first and the third quadrants of each ring. The neighboring cells do not have to be in the same quadrant as the cell 1. A hexadecagonal structure has two lines of symmetry. In order to keep the local numbering

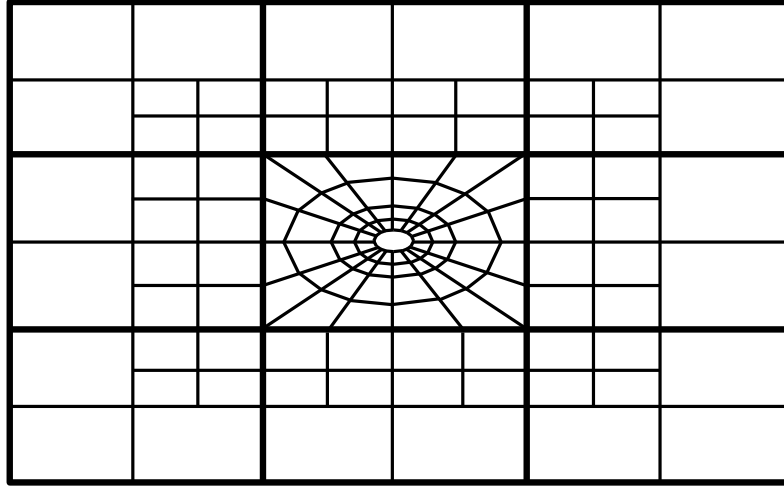


Figure 5.1: Hexadecagonal grid refinement around the well.

consistent with these two lines of symmetry, we use a different local numbering in the second and the fourth quadrants, as shown in Fig. 5.2b. Following these local numberings, for any gridblock in the second, third or fourth quadrant, there is a gridblock in the first quadrant with the exact same transmissibility coefficients. An interaction region between four neighboring grid cells can be constructed by selecting the center of each cell and a point at each interface.

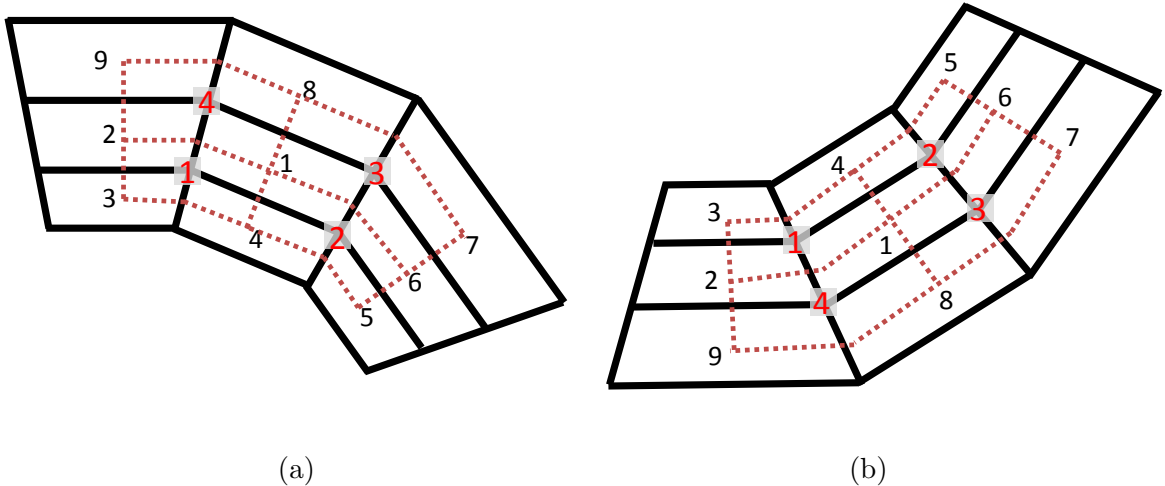


Figure 5.2: Local numbering and the interaction regions (a) for grid cells located in the first and the third quadrants and (b) for grid cells located in the second and the fourth quadrants.

Considering cell 1 in Fig. 5.3, t_j is defined as the transmissibility coefficient of the

potential of gridblock j . The total flux out of cell 1 is calculated as $\sum_{j=1}^9 t_j p_j$, where p_j is the potential of the neighboring cell j of the grid cell 1, and this expression for the total flux includes the flow out of cell 1 through all four of its interfaces. As there is no flow out of cell 1 if the potential of all the nine cells are equal, it follows that the summation of the transmissibility coefficients is equal to zero, i.e., $\sum_{j=1}^9 t_j = 0$. Thus, the flux out of cell 1 through all four boundaries can be written as a function of the potential differences between cell 1 and each neighboring cell, i.e., as $\sum_{j=2}^9 t_j (p_j - p_1)$.

Fig. 5.3 shows the numbering of the 8 sub-interfaces of cell 1 and the direction of the flow through each sub-interface when the flowrate is positive. We define $t_{kj}^{(c)}$ as the transmissibility coefficient of the potential of gridblock j associated with sub-interface k calculated from interaction region c , where k refers to the indices of sub-interfaces depicted by n_k in Fig. 5.3. For example, we use interaction region 1 in Fig. 5.3 to compute the flux

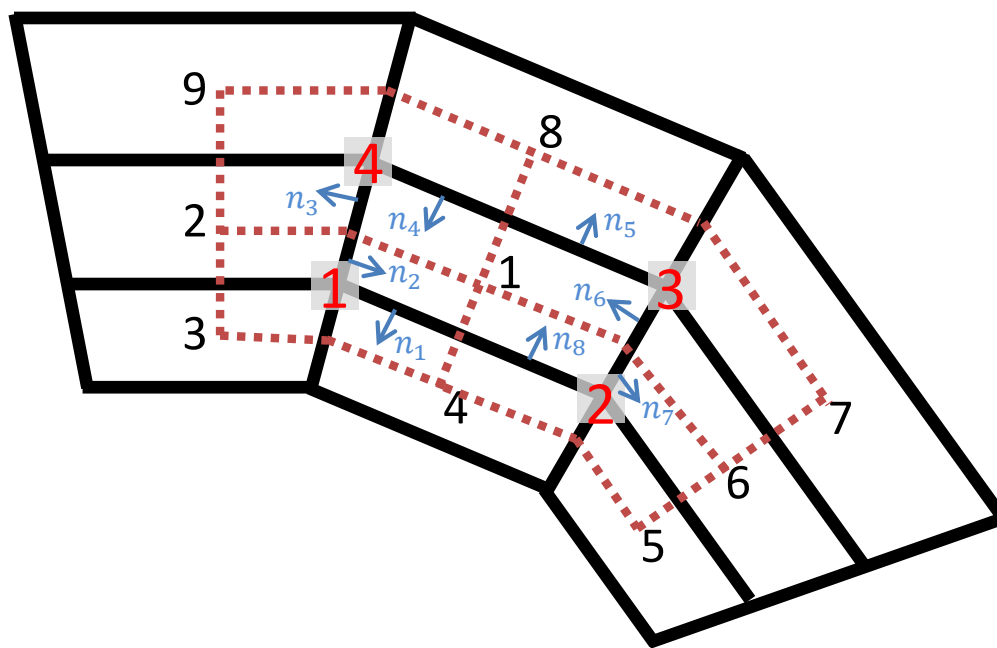


Figure 5.3: Flow directions through 8 sub-interfaces of cell 1 located in the first and the third quadrants.

out of cell 1 through the sub-interfaces depicted by normal vectors n_1 and n_2 . $t_{13}^{(1)}$ and $t_{23}^{(1)}$ are the coefficients of the potential of the cell 3 in interaction region 1. Since in Fig. 5.3, the flux between cells 1 and 2 is into cell 1 and the flux between cells 1 and 4 is out of cell 1, we set the transmissibility coefficient of the potential of cell 3, t_3 , equal to $t_{23}^{(1)} - t_{13}^{(1)}$, which represents the effect of the potential of cell 3 on the flow rate out of cell 1 through sub-interfaces 1 and 2.

The transmissibility coefficients for the cell interfaces are calculated by combining the coefficients obtained from the four interaction regions around the cell as follows:

$$t_1 = -t_{21}^{(1)} + t_{11}^{(1)} - t_{81}^{(2)} + t_{71}^{(2)} + t_{51}^{(3)} - t_{61}^{(3)} - t_{41}^{(4)} + t_{31}^{(4)} \quad (5.10)$$

$$t_2 = -t_{22}^{(1)} + t_{12}^{(1)} - t_{42}^{(4)} + t_{32}^{(4)} \quad (5.11)$$

$$t_3 = -t_{23}^{(1)} + t_{13}^{(1)} \quad (5.12)$$

$$t_4 = -t_{24}^{(1)} + t_{14}^{(1)} - t_{84}^{(2)} + t_{74}^{(2)} \quad (5.13)$$

$$t_5 = -t_{85}^{(2)} + t_{75}^{(2)} \quad (5.14)$$

$$t_6 = -t_{86}^{(2)} + t_{76}^{(2)} + t_{56}^{(3)} - t_{66}^{(3)} \quad (5.15)$$

$$t_7 = +t_{57}^{(3)} - t_{67}^{(3)} \quad (5.16)$$

$$t_8 = +t_{58}^{(3)} - t_{68}^{(3)} - t_{48}^{(4)} + t_{38}^{(4)} \quad (5.17)$$

$$t_9 = -t_{49}^{(4)} + t_{39}^{(4)}. \quad (5.18)$$

We add superscript/subscript i as the global index of grid cells shown in Fig. 5.4 to write the general form of the mass conservation equation for grid cell i as follows:

$$\sum_{j=1}^9 t_j^i p_j^i = q_i \text{ for } i = 1, 2, \dots, n, \quad (5.19)$$

where t_j^i denotes the transmissibility of the potential of gridblock j used to approximate the

total flux out of cell i , q_i is the source term of cell i , p_j^i is the potential of the neighboring cell j of the grid cell i and n is the number of trapezoidal cells in a hexadecagonal grid refinement. Here, the left hand side of the equation represents the summation of all the fluxes out of the cell i . We introduce the vector quantities $p = (p_1, p_2, \dots, p_n)^T$ and $q = (q_1, q_2, \dots, q_n)^T$ where p_i is the potential of cell i . Then, Eq. 5.19 can be written in matrix form as $Ap = q$, where A is the $n \times n$ matrix of coefficients.

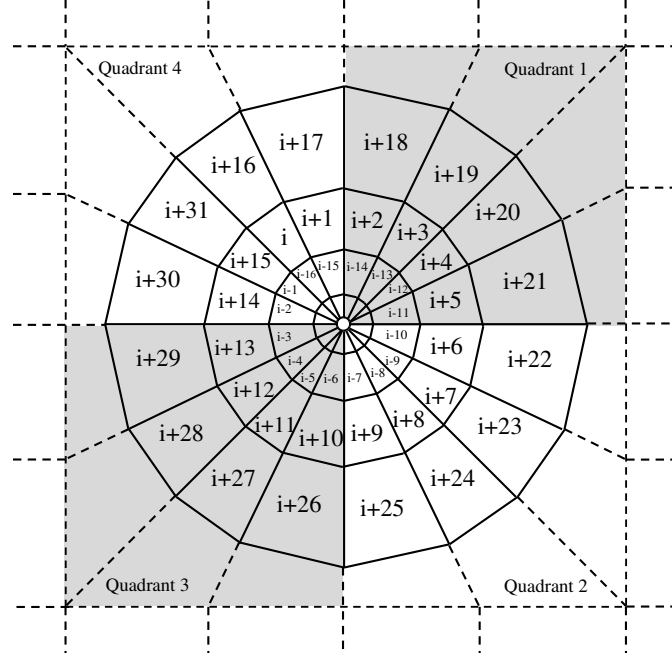


Figure 5.4: A set of irregular hexadecagonal grids for determining transmissibilities for flow into and out of cells $i, i + 1, \dots, i + 15$.

We specify l as the ring number with the first ring around the well as ring $l = 1$. Based on the global ordering of the grid cells shown in Fig. 5.4, the first cell ($i = 16l - 15$) and the last cell ($i = 16l$) in ring l are located in the fourth quadrant and we use the local numbering of grid cells shown in Fig. 5.2b for these cells. Considering the local ordering in Fig. 5.2 and the global ordering of the grid cells shown in Fig. 5.5, the i th row of the matrix A can be written as shown in Table. 5.1. Row i represents the transmissibility coefficients used to compute the total flux out of cell i .

As we defined earlier, t_j^i is the transmissibility of the potential of neighboring cell j used to approximate the total flux out of cell i . In Table 5.1, the column index $i \neq 16l, 16l - 15$

Table 5.1: The nonzero entries of the i th row of the matrix A .

Column index	$i - 31$	$i - 17$	$i - 16$	$i - 15$	$i - 1$	i	$i + 1$	$i + 15$	$i + 16$	$i + 17$	$i + 31$
If $i \neq 16l, 16l - 15$		t_3^i	t_4^i	t_5^i	t_2^i	t_1^i	t_6^i	t_9^i	t_8^i	t_7^i	
If $i = 16l$		t_5^i	t_4^i	t_3^i	t_6^i	t_1^i	t_2^i	t_7^i	t_8^i	t_9^i	
If $i = 16l - 15$	t_3^i	t_5^i	t_4^i	t_2^i	t_6^i	t_1^i	t_9^i	t_7^i	t_8^i	t_9^i	t_7^i

has two rows. The first row represents the transmissibility coefficients of a cell in the first and the third quadrants and the second row represents the transmissibility coefficients of a cell in the second and the fourth quadrants. Cell i in Fig. 5.5a can be located in any quadrant. Note that the elements in the first and the second rows of the column index $i \neq 16l, 16l - 15$ are obtained respectively, by comparing the global numbering in Fig. 5.5a with the local numberings shown in Fig. 5.2a and Fig. 5.2b. The elements in the column index $i = 16l$ are obtained by comparing the global numbering in Fig. 5.5b with the local numbering shown in Fig. 5.2b and the elements in the column index $i = 16l - 15$ are obtained by comparing Fig. 5.5c with Fig. 5.2b.

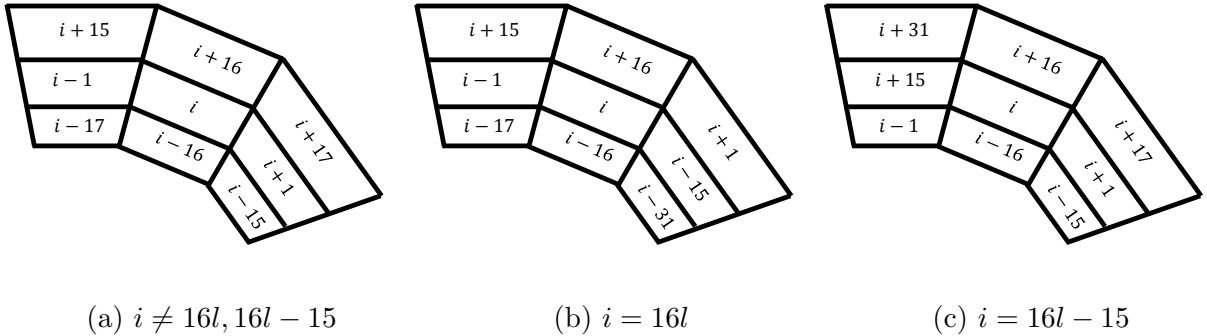


Figure 5.5: Global numbering of a gridblock and its 8 neighboring cells for three different locations in the ring.

To derive conditions that ensure A , with the nonzero entries shown in Table 5.1, is monotone, we apply the following theorem given by J.M. Nordbotten et al. [31]:

Theorem 1. Assume the real $n \times n$ matrix A has a splitting $A = B - C$, such that $B^{-1} \geq 0$, CB^{-1} is irreducible, $CB^{-1} \geq 0$ and for at least one j , $\sum_i a_{ij} \geq 0$. Then the matrix A is monotone, i.e., A^{-1} exists and $A^{-1} \geq 0$.

J.M. Nordbotten et al. [31] showed that the sum of the j th column of the matrix A (from $Ap = q$) is zero. Here j can be the index of any inner grid cell, i.e. a cell that does not share any interface with the reservoir boundary. To prove this, let p be a vector such that the j th component is equal to 1 and all other components are equal to zero (here, each component of the vector p represents the potential at the center of a grid cell). This means, all cells except the inner cell j have zero potential (this includes all boundary cells). Then we solve $Ap = q$ for q which yields

$$q_i = a_{ij}. \quad (5.20)$$

Since j is the index of an inner grid cell, the potential of the boundary cells are zero and because we use the zero Dirichlet boundary conditions, the potential on the boundary is also zero. Thus, there is no flow across the boundary. Since, in the monotonicity analysis, the flow is assumed to be incompressible, thus the sum of the source terms is zero. Therefore,

$$\sum_i a_{ij} = \sum_i q_i = 0, \quad (5.21)$$

so the last monotonicity condition of Theorem 1 is satisfied.

We specify matrix B as the tridiagonal part of the matrix A . Referring back to the structure of the matrix A given in Table 5.1, the i th row of B can be written as shown in Table 5.2. The following result is from G. D. Poole[37].

Table 5.2: The nonzero entries of the i th row of the matrix B .

Column index	$i - 1$	i	$i + 1$
If $i \neq 16l, 16l - 15$	t_2^i	t_1^i	t_6^i
	t_6^i	t_1^i	t_2^i
If $i = 16l$	t_6^i	t_1^i	t_9^i
If $i = 16l - 15$	t_5^i	t_1^i	t_2^i

Definition 3. The square matrix $A = (a_{ij})$ is called an M-matrix if $a_{ij} \leq 0$ whenever $i \neq j$, $a_{ii} > 0$ for each i and any one of the following conditions:

- (a) $A = \alpha I - B$ for some nonnegative matrix B and some $\alpha > \rho$, where ρ is the spectral radius of B .

- (b) The real part of each eigenvalue of A is positive.
- (c) All principal minors of A are positive.
- (d) A^{-1} exists and $A^{-1} \geq 0$.
- (e) There exists a vector $x > 0$ such that $Ax > 0$.

Thus if we can show that a given matrix A satisfies $a_{ij} \leq 0$ whenever $i \neq j$, $a_{ii} > 0$ for each i and condition (e) of Definition 3, then A is an M-matrix and thus, A must also satisfy condition (d), i.e., A^{-1} exists and $A^{-1} \geq 0$ (A is monotone). If we let x be the m -dimensional column vector with all entries equal to unity, then $Ax = y$ where $y_i = \sum_{j=1}^m a_{ij}$ for $i = 1, 2, \dots, m$. Hence, $Ax > 0$ if and only if

$$\sum_{j=1}^m a_{ij} > 0 \text{ for } i = 1, 2, \dots, m. \quad (5.22)$$

If Eq. 5.22 holds, then it follows from Definition 3 that A is an M-matrix if $a_{ij} \leq 0$ whenever $i \neq j$, $a_{ii} > 0$ for each i .

Considering the preceding discussion of Poole's result and referring back to the components of the matrix B shown in Table 5.2, it follows that the conditions given in Table 5.3 are sufficient to guarantee that B is an M-matrix, so that, $B^{-1} \geq 0$ are

Table 5.3: Sufficient conditions for $B^{-1} \geq 0$.

If $i \neq 16l, 16l - 15$	If $i = 16l$	If $i = 16l - 15$
$t_6^i + t_1^i + t_2^i > 0$	$t_9^i + t_1^i + t_6^i > 0$	$t_2^i + t_1^i + t_5^i > 0$
$t_1^i > 0$	$t_1^i > 0$	$t_1^i > 0$
$t_6^i \leq 0$	$t_9^i \leq 0$	$t_2^i \leq 0$
$t_2^i \leq 0$	$t_6^i \leq 0$	$t_5^i \leq 0$

Note that even though the column index $i \neq 16l, 16l - 15$ in Table 5.2 has two rows, there is only one set of conditions in Table 5.3 for both rows.

As the objective is to apply Theorem 1 to show that A is monotone, the matrix C is defined as $C = B - A$. Based on the structure of matrices A and B in Tables 5.1 and 5.2, the i th row of C is given by

Table 5.4: The nonzero entries of the i th row of the matrix C .

Column index	$i - 31$	$i - 17$	$i - 16$	$i - 15$	$i + 15$	$i + 16$	$i + 17$	$i + 31$
If $i \neq 16l, 16l - 15$		$-t_3^i$	$-t_4^i$	$-t_5^i$	$-t_9^i$	$-t_8^i$	$-t_7^i$	
		$-t_5^i$	$-t_4^i$	$-t_3^i$	$-t_7^i$	$-t_8^i$	$-t_9^i$	
If $i = 16l$	$-t_3^i$	$-t_5^i$	$-t_4^i$	$-t_2^i$	$-t_7^i$	$-t_8^i$		
If $i = 16l - 15$			$-t_4^i$	$-t_3^i$	$-t_6^i$	$-t_8^i$	$-t_9^i$	$-t_7^i$

We shall now establish conditions that are sufficient to ensure that $CB^{-1} \geq 0$. In this part, we only consider the first row of column index $i \neq 16l, 16l - 15$ and at the end, to consider the second row, we can simply interchange the subscripts 3 with 5 and 7 with 9 for grid cells located in the second and the fourth quadrants (cells with local numbering shown in Fig. 5.2b). We define the matrix $D = [d_{ij}]$ as the inverse of the matrix B . Then each entry in the i th row and j th column of $E = CB^{-1} = CD$ is given below.

If $i \neq 16l, 16l - 15$:

$$e_{ij} = -t_3^i d_{i-17,j} - t_4^i d_{i-16,j} - t_5^i d_{i-15,j} - t_9^i d_{i+15,j} - t_8^i d_{i+16,j} - t_7^i d_{i+17,j}, \quad (5.23)$$

If $i = 16l$:

$$e_{ij} = -t_3^i d_{i-31,j} - t_5^i d_{i-17,j} - t_4^i d_{i-16,j} - t_2^i d_{i-15,j} - t_7^i d_{i+15,j} - t_8^i d_{i+16,j}, \quad (5.24)$$

If $i = 16l - 15$:

$$e_{ij} = -t_4^i d_{i-16,j} - t_3^i d_{i-15,j} - t_6^i d_{i+15,j} - t_8^i d_{i+16,j} - t_9^i d_{i+17,j} - t_7^i d_{i+31,j}. \quad (5.25)$$

We assume that the conditions of Table 5.3 hold, so $B^{-1} \geq 0$ and hence $d_{ij} \geq 0$. Then the following conditions are sufficient to ensure $e_{ij} \geq 0$ and therefore, $CB^{-1} \geq 0$.

$$t_k^i \leq 0 \text{ for } \begin{cases} k=3,4,5,7,8,9 & \text{if } i \neq 16l, 16l - 15; \\ k=3,4,5,2,8,7 & \text{if } i = 16l; \\ k=6,4,3,7,8,9 & \text{if } i = 16l - 15. \end{cases} \quad (5.26)$$

J.M. Nordbotten et al. [31] used the equation $BD = I$ to obtain less restrictive conditions on the transmissibility coefficients and next, we consider this approach for the problem of interest here. If $i \neq 16l, 16l - 15$, $BD = I$ implies

$$t_2^i d_{i-1,j} + t_1^i d_{i,j} + t_6^i d_{i+1,j} = \delta_{i,j}, \text{ for all } j. \quad (5.27)$$

Rearranging Eq. 5.27 gives,

$$d_{i,j} = \frac{\delta_{i,j}}{t_1^i} - \frac{t_2^i}{t_1^i} d_{i-1,j} - \frac{t_6^i}{t_1^i} d_{i+1,j}, \text{ for all } i \neq 16l, 16l - 15. \quad (5.28)$$

Similarly, for $i = 16l$,

$$d_{i,j} = \frac{\delta_{i,j}}{t_1^i} - \frac{t_6^i}{t_1^i} d_{i-1,j} - \frac{t_9^i}{t_1^i} d_{i+1,j}, \text{ for all } j, \quad (5.29)$$

and for $i = 16l - 15$,

$$d_{i,j} = \frac{\delta_{i,j}}{t_1^i} - \frac{t_5^i}{t_1^i} d_{i-1,j} - \frac{t_2^i}{t_1^i} d_{i+1,j}, \text{ for all } j. \quad (5.30)$$

Next, we write Eqs. 5.28, 5.29 and 5.30 for $d_{i-16,j}$ and $d_{i+16,j}$, and substitute the results into Eqs. 5.23, 5.24 and 5.25 to obtain the following results.

if $i \neq 16l, 16l - 15$:

$$\begin{aligned} e_{ij} = & -t_4^i \frac{\delta_{i-16,j}}{t_1^{i-16}} + \left(t_4^i \frac{t_2^{i-16}}{t_1^{i-16}} - t_3^i \right) d_{i-17,j} + \left(t_4^i \frac{t_6^{i-16}}{t_1^{i-16}} - t_5^i \right) d_{i-15,j} \\ & -t_8^i \frac{\delta_{i+16,j}}{t_1^{i+16}} + \left(t_8^i \frac{t_2^{i+16}}{t_1^{i+16}} - t_9^i \right) d_{i+15,j} + \left(t_8^i \frac{t_6^{i+16}}{t_1^{i+16}} - t_7^i \right) d_{i+17,j} \geq 0; \end{aligned} \quad (5.31)$$

if $i = 16l$:

$$\begin{aligned} e_{ij} = & -t_4^i \frac{\delta_{i-16,j}}{t_1^{i-16}} + \left(t_4^i \frac{t_6^{i-16}}{t_1^{i-16}} \right) d_{i-17,j} + \left(t_4^i \frac{t_9^{i-16}}{t_1^{i-16}} - t_3^i \right) d_{i-15,j} \\ & -t_8^i \frac{\delta_{i+16,j}}{t_1^{i+16}} + \left(t_8^i \frac{t_6^{i+16}}{t_1^{i+16}} - t_6^i \right) d_{i+15,j} + \left(t_8^i \frac{t_9^{i+16}}{t_1^{i+16}} - t_9^i \right) d_{i+17,j} - t_7^i d_{i+31,j} \geq 0; \end{aligned} \quad (5.32)$$

and if $i = 16l - 15$:

$$\begin{aligned}
e_{ij} = & -t_3^i d_{i-31,j} - t_4^i \frac{\delta_{i-16,j}}{t_1^{i-16}} + \left(t_4^i \frac{t_5^{i-16}}{t_1^{i-16}} - t_5^i \right) d_{i-17,j} + \left(t_4^i \frac{t_2^{i-16}}{t_1^{i-16}} - t_2^i \right) d_{i-15,j} \\
& - t_8^i \frac{\delta_{i+16,j}}{t_1^{i+16}} + \left(t_8^i \frac{t_5^{i+16}}{t_1^{i+16}} - t_7^i \right) d_{i+15,j} + t_8^i \frac{t_2^{i+16}}{t_1^{i+16}} d_{i+17,j} \geq 0.
\end{aligned} \tag{5.33}$$

The conditions which ensure that each individual term on the right hand side of Eqs. 5.31- 5.33 is non-negative always give less restrictive conditions than Eq. 5.26 and are sufficient to ensure $CB^{-1} \geq 0$. Recalling $B^{-1} = [d_{ij}] \geq 0$, these conditions are given in Table 5.5. As we mentioned earlier, to consider the second row of column index $i \neq$

Table 5.5: Sufficient conditions for $CB^{-1} \geq 0$.

If $i \neq 16l, 16l - 15$	If $i = 16l$	If $i = 16l - 15$
$t_4^i \leq 0$	$t_4^i \leq 0$	$t_4^i \leq 0$
$t_8^i \leq 0$	$t_8^i \leq 0$	$t_8^i \leq 0$
$t_4^i t_2^{i-16} - t_3^i t_1^{i-16} \geq 0$	$t_4^i t_5^{i-16} - t_5^i t_1^{i-16} \geq 0$	$t_6^{i-16} \leq 0$
$t_4^i t_6^{i-16} - t_5^i t_1^{i-16} \geq 0$	$t_4^i t_2^{i-16} - t_2^i t_1^{i-16} \geq 0$	$t_4^i t_9^{i-16} - t_3^i t_1^{i-16} \geq 0$
$t_8^i t_2^{i+16} - t_9^i t_1^{i+16} \geq 0$	$t_8^i t_5^{i+16} - t_7^i t_1^{i+16} \geq 0$	$t_8^i t_6^{i+16} - t_6^i t_1^{i+16} \geq 0$
$t_8^i t_6^{i+16} - t_7^i t_1^{i+16} \geq 0$	$t_9^{i+16} \leq 0$	$t_8^i t_2^{i+16} - t_9^i t_1^{i+16} \geq 0$
	$t_3^i \leq 0$	$t_7^i \leq 0$

$16l, 16l - 15$ in Table 5.4, we interchange the subscripts 3 with 5 and 7 with 9 of the conditions in the first column of Table 5.5. However interchanging these subscripts results in the same set of conditions given in Table 5.5.

If CB^{-1} is a positive matrix, i.e., $e_{ij} > 0$ for all i, j , then it is irreducible. Referring to Eqs. 5.31, 5.32 and 5.33, it follows that $e_{ij} > 0$ for all i, j if the conditions shown in Tables 5.3 and 5.5 are changed to strict inequalities. With this change to strict inequalities in Tables. 5.3 and 5.5, Theorem 1 can be applied to show that A is monotone. Specifically, the criteria in Table 5.6 guarantee that the matrix A is monotone, i.e., A^{-1} exists and $A^{-1} \geq 0$.

Since we did not consider the specific type of MPFA method when deriving the criteria for the monotonicity shown in Table 5.6, these conditions are also valid for other MPFA methods that are defined on the hexadecagonal grid and use a nine-point computational stencil.

Table 5.6: Conditions for $A^{-1} \geq 0$.

If $i \neq 16l, 16l - 15$	If $i = 16l$	If $i = 16l - 15$
$t_6^i + t_1^i + t_2^i > 0$	$t_9^i + t_1^i + t_6^i > 0$	$t_3^i + t_1^i + t_5^i > 0$
$t_1^i > 0$	$t_1^i > 0$	$t_1^i > 0$
$t_6^i < 0$	$t_9^i < 0$	$t_2^i < 0$
$t_2^i < 0$	$t_6^i < 0$	$t_5^i < 0$
$t_4^i < 0$	$t_4^i < 0$	$t_4^i < 0$
$t_8^i < 0$	$t_8^i < 0$	$t_8^i < 0$
$t_4^i t_2^{i-16} - t_3^i t_1^{i-16} > 0$	$t_4^i t_5^{i-16} - t_5^i t_1^{i-16} > 0$	$t_6^{i-16} < 0$
$t_4^i t_6^{i-16} - t_5^i t_1^{i-16} > 0$	$t_4^i t_2^{i-16} - t_2^i t_1^{i-16} > 0$	$t_4^i t_9^{i-16} - t_3^i t_1^{i-16} > 0$
$t_8^i t_2^{i+16} - t_9^i t_1^{i+16} > 0$	$t_8^i t_5^{i+16} - t_7^i t_1^{i+16} > 0$	$t_8^i t_6^{i+16} - t_6^i t_1^{i+16} > 0$
$t_8^i t_6^{i+16} - t_7^i t_1^{i+16} > 0$	$t_9^{i+16} < 0$	$t_8^i t_2^{i+16} - t_9^i t_1^{i+16} > 0$
	$t_3^i < 0$	$t_7^i < 0$

To find useful monotonicity conditions for different MPFA methods, we need to determine which parameters affect the transmissibility coefficients and specific expressions for the transmissibilities. We consider a grid structure where each grid cell is refined into a set of irregular hexadecagons, as this is the grid refinement scheme we advocate for the well testing reservoir simulator, see Fig. 5.4. To keep the size of all refined rectangular neighboring cells equal, we modify the structure of the hexadecagons in such a way that each side of the host cell is divided into four equal parts. Then, the 16 trapezoidal grids between two hexadecagons are not of equal size, as shown in Figs. 5.4 and 3.2. As is typical in such an analysis, we consider the case where the medium is homogeneous but anisotropic.

In this part, we solve the flow equations using the basic MPFA O-method in two dimensions following I. Aavatsmark et al. [2, 5] and the earlier discussion in Section 4.2. To specify an interaction region between each four grid cells with one common point, each cell center is connected to the midpoints of interfaces (I. Aavatsmark et al. [4]). To account for the logarithmic behavior of pressure with distance from the well, when flow is primarily radial in the near wellbore region, the size of the refined grid increases geometrically as we move away from the center of the cell designated as the well location.

Fig. 5.6 shows the interaction region between four grids with grid points P_1 , P_2 , P_3 and P_4 . Here vectors v_l^+ and v_l^- , respectively, are defined as normal to $(P'_l - P_l)$ and $(P'_{m(l)} - P_l)$, chosen so that $\|v_l^+\| = \|P'_l - P_l\|$ and $\|v_l^-\| = \|P'_{m(l)} - P_l\|$. We emphasize that v_l^+ and v_l^- are always outward normal to the part of the grid cell under consideration, n_i

is the outward-pointing unit normal vector to interface i and $m(l)$ is the backward integer function defined as

$$m(i) = \begin{cases} i - 1 & \text{if } i > 1; \\ 4 & \text{if } i = 1. \end{cases} \quad (5.34)$$

Following the earlier discussion in Section 4.2, to compute the transmissibility coefficients, we calculate the following scalar coefficients which are functions of geometry and permeability of the grid,

$$w_{il}^{\pm} = \frac{n_i^T K_l v_l^{\pm} A_i}{2F_l}. \quad (5.35)$$

As throughout, the K_l is the absolute permeability tensor of grid cell l , A_i is the area of interface i and F_l is the area of triangle $P_l P'_l P'_{m(l)}$. For example, the coefficients associated with grid cell 1 and interface 4 in Fig. 5.6 are defined by

$$w_{41}^- = \frac{n_4^T K_1 v_1^- A_4}{2F_1} \quad \text{and} \quad w_{41}^+ = \frac{n_4^T K_1 v_1^+ A_4}{2F_1}, \quad (5.36)$$

where A_4 is the area of the subinterface between grid cells 1 and 4 inside the interaction region. The w_{il}^{\pm} coefficients are used to calculate the transmissibility coefficients in each interaction region. In this part, we assume that $\mathbf{K} = \begin{bmatrix} k_x & 0 \\ 0 & k_y \end{bmatrix}$ is homogeneous anisotropic diagonal permeability tensor in the base Cartesian gridblock containing the well.

If we define the transmissibility matrix as $T = (t_{ij})$ where t_{ij} is the transmissibility coefficient of the potential of the gridblock j associated with interface i , following Section 4.2, the flux and potential continuity conditions at the interfaces of the grid cells in the interaction region yield,

$$T = B(B - D)^{-1}(C - A) + A = D(B - D)^{-1}(C - A) + C, \quad (5.37)$$

where following Eqs. 4.31 – 4.34, matrices A , B , C , and D are expressed in the following way.

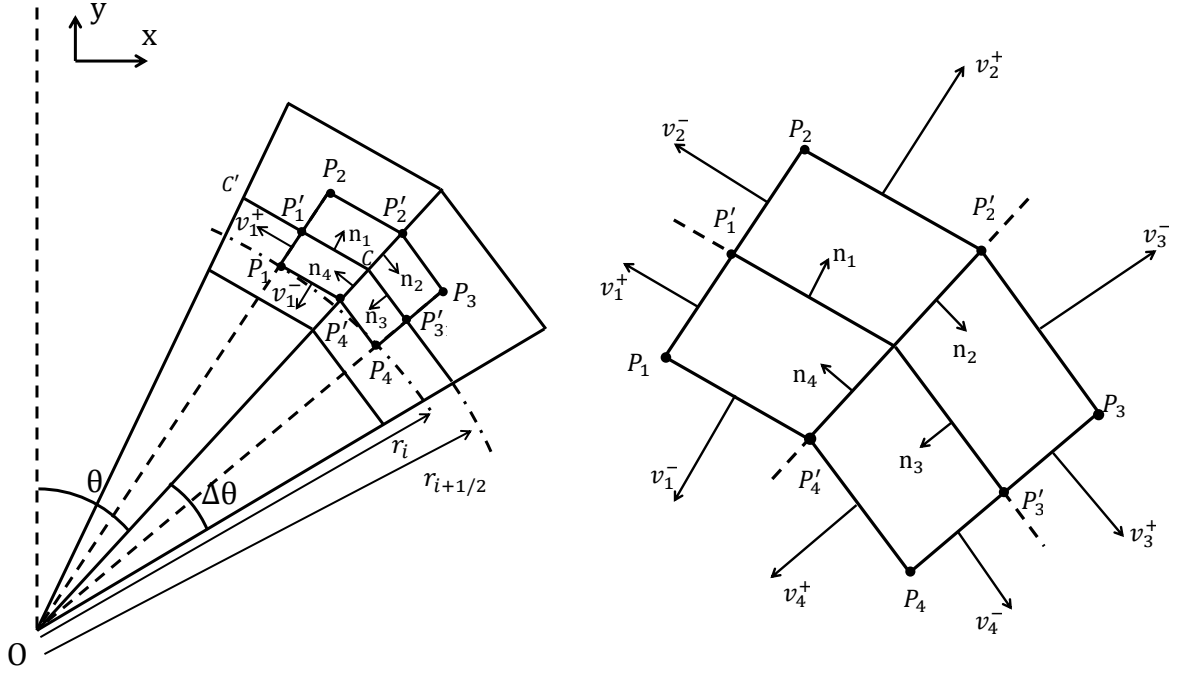


Figure 5.6: Interaction region of four trapezoidal grids.

$$A = \begin{pmatrix} -(w_{11}^+ + w_{11}^-) & 0 & 0 & 0 \\ 0 & -(w_{22}^+ + w_{22}^-) & 0 & 0 \\ 0 & 0 & -(w_{33}^+ + w_{33}^-) & 0 \\ 0 & 0 & 0 & -(w_{44}^+ + w_{44}^-) \end{pmatrix}, \quad (5.38)$$

$$B = \begin{pmatrix} w_{11}^- & 0 & 0 & w_{11}^+ \\ w_{22}^+ & w_{22}^- & 0 & 0 \\ 0 & w_{33}^+ & w_{33}^- & 0 \\ 0 & 0 & w_{44}^+ & w_{44}^- \end{pmatrix}, \quad (5.39)$$

$$C = \begin{pmatrix} 0 & -(w_{12}^+ + w_{12}^-) & 0 & 0 \\ 0 & 0 & -(w_{23}^+ + w_{23}^-) & 0 \\ 0 & 0 & 0 & -(w_{34}^+ + w_{34}^-) \\ -(w_{41}^+ + w_{41}^-) & 0 & 0 & 0 \end{pmatrix} \quad (5.40)$$

and

$$D = \begin{pmatrix} w_{12}^+ & w_{12}^- & 0 & 0 \\ 0 & w_{23}^+ & w_{23}^- & 0 \\ 0 & 0 & w_{34}^+ & w_{34}^- \\ w_{41}^- & 0 & 0 & w_{41}^+ \end{pmatrix}. \quad (5.41)$$

First, we calculate the scalar coefficients, w_{ij}^\pm , for the interaction region centered at $(r_{j+\frac{1}{2}}, \theta)$ where the angle θ is measured counter-clockwise from the positive y-axis, as shown in Fig. 5.6. Here $r_{j+\frac{1}{2}}$ is the radius of the circle that passes through the vertices of i th hexadecagon. Since the reservoir is anisotropic, the transmissibility coefficients are a function of θ .

The unit normal vectors, n_i , are obtained as a function of θ , $\Delta\theta_1$ and $\Delta\theta_2$, shown in Fig. 5.6. Specifically,

$$n_1 = \begin{bmatrix} \sin(\theta - \frac{\Delta\theta_1}{2}) \\ \cos(\theta - \frac{\Delta\theta_1}{2}) \end{bmatrix}, n_2 = \begin{bmatrix} \cos \theta \\ -\sin \theta \end{bmatrix}, n_3 = \begin{bmatrix} -\sin(\theta + \frac{\Delta\theta_2}{2}) \\ -\cos(\theta + \frac{\Delta\theta_2}{2}) \end{bmatrix} \text{ and } n_4 = \begin{bmatrix} -\cos \theta \\ \sin \theta \end{bmatrix}. \quad (5.42)$$

For example, n_1 is a unit normal to line segment $(C' - C)$. Since line segment $(P_2 - O)$ is perpendicular to $(C' - C)$, then n_1 is parallel to $(P_2 - O)$. P'_1 is in the middle of $(C' - C)$, then the angle between the positive y-axis and $(P_2 - O)$ (and hence n_1) is $(\theta - (\frac{\Delta\theta}{2}))$. Using the angle between n_1 and the positive y-axis, and $\|n_1\| = 1$, the x component of unit normal vector n_1 is equal to $\sin(\theta - \frac{\Delta\theta_1}{2})$ and y component of n_1 is equal to $\cos(\theta - \frac{\Delta\theta_1}{2})$.

Here, we specify the magnitudes and the directions of vectors v_i^\pm individually.

$$\frac{v_1^+}{\|v_1^+\|} = \frac{v_2^-}{\|v_2^-\|} = \begin{bmatrix} -\cos(\theta - \frac{\Delta\theta_1}{2}) \\ \sin(\theta - \frac{\Delta\theta_1}{2}) \end{bmatrix}, \frac{v_3^+}{\|v_3^+\|} = \frac{v_4^-}{\|v_4^-\|} = \begin{bmatrix} \cos(\theta + \frac{\Delta\theta_2}{2}) \\ -\sin(\theta + \frac{\Delta\theta_2}{2}) \end{bmatrix}. \quad (5.43)$$

For example, both vectors v_1^+ and v_2^- are perpendicular to $(P_2 - O)$ and hence n_1 . We know that vectors $[a, b]^T$ and $[-b, a]^T$ are perpendicular with the same magnitude. Then, if $(l)_x$

and $(l)_y$ respectively, represent the x and y components of vector l, the x and y components of v_1^+ and v_2^- can be obtained based on n_1 components as follows: $(v_1^+)_y = (v_2^-)_y = (n_1)_x$, and $(v_1^+)_x = (v_2^-)_x = -(n_1)_y$.

A trapezoid has a pair of parallel sides. Then, vectors v_2^+ and v_1^- are both parallel to n_1 , and vectors v_4^+ and v_3^- are parallel to n_3 . Specifically,

$$\frac{v_2^+}{\|v_2^+\|} = -\frac{v_1^-}{\|v_1^-\|} = n_1, \quad \frac{v_4^+}{\|v_4^+\|} = -\frac{v_3^-}{\|v_3^-\|} = n_3. \quad (5.44)$$

The vector magnitudes, $\|v_l^\pm\|$, are a function of $r_{j-\frac{1}{2}}$, α , θ , $\Delta\theta_1$ and $\Delta\theta_2$. Throughout, the geometric ratio is defined as

$$\alpha = \frac{r_{i+\frac{1}{2}}}{r_{i-\frac{1}{2}}}, \quad i = 1, 2, \dots, m, \quad (5.45)$$

where, $r_{1/2} = r_w$ and m is the number of rings. In this part, we compute the magnitudes of v_l^\pm for $l = 1$. The magnitudes of other vectors can be computed in a similar way. Vector v_1^- is defined as normal to $(P'_{m(l)} - P_l)$ with $\|v_1^-\| = \|P'_{m(l)} - P_l\|$. Thus,

$$\|v_1^-\| = \|P'_4 - P_1\|. \quad (5.46)$$

Considering the right-angle triangle $OP_1P'_4$ in Fig. 5.7,

$$\|P'_4 - P_1\| = \|P'_4 - O\| \sin\left(\frac{\Delta\theta_1}{2}\right). \quad (5.47)$$

As we mentioned before, to specify an interaction region between each four grid cells with one common point, each cell center is connected to the midpoints of interfaces. Using this observation and Eq. 5.45, it follows that

$$\|P'_4 - O\| = \frac{r_{i+\frac{1}{2}} + r_{i-\frac{1}{2}}}{2} = \frac{r_{i-\frac{1}{2}}(\alpha + 1)}{2}. \quad (5.48)$$

Using Eqs. 5.47 and 5.48 in Eq. 5.46, it follows that

$$\|v_1^-\| = \|P_4' - P_1\| = r_{i-\frac{1}{2}} \frac{\alpha + 1}{2} \sin\left(\frac{\Delta\theta_1}{2}\right). \quad (5.49)$$

The vector v_1^+ is defined as normal to $(P_1' - P_1)$ with

$$\|v_1^+\| = \|P_1' - P_1\|. \quad (5.50)$$

On the other hand,

$$\|P_1' - P_1\| = \|P_1' - O\| - \|P_1 - O\|. \quad (5.51)$$

Considering the right-angle triangles OP_1P_4' and OP_1C in Fig. 5.7, we have

$$\|P_1' - O\| = r_{i+\frac{1}{2}} \cos\left(\frac{\Delta\theta_1}{2}\right), \quad (5.52)$$

and

$$\|P_1 - O\| = \frac{r_{i+\frac{1}{2}} + r_{i-\frac{1}{2}}}{2} \cos\left(\frac{\Delta\theta_1}{2}\right). \quad (5.53)$$

Therefore, using Eqs. 5.51, 5.52 and 5.53 in Eq. 5.50, the magnitude of v_1^+ is computed as follows:

$$\|v_1^+\| = \|P_1' - P_1\| = r_{i-\frac{1}{2}} \frac{\alpha - 1}{2} \cos\left(\frac{\Delta\theta_1}{2}\right). \quad (5.54)$$

The vector v_2^- is defined as normal to $(P_2 - P_1')$ with

$$\|v_2^-\| = \|P_2 - P_1'\|. \quad (5.55)$$

Similar to Eq. 5.53 and using Eq. 5.45, the magnitude of $(P_2 - O)$ can be computed as follows:

$$\|P_2 - O\| = \frac{r_{i+\frac{3}{2}} + r_{i+\frac{1}{2}}}{2} \cos\left(\frac{\Delta\theta_1}{2}\right) = \alpha \frac{r_{i+\frac{1}{2}} + r_{i-\frac{1}{2}}}{2} \cos\left(\frac{\Delta\theta_1}{2}\right). \quad (5.56)$$

Then, using Eqs. 5.52 and 5.56 in Eq. 5.55, the magnitude of v_2^- is computed as follows:

$$\|v_2^-\| = \|P_2 - P'_1\| = \alpha r_{i-\frac{1}{2}} \frac{\alpha - 1}{2} \cos\left(\frac{\Delta\theta_1}{2}\right). \quad (5.57)$$

Similarly,

$$\|v_1^-\| = \frac{1}{\alpha} \|v_2^+\| = r_{j-\frac{1}{2}} \frac{\alpha + 1}{2} \sin\left(\frac{\Delta\theta_1}{2}\right), \quad (5.58)$$

$$\|v_4^+\| = \frac{1}{\alpha} \|v_3^-\| = r_{j-\frac{1}{2}} \frac{\alpha + 1}{2} \sin\left(\frac{\Delta\theta_2}{2}\right), \quad (5.59)$$

$$\|v_4^-\| = \frac{1}{\alpha} \|v_3^+\| = r_{j-\frac{1}{2}} \frac{\alpha - 1}{2} \cos\left(\frac{\Delta\theta_2}{2}\right). \quad (5.60)$$

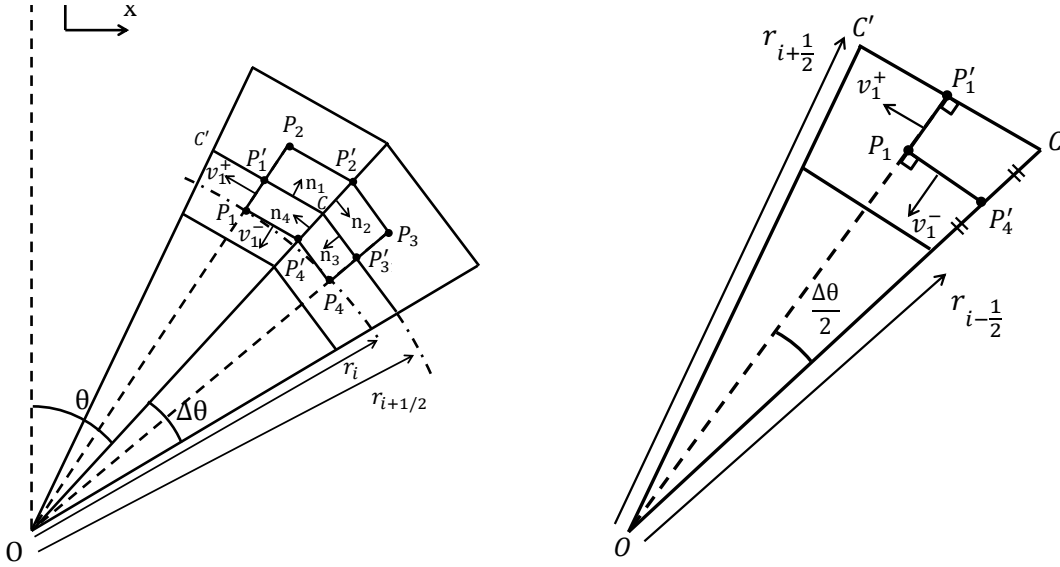


Figure 5.7: Interaction region of four trapezoidal gridblocks.

The area of each interface is a function of $r_{j-\frac{1}{2}}$, α , $\Delta\theta_1$ and $\Delta\theta_2$ but not θ . Specifically,

$$A_1 = \alpha r_{j-\frac{1}{2}} \sin\left(\frac{\Delta\theta_1}{2}\right), \quad A_3 = \alpha r_{j-\frac{1}{2}} \sin\left(\frac{\Delta\theta_2}{2}\right), \quad A_4 = \alpha A_2 = r_{j-\frac{1}{2}} \frac{\alpha - 1}{2}. \quad (5.61)$$

Here $A_1 = \|P'_1 - C\|$ is the area of the sub-interface between cells 1 and 2 shown in Fig. 5.7.

Referring back to Eq. 4.13 in Section 4, the area of the triangle, F_l , with vertices P_l , P'_l and

$P'_m(l)$, is computed as follows:

$$F_l = \frac{1}{2} \|v_l^-\| \|v_l^+\| \sin(\beta), \quad (5.62)$$

where, β is the angle between v_l^- and v_l^+ and is equal to $\pi/2$; see Fig. 5.7. Therefore, F_l is computed using the magnitudes of vectors v_l^- and v_l^+ .

$$F_1 = \frac{\|v_1^-\| \|v_1^+\|}{2} = r_{j-\frac{1}{2}}^2 \left(\frac{\alpha^2 - 1}{16} \right) \sin \Delta\theta_1, \quad (5.63)$$

$$F_2 = \frac{\|v_2^-\| \|v_2^+\|}{2} = \alpha^2 r_{j-\frac{1}{2}}^2 \left(\frac{\alpha^2 - 1}{16} \right) \sin \Delta\theta_1, \quad (5.64)$$

$$F_3 = \frac{\|v_3^-\| \|v_3^+\|}{2} = \alpha^2 r_{j-\frac{1}{2}}^2 \left(\frac{\alpha^2 - 1}{16} \right) \sin \Delta\theta_2. \quad (5.65)$$

$$F_4 \frac{\|v_4^-\| \|v_4^+\|}{2} = r_{j-\frac{1}{2}}^2 \left(\frac{\alpha^2 - 1}{16} \right) \sin \Delta\theta_2. \quad (5.66)$$

Substituting Eqs. 5.42 through 5.64 into Eq. 5.35 yields

$$w_{11}^- = \frac{A_1 \|v_1^-\|}{2F_1} n_1^T K_1 \frac{v_1^-}{\|v_1^-\|} = \frac{\alpha r_{j-\frac{1}{2}} \sin\left(\frac{\Delta\theta_1}{2}\right) \left(r_{j-\frac{1}{2}} \frac{\alpha+1}{2} \sin\left(\frac{\Delta\theta_1}{2}\right) \right)}{r_{j-\frac{1}{2}}^2 \frac{\alpha^2-1}{8} \sin(\Delta\theta_1)} \begin{bmatrix} \sin\left(\theta - \frac{\Delta\theta_1}{2}\right) \\ \cos\left(\theta - \frac{\Delta\theta_1}{2}\right) \end{bmatrix}^T \begin{bmatrix} k_x & 0 \\ 0 & k_y \end{bmatrix} \begin{bmatrix} -\sin\left(\theta - \frac{\Delta\theta_1}{2}\right) \\ -\cos\left(\theta - \frac{\Delta\theta_1}{2}\right) \end{bmatrix}. \quad (5.67)$$

After rearranging Eq. 5.67 and using $\frac{\sin^2(\Delta\theta_1/2)}{\sin \Delta\theta_1} = \frac{\tan(\Delta\theta_1/2)}{2}$,

$$w_{11}^- = -\frac{2\alpha \tan\left(\frac{\Delta\theta_1}{2}\right)}{\alpha - 1} \left(k_x \sin^2\left(\theta - \frac{\Delta\theta_1}{2}\right) + k_y \cos^2\left(\theta - \frac{\Delta\theta_1}{2}\right) \right), \quad (5.68)$$

Similarly,

$$w_{22}^- = \frac{(\alpha - 1)}{\alpha(\alpha + 1) \sin\left(\frac{\Delta\theta_1}{2}\right)} \left(k_y \sin(\theta) \sin\left(\theta - \frac{\Delta\theta_1}{2}\right) - k_x \cos(\theta) \cos\left(\theta - \frac{\Delta\theta_1}{2}\right) \right), \quad (5.69)$$

$$w_{33}^- = -\frac{2 \tan\left(\frac{\Delta\theta_2}{2}\right)}{\alpha - 1} \left(k_x \sin^2\left(\theta + \frac{\Delta\theta_2}{2}\right) + k_y \cos^2\left(\theta + \frac{\Delta\theta_2}{2}\right) \right), \quad (5.70)$$

$$w_{44}^- = -\frac{\alpha(\alpha - 1)}{(\alpha + 1) \sin\left(\frac{\Delta\theta_2}{2}\right)} \left(k_x \cos(\theta) \cos\left(\theta + \frac{\Delta\theta_2}{2}\right) + k_y \sin(\theta) \sin\left(\theta + \frac{\Delta\theta_2}{2}\right) \right), \quad (5.71)$$

$$w_{11}^+ = -\frac{\alpha}{\alpha + 1} (k_x - k_y) \sin(2\theta - \Delta\theta_1), \quad (5.72)$$

$$w_{22}^+ = \frac{1}{\alpha \cos\left(\frac{\Delta\theta_1}{2}\right)} \left(k_x \cos(\theta) \sin\left(\theta - \frac{\Delta\theta_1}{2}\right) - k_y \sin(\theta) \cos\left(\theta - \frac{\Delta\theta_1}{2}\right) \right), \quad (5.73)$$

$$w_{33}^+ = -\frac{1}{\alpha + 1} (k_x - k_y) \sin(2\theta + \Delta\theta_2), \quad (5.74)$$

$$w_{44}^+ = \frac{\alpha}{\cos\left(\frac{\Delta\theta_2}{2}\right)} \left(k_x \cos(\theta) \sin\left(\theta + \frac{\Delta\theta_2}{2}\right) - k_y \sin(\theta) \cos\left(\theta + \frac{\Delta\theta_2}{2}\right) \right), \quad (5.75)$$

$$w_{12}^- = w_{11}^+ / \alpha, \quad (5.76)$$

$$w_{23}^- = \frac{1}{\alpha \cos\left(\frac{\Delta\theta_2}{2}\right)} \left(k_x \cos(\theta) \sin\left(\theta + \frac{\Delta\theta_2}{2}\right) - k_y \sin(\theta) \cos\left(\theta + \frac{\Delta\theta_2}{2}\right) \right), \quad (5.77)$$

$$w_{34}^- = \alpha w_{33}^+, \quad (5.78)$$

$$w_{41}^- = \frac{\alpha}{\cos\left(\frac{\Delta\theta_1}{2}\right)} \left(k_x \cos(\theta) \sin\left(\theta - \frac{\Delta\theta_1}{2}\right) - k_y \sin(\theta) \cos\left(\theta - \frac{\Delta\theta_1}{2}\right) \right), \quad (5.79)$$

$$w_{12}^+ = -w_{11}^- / \alpha, \quad (5.80)$$

$$w_{23}^+ = \frac{(\alpha - 1)}{\alpha(\alpha + 1) \sin\left(\frac{\Delta\theta_2}{2}\right)} \left(k_x \cos(\theta) \cos\left(\theta + \frac{\Delta\theta_2}{2}\right) + k_y \sin(\theta) \sin\left(\theta + \frac{\Delta\theta_2}{2}\right) \right), \quad (5.81)$$

$$w_{34}^+ = -\alpha w_{33}^-, \quad (5.82)$$

$$w_{41}^+ = \frac{(\alpha - 1)\alpha}{(\alpha + 1) \sin\left(\frac{\Delta\theta_1}{2}\right)} \left(k_x \cos(\theta) \cos\left(\theta - \frac{\Delta\theta_1}{2}\right) + k_y \sin(\theta) \sin\left(\theta - \frac{\Delta\theta_1}{2}\right) \right). \quad (5.83)$$

It is important to note that the scalars w_{il}^\pm in Eqs. 5.68 to 5.83 are functions of geometry ($\theta, \Delta\theta_1, \Delta\theta_2$ and α) and permeability (k_x, k_y) of the grid but not a function of $r_{i+\frac{1}{2}}$ or $r_{i-\frac{1}{2}}$ individually. Based on Eqs. 5.68 to 5.83, w_{il}^\pm can be written as $k_y w_{il}'^\pm$, where $w_{il}'^\pm$ is a function of permeability ratio (k_x/k_y) and geometry ($\theta, \Delta\theta_1, \Delta\theta_2$ and α). For example, Eq. 5.79 can

be written as $w_{41}^- = k_y w'_{41}^-$, where

$$w_{41}^- = \frac{\alpha}{\cos\left(\frac{\Delta\theta_1}{2}\right)} \left(\left(\frac{k_x}{k_y}\right) \cos(\theta) \sin\left(\theta - \frac{\Delta\theta_1}{2}\right) - \sin(\theta) \cos\left(\theta - \frac{\Delta\theta_1}{2}\right) \right). \quad (5.84)$$

As shown in Eqs. 5.10 to 5.18, t_j coefficients are calculated by combining the coefficients obtained from the four interaction regions using Eq. 5.37 (Fig. 5.6). From Eqs. 5.37 to 5.41, it is easily seen that t_j^k also can be written as $k_y t_j'^k$ where $t_j'^k$ is a function of permeability ratio and geometry. Since the matrix A is constructed from transmissibility coefficients as shown in Table 5.1, if the matrix A' is defined as $A' = \frac{1}{k_y} A$, then, A' (and as a result A'^{-1}) is only a function of geometry and permeability ratio and not permeability values. Based on the definition of A' , the matrix A is monotone ($A^{-1} \geq 0$) if and only if the matrix A' is monotone ($A'^{-1} \geq 0$). Thus, even though A^{-1} is a function of permeability values, the monotonicity properties of A are only functions of geometry and permeability ratio.

Since the scalars w_{il}^\pm (and hence the transmissibility coefficients) are function of $\alpha = r_{i+\frac{1}{2}}/r_{i-\frac{1}{2}}$ and not functions of $r_{i+\frac{1}{2}}$ or $r_{i-\frac{1}{2}}$ individually, the transmissibilities are repeated after every 16 gridblocks and the nonzero entries of row i of the matrix A are the same as the nonzero entries of row $i + 16$. Because the grid structure is symmetric, we only need to analyze the transmissibility coefficients of the four grid cells in the first quarter of the ring between two hexadecagons. In this case, we consider five interaction regions with $\theta = 0, \pi/8, \pi/4, 3\pi/8, \pi/2$, where θ is measured from the y-axis.

5.2.1 Monotonicity for the O-method

As an example, to investigate the monotonicity regions for the permeability ratio of $k_x/k_y = 2$ and $\Delta x/\Delta y = 1$, we plot in Fig. 5.8, the parameters given in Table 5.6 for $i \neq 16, 16l - 15$ as a function of geometric ratio for hexadecagonal grid cells, calculated as follows:

$$\alpha = l_{i+\frac{1}{2}}/l_{i-\frac{1}{2}}, \quad (5.85)$$

where $l_{i+\frac{1}{2}}$ is the length of the x -axis of the ellipse (or the circle in this case where $\Delta x = \Delta y$)

in which the hexadecagon is inscribed. The bold black line in each graph represents the boundary of the condition for the specific parameter shown in the same graph. To determine the range of α we expect to use in practice, we use Eq. 3.5 which is represented as follows:

$$\alpha = \left(\frac{2\Delta x}{\sqrt{\pi}l_w} \right)^{\frac{1}{N_r+1}}, \quad (5.86)$$

to calculate the minimum and the maximum values of α for a case with $\Delta x = \Delta y$ between 50 and 500 ft and the number of rings between 8 and 25, and l_w between 0.5 and 1.5 ft. A case with $\Delta x = 50$, $l_w = 1.5$ and $N_r = 25$ has the minimum value of α which is equal 1.15 and a case with $\Delta x = 500$, $l_w = 0.5$ and $N_r = 8$ has the maximum value of α which is equal 2.15. Therefore, we only consider the monotonicity criteria for values of the geometric ratio between 1.15 and 2.15.

Based on Fig. 5.8, all inequalities given in Table 5.6 are satisfied for α greater than or equal to 1.1, except the inequality $t_4^i t_6^{i-16} - t_5^i t_1^{i-16} > 0$. The results of the plot in the second row and second column of Fig. 5.8 show that this inequality holds only when $1.23 \leq \alpha \leq 1.88$. To find the range where $A^{-1} \geq 0$ holds, we also have to investigate the conditions for $i = 16l$ and $i = 16l - 15$. For instance, t_5 of cells with index $i = 16l$ has to be negative. However, in the above example, this coefficient is positive in the entire range of α (see Fig. 5.9). Thus, the for the MPFA O-method the monotonicity criteria given in Table 5.6 fails in the entire range of α . This, however does not mean the MPFA scheme constructed will not be monotone as the conditions of Table 5.6 are sufficient conditions for monotonicity, but not necessary to have monotonicity.

5.2.2 Monotonicity for the L-method

Figs. 5.8 and 5.9 pertain only to the specific case where the permeability ratio, k_x/k_y , is equal to 2, although computational results not shown here, indicate that the MPFA O-method does not satisfy all the monotonicity criteria given in Table 5.6 for any permeability ratio. Therefore, we use a different MPFA method to achieve a discrete maximum principle. Since the L-method uses fewer potential points in transmissibility calculations and the

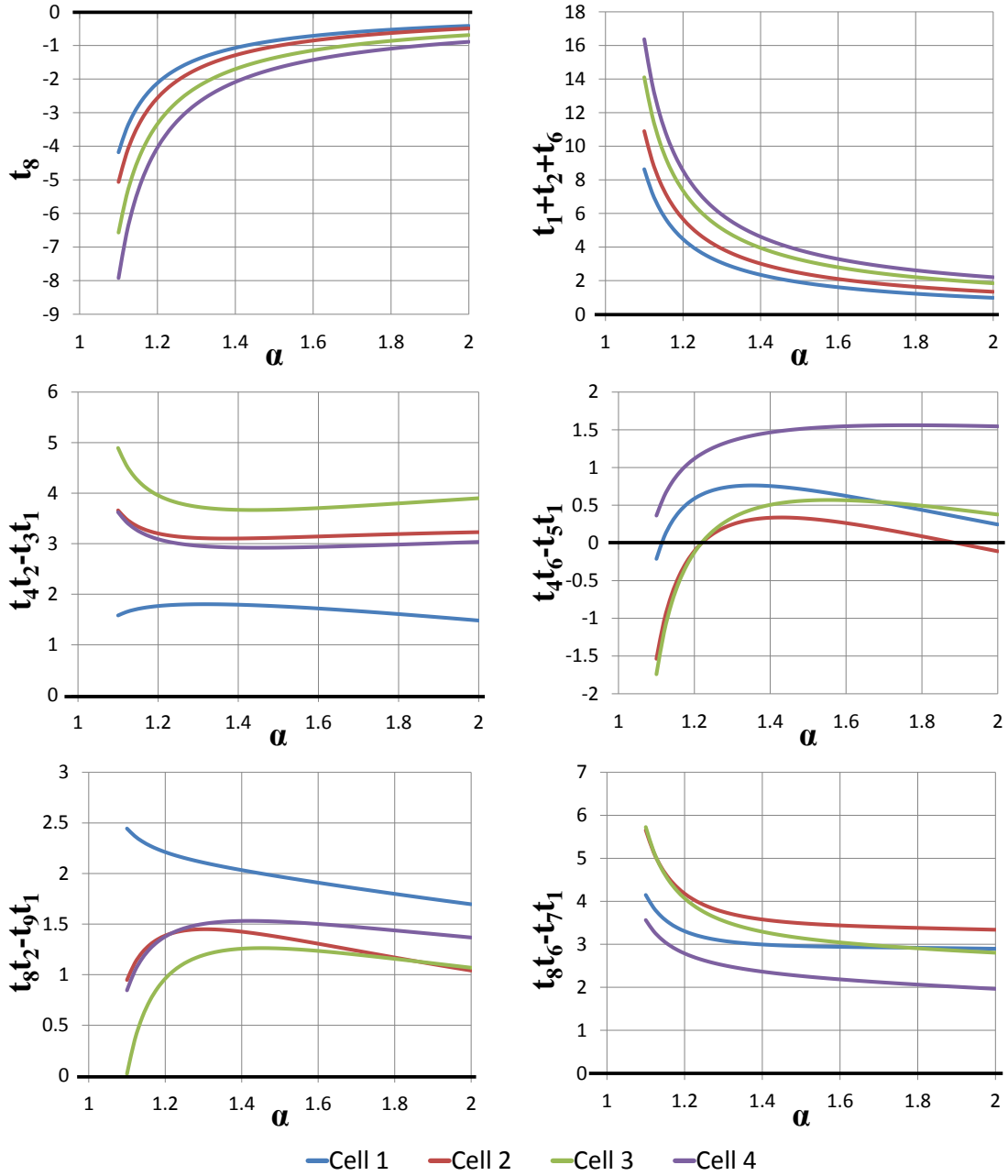


Figure 5.8: The parameters of the monotonicity criteria for $i \neq 16l, 16l - 15$ as a function of geometric ratio, α , with the permeability ratio of $k_x/k_y = 2$ and $\Delta x/\Delta y = 1$, using the O-method.

monotonicity region of the L-method is usually larger than the O-methods, it is expected to yield better results [6]. We use the same conditions listed in Table 5.6 to analyze the monotonicity regions for the grid model presented in this work (Fig. 3.2). Similar to the example for the O-method, we show in Figs. 5.10, 5.11 and 5.12 the criteria given in Table 5.6 as a function of the geometric ratio, α , to investigate the monotonicity regions for

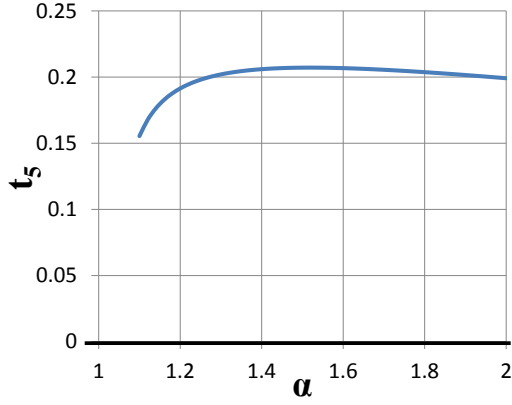


Figure 5.9: The parameter t_5 of criterion $t_5 < 0$ for the last cell in each ring ($i = 16l$) as a function of geometric ratio, α , with $k_x/k_y = 2$ and $\Delta x/\Delta y = 1$, using the O-method.

the permeability ratio of 2. Based on the results of Figs. 5.10, 5.11 and 5.12, all conditions in Table 5.6 hold if $1.2 \leq \alpha \leq 1.8$, whereas the O-method does not satisfy all monotonicity conditions of Table 5.6 for any reasonable α , see Fig. 5.9.

Fig. 5.13 shows the monotonicity regions that we calculated for a set of irregular hexadecagonal grids with a homogeneous medium using the L-method as functions of α and k_x/k_y . Throughout, the aspect ratio is defined as the ratio of the dimensions of the Cartesian cell, i.e. the aspect ratio denoted by AR as $AR = \Delta x/\Delta y$ and the geometric ratio is defined by Eq. 5.85. To create the monotonicity regions in Fig. 5.13, we calculate the transmissibility coefficients based on Eqs. 5.68 to 5.83, Eqs. 5.37 to 5.41 and Eqs. 5.10 to 5.18 for each α , k_x/k_y and $\Delta x/\Delta y$ and then we determine whether the conditions in Table 5.6 are satisfied.

As shown in Fig. 5.13a, for an aspect ratio of 1, the L-method is monotone in the entire range of α for an isotropic permeability field. However, increasing the permeability ratio decreases the monotonicity regions significantly and in a medium with a permeability ratio higher than 4, the method fails to satisfy the criteria of Table 5.6, so we cannot guarantee that it is monotone. However, as shown next, the monotonicity region can be increased by choosing the size of the gridblock containing the well so that

$$\frac{\Delta x}{\Delta y} = \sqrt{\frac{k_x}{k_y}}, \quad (5.87)$$

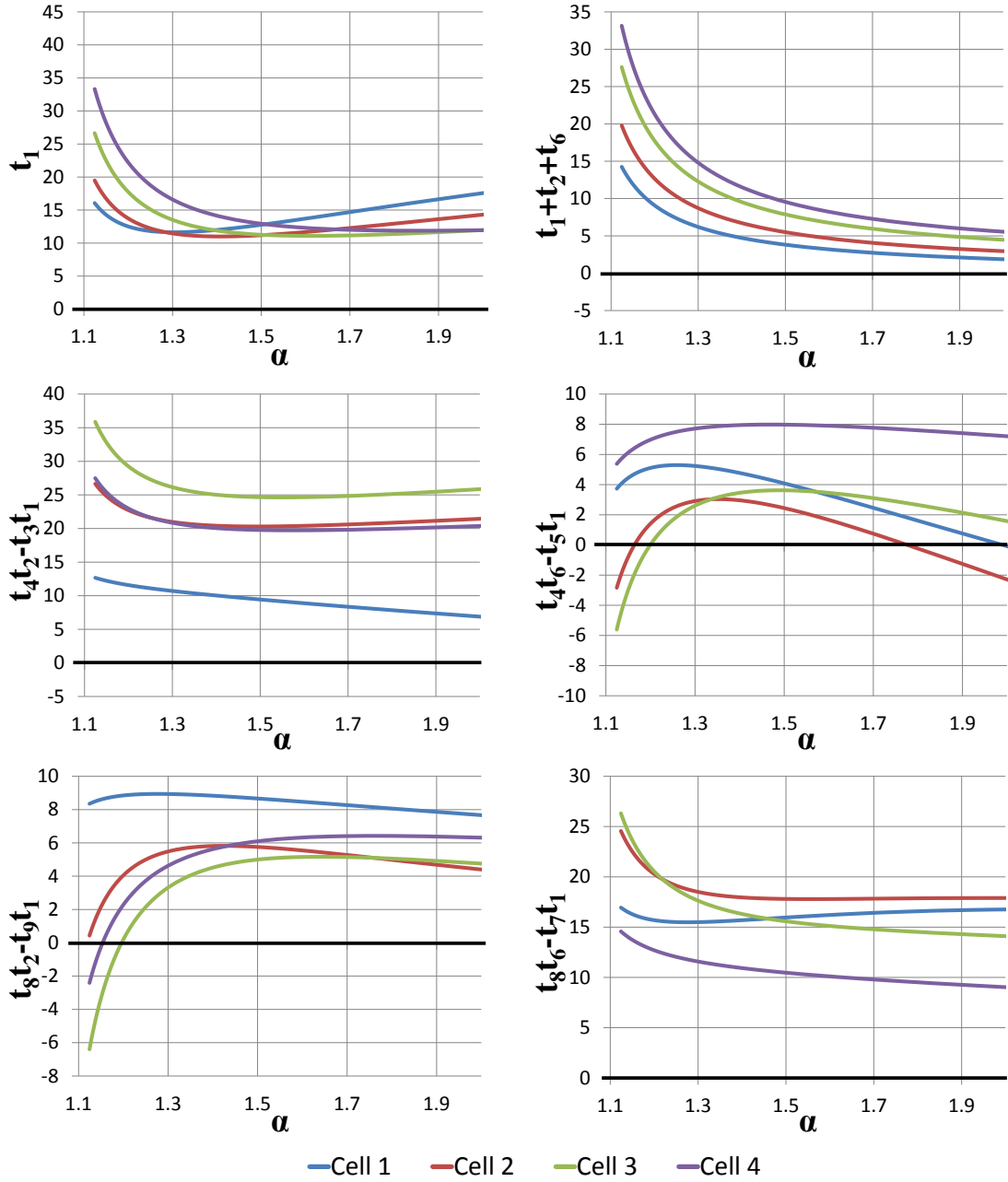


Figure 5.10: The parameters of the monotonicity criteria for $i \neq 16l, 16l - 15$ as a function of geometric ratio, α with the permeability ratio of 2 and $\Delta x/\Delta y = 1$, using the L-method.

or equivalently,

$$R \equiv \frac{\Delta x}{\Delta y} \sqrt{\frac{k_y}{k_x}} = 1. \quad (5.88)$$

The results of Figs. 5.13b, 5.13c and 5.13d consider grids with different aspect ratios, in order to show the effects of adjusting the structure of hexadecagons based on the near-well

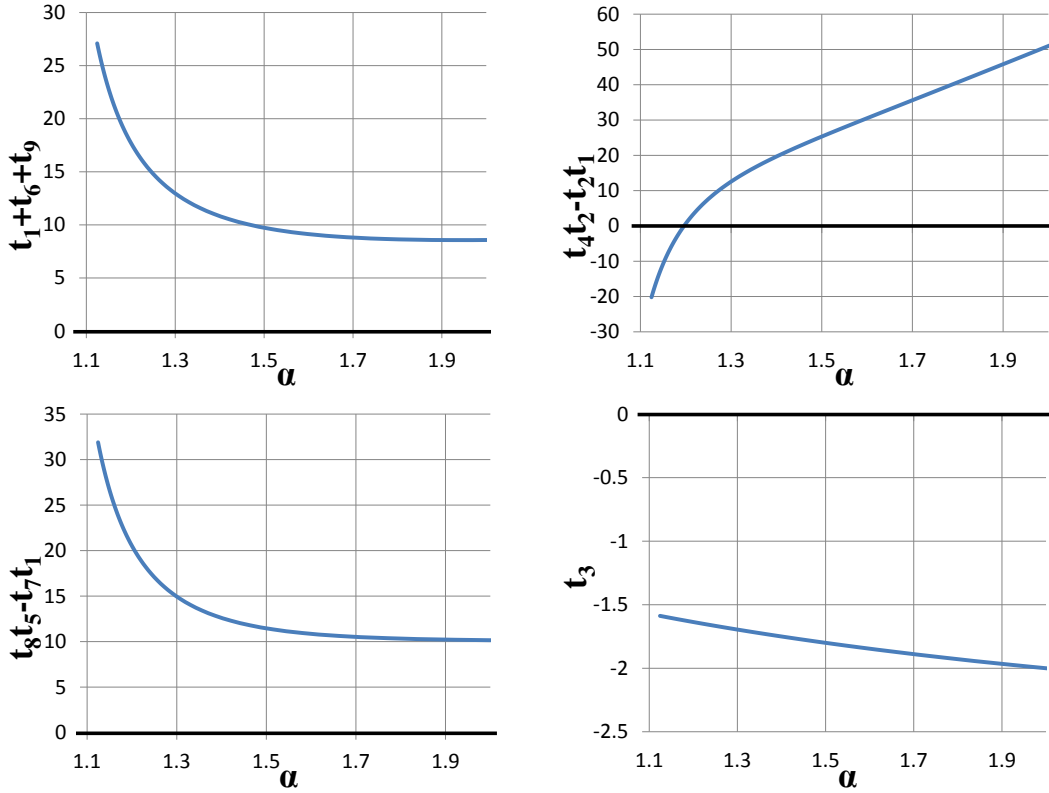


Figure 5.11: The parameters of the monotonicity criteria for the last cell in each ring ($i = 16l$) as a function of geometric ratio, α with the permeability ratio of 2 and $\Delta x/\Delta y = 1$, using the L-method.

flow geometry. From the results of Fig. 5.13 and other similar computations, the L-method for an anisotropic medium has the largest monotonicity range when the aspect ratio is equal to the square root of permeability ratio, i.e. Eq. 5.88 holds. Interestingly, Figs. 5.13a to 5.13d indicate that for any aspect ratio, the geometric ratio of 1.4 is always monotone for the largest range of the permeability ratio, but we have no theoretical explanation of this result.

5.3 Effect of Skin Zone on Monotonicity Regions for the L-method

One of the advantages of a grid refinement around the well is that the skin zone can be modeled adequately based on the permeabilities in the skin zone, and the external radius of the skin zone, r_s . Fig. 5.14 shows a hexadecagonal grid refinement around the well where the two rings closest to the well represent the skin zone (shown in grey). As we mentioned earlier, the coefficients calculated from an interaction region between four cells in a case with a homogeneous medium are not a function of $l_{i+\frac{1}{2}}$. However, considering a skin zone around

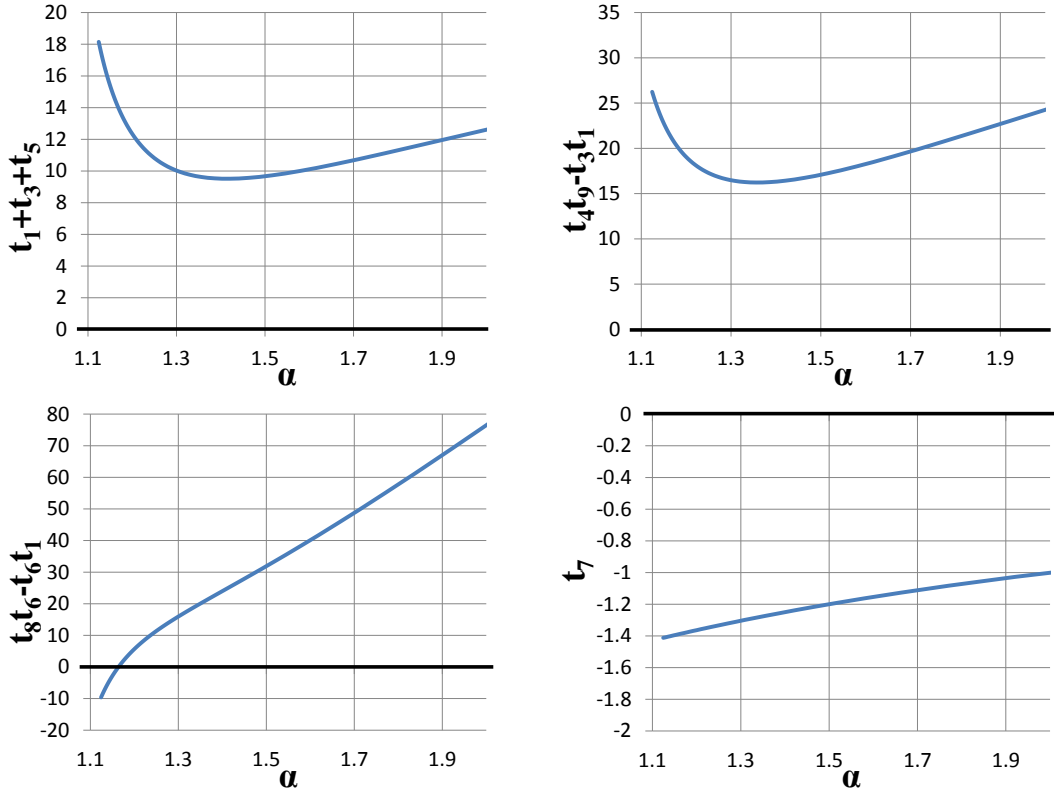


Figure 5.12: The parameters of the monotonicity criteria for the first cell in each ring ($i = 16l - 15$) as a function of geometric ratio, α with the permeability ratio of 2 and $\Delta x/\Delta y = 1$, using the L-method.

the well, the interaction region between four cells where two of them are in the skin zone and the other two are out of the skin zone, creates coefficients which are different from the ones for a homogeneous medium. These coefficients affect the transmissibilities of grid cells in the last ring of the skin zone and the first ring out of the skin zone.

In this study, we assume that the permeability ratio in the skin zone is the same as the one in the unaffected zone, i.e.,

$$\frac{k_{sx}}{k_{sy}} = \frac{k_x}{k_y}. \quad (5.89)$$

We define γ as the ratio of the permeability in the skin zone to the unaffected formation permeability, i.e., $\mathbf{K}_s = \gamma \mathbf{K}$. Since we assumed that the permeability ratio in both regions are equal (Eq. 5.89), then

$$\gamma = \frac{k_{sx}}{k_x} = \frac{k_{sy}}{k_y}. \quad (5.90)$$

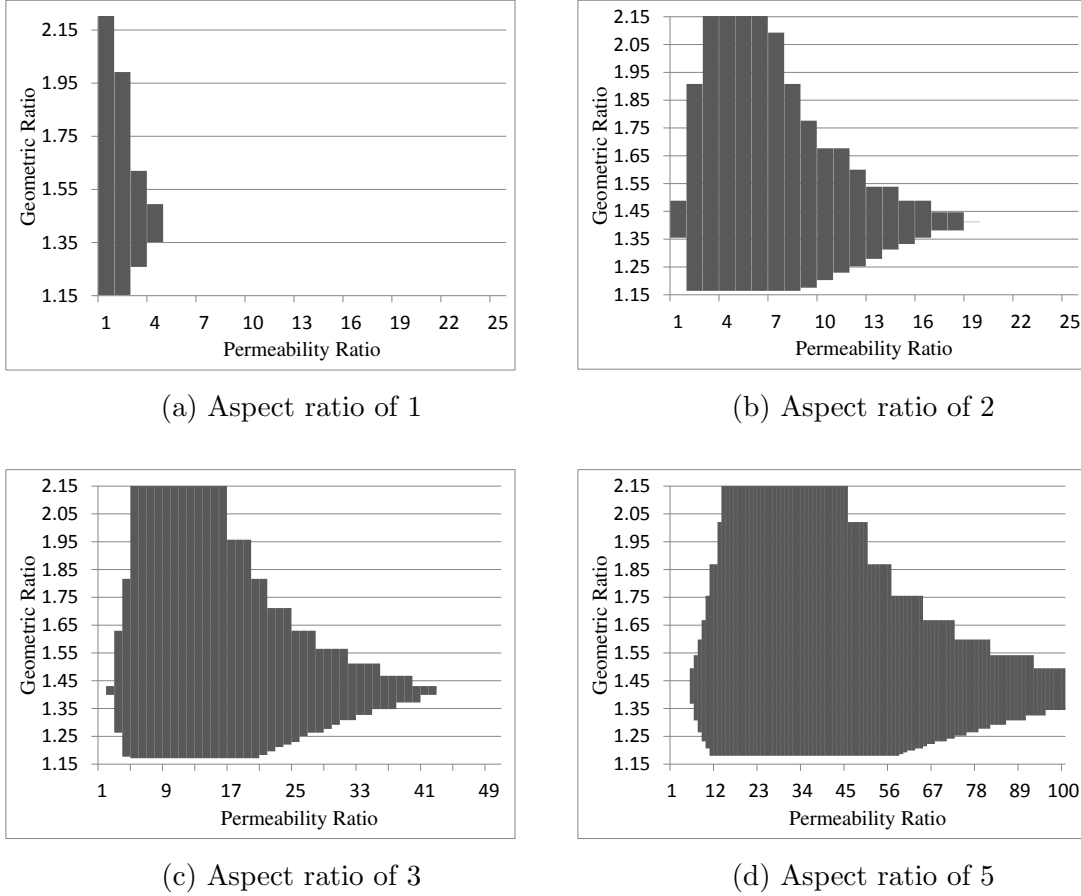


Figure 5.13: Monotonicity regions of hexadecagonal grids using the L-method.

First, we analyze the transmissibility coefficients calculated from an interaction region where all four cells are in the skin zone. In this zone, the permeability values are multiplied by the constant value γ . Based on Eqs. 5.68 to 5.83, the scalars $(w_{il}^{\pm})_s$ can be written as $\gamma(w_{il}^{\pm})_{ns}$. In this part, subscript s refers to values calculated from the permeabilities of the skin zone and subscript ns means that the value is calculated from the unaffected formation permeabilities. Matrices A_s , B_s , C_s and D_s from Eqs. 4.54, 4.55, 4.57 and 4.58 in the skin zone, respectively can be written as γA_{ns} , γB_{ns} , γC_{ns} and γD_{ns} . From Eq. 4.64, the transmissibility coefficient matrix of a cell where all its eight neighbors are in the unaffected zone, $T_{ns} = ((t_{ij})_{ns})$, is as follows:

$$T_{ns} = C_{ns}A_{ns}^{-1}B_{ns} + D_{ns}, \quad (5.91)$$

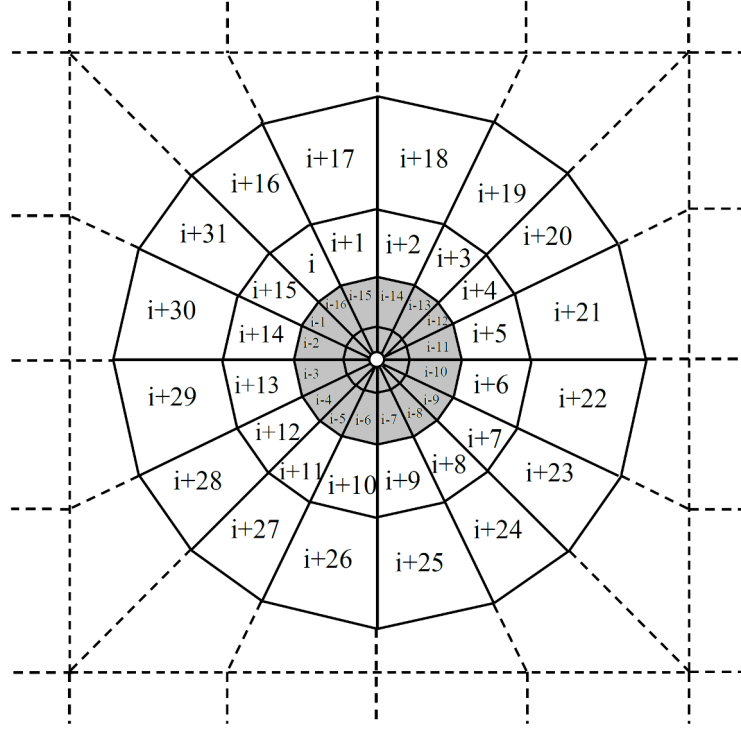


Figure 5.14: A set of irregular hexadecagonal grids with a skin zone shown in grey.

and the transmissibility coefficient matrix of a cell where all its eight neighbors are in the skin zone, $T_n = ((t_{ij})_n)$, is given as follows:

$$T_s = C_s A_s^{-1} B_s + D_s. \quad (5.92)$$

Since, $A_s = \gamma A_{ns}$, $B_s = \gamma B_{ns}$, $C_s = \gamma C_{ns}$ and $D_s = \gamma D_{ns}$ and using Eq. 5.91, Eq. 5.92 can be rearrange as follows:

$$T_s = C_s A_s^{-1} B_s + D_s = (\gamma C_{ns})(\gamma A_{ns})^{-1}(\gamma B_{ns}) + (\gamma D_{ns}) = \gamma(C_{ns} A_{ns}^{-1} B_{ns} + D_{ns}) = \gamma T_{ns}. \quad (5.93)$$

From Eq. 5.93, it is easily seen that $(t_{ij})_s$ also can be written as $\gamma(t_{ij})_{ns}$. Therefore, if the transmissibility coefficients of a cell where all its eight neighbors are in the unaffected zone satisfy the monotonicity conditions listed in Table 5.6, then, the transmissibility coefficients of a cell with the same geometry properties (θ, α) but with all of its neighbors in the skin zone also satisfy the monotonicity conditions.

The major issue is where two cells out of the four cells in the interaction region are in the skin zone and the other two are in the unaffected zone. Transmissibility calculations of the O-method and the L-method show that the permeability values of the skin zone affect all transmissibility coefficients of the interaction region. To analyze the effect of skin on the monotonicity regions for the L-method, we use the coefficients of the interaction regions on the outer boundary of the skin zone and Eqs. 5.10 through 5.18 to compute the transmissibility coefficients of cells in the last ring of the skin zone and the first ring out of the skin zone. For example, in Fig. 5.14, the interaction region between cells $i - 16$, $i - 15$, i and $i + 1$ contains two cells from the skin zone and two cells from the unaffected zone. Then, unlike other interaction regions where all four cells have the same permeability tensor, the permeability tensors of the four cells in this interaction region are different.

Fig. 5.15 shows the monotonicity regions for a set of irregular hexadecagonal grids with a skin zone around the well. In all cases considered $k_{sx} = 0.1k_x$, $k_{sy} = 0.1k_y$ and the four rings closest to the well represent the skin zone. Then, by defining $k_s = \sqrt{k_{sx}k_{sy}}$ and $k = \sqrt{k_xk_y}$, we have

$$\frac{k_s}{k} = \frac{\sqrt{k_{sx}k_{sy}}}{\sqrt{k_xk_y}} = 0.1. \quad (5.94)$$

The monotonicity regions for the case of skin zone with $k/k_s = 10$ are shown in Fig. 5.15. Comparing the results of Fig. 5.15 with those of Fig. 5.13, we see that the presence of a skin decreases the size of the monotonicity region of the L-method. In Fig. 5.13, the geometric ratio of 1.4, for any aspect ratio, is always monotone for the largest range of the permeability ratio. Fig. 5.15 indicates that this “optimal” value of α increases to 1.47 for the skin case. In Fig. 5.15, for a permeability ratio of 1, the monotonicity conditions are not satisfied when the aspect ratio is 2, 3 or 5. However, the conditions are sufficient to guarantee monotonicity but not necessary and our numerical results in the next section show that if a case is out of the monotonicity region but not far from the region, solutions show no non-physical oscillatory behavior, i.e., are monotone.

As shown in Figs. 5.13 and 5.15, for each aspect ratio, we have a different monotonicity

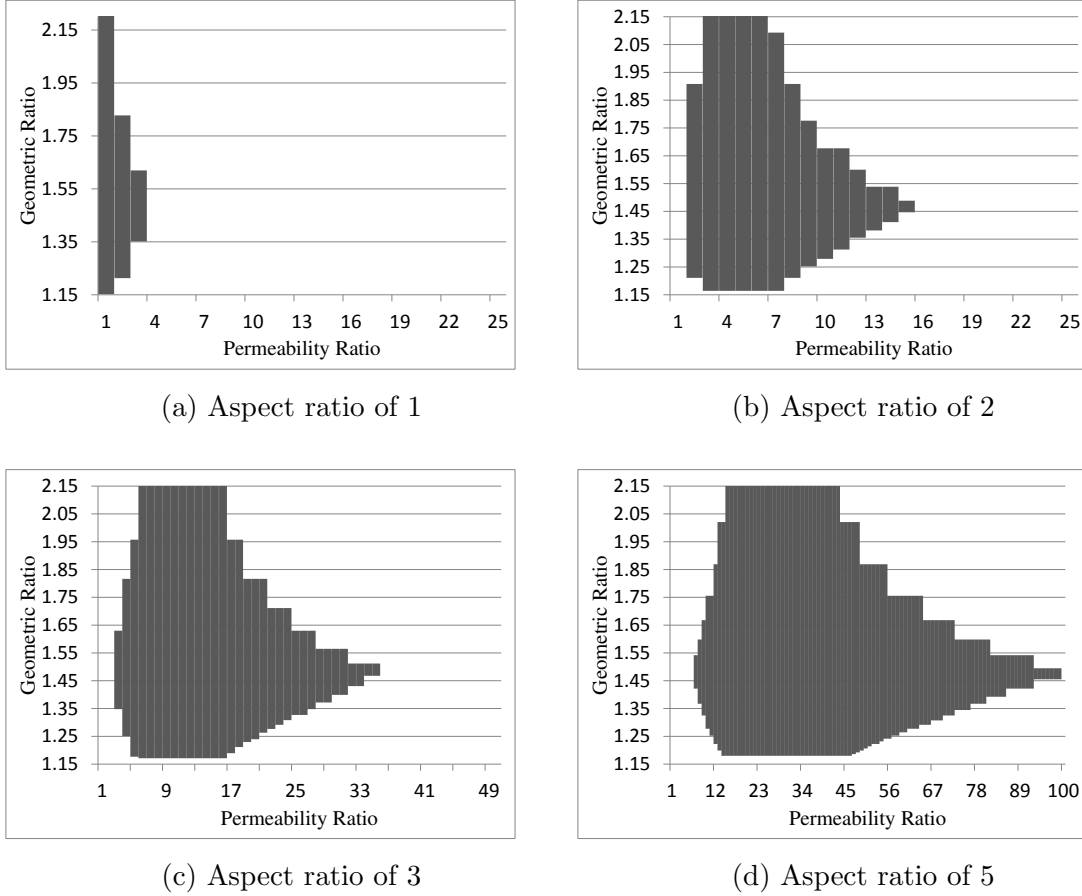
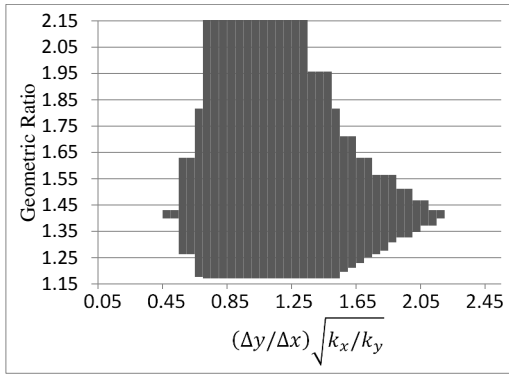


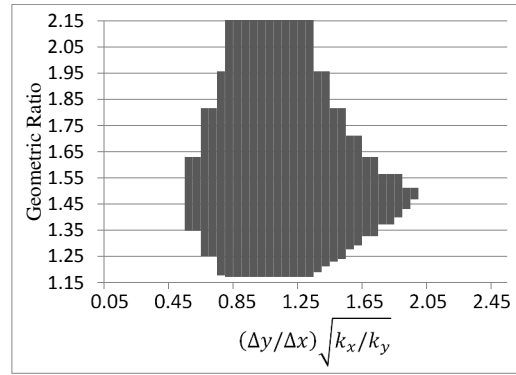
Figure 5.15: Monotonicity regions of hexadecagonal grids with a skin zone using the L-method.

region. Our investigation on these results shows that if we plot the monotonicity region as a function of $(\Delta y/\Delta x) \sqrt{k_x/k_y}$ instead of permeability ratio, the difference between plots is small, i.e., monotonicity regions correlate as a function of α and $(\Delta y/\Delta x) \sqrt{k_x/k_y}$ and one plot can represent the monotonicity region for all aspect ratios. Fig. 5.16a shows the monotonicity regions of hexadecagonal grids without skin using the L-method and Fig. 5.16b shows the monotonicity regions of hexadecagonal grids with the skin zone around the well.

Although the monotonicity results of this and the next section are presented in terms of k_x , k_y , Δx and Δy , i.e., implicitly seen to pertain to a vertical well, it is important to note that they are also applicable to a horizontal well.



(a) No skin



(b) Skin ($k/k_s = 10$)

Figure 5.16: Monotonicity regions of hexadecagonal grids using the L-method.

CHAPTER 6

CONVERGENCE AND NUMERICAL TESTS FOR THE L-METHOD

6.1 Convergence

In this part, we investigate the convergence behavior of the L-method for the polygonal grid refinement system. We consider the effects of the aspect ratio and the skin zone. The case under study is only the polygon part of the grid refinement system and we consider here only the hexadecagonal grid structure, the complete grid system us discussed in Chapeter 7. As shown in Fig. 5.4, the polygon used in the grid refinement system is 16-sided. To increase the number of grid cells, we can only increase the number of rings in the r-direction (N_r). By increasing the number of rings and keeping the number of divisions in the θ -direction (N_θ) constant, the width to height ratio of trapezoidal cells increases. Fig. 5.16 shows that there is an optimum geometric ratio ($\alpha = l_{i+\frac{1}{2}}/l_{i-\frac{1}{2}}$) for a given permeability ratio to have the maximum monotonicity range.

Since we cannot investigate the convergence behavior of the L-method for the grid refinement system where the number of divisions in the θ -direction is constant, we modify the grid refinement system by adjusting N_θ based on N_r , in such a way that the width (average length of the two bases) to height ratio of trapezoidal cells stays constant. Fig. 6.1 shows an isosceles trapezoidal grid cell with the width of w_i and the height of h_i . In the figure, the magnitude of $(C_1 - O)$ and $(C_2 - O)$ are computed as:

$$\|C_1 - O\| = r_{i-\frac{1}{2}} \cos(\theta/2), \quad (6.1)$$

and,

$$\|C_2 - O\| = r_{i+\frac{1}{2}} \cos(\theta/2). \quad (6.2)$$

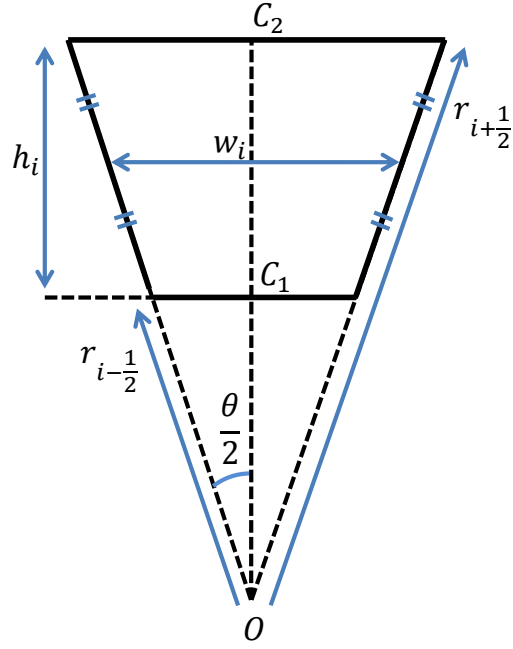


Figure 6.1: An isosceles trapezoidal grid cell

Then, using Eqs. 6.1 and 6.2, the height of the trapezoid can be computed as a function of $r_{i+\frac{1}{2}}$, $r_{i-\frac{1}{2}}$ and θ as follows:

$$h_i = \|C_2 - C_1\| = \left(r_{i+\frac{1}{2}} - r_{i-\frac{1}{2}} \right) \cos(\theta/2) = (\alpha - 1)r_{i-\frac{1}{2}} \cos(\theta/2), \quad (6.3)$$

where $\alpha = r_{i+\frac{1}{2}}/r_{i-\frac{1}{2}}$. The width of the trapezoid, w_i , is defined as the average of the two bases of the trapezoid. Then,

$$w_i = \left(r_{i+\frac{1}{2}} + r_{i-\frac{1}{2}} \right) \sin(\theta/2) = (\alpha + 1)r_{i-\frac{1}{2}} \sin(\theta/2). \quad (6.4)$$

Using Eqs. 6.3 and 6.4, the width to height ratio can be written as follows:

$$\gamma = \frac{w_i}{h_i} = \frac{\alpha + 1}{\alpha - 1} \tan(\theta/2), \quad (6.5)$$

where γ is the width to height ratio of the trapezoid, where we wish to keep constant. By

substituting $\theta = 2\pi/N_\theta$ into Eq. 6.5 and rearranging, we have:

$$N_\theta = \frac{\pi}{\tan^{-1}\left(\gamma\left(1 - \frac{2}{\alpha+1}\right)\right)}. \quad (6.6)$$

where α is computed as follows:

$$\alpha = \left(\frac{l_{max}}{l_w}\right)^{\frac{1}{N_r}}, \quad (6.7)$$

where l_{max} is the length of the ellipse that is used to construct the last polygon, in the x -direction and l_w is the length of the ellipse, used to construct the wellbore polygon, in the x -direction. The wellbore polygon represents the wellbore and has the same area as the wellbore. Since there is no specified value of γ , we use the optimum $\alpha = 1.4$ for the 16-sided polygon to estimate the width to height ratio which gives the highest monotonicity range. As the result, in order to keep the width to height ratio of trapezoidal grid cells approximately constant, for a given number of rings in the r -direction, N_r , the number of divisions in the θ -direction, N_θ , which is calculated using Eq. 6.6, is rounded to the nearest integer, as follows:

$$N_\theta = \left\lceil \frac{\pi}{\tan^{-1}\left(\gamma\left(1 - \frac{2(l_w)^{1/N_r}}{(l_{max})^{1/N_r} + (l_w)^{1/N_r}}\right)\right)} \right\rceil. \quad (6.8)$$

6.1.1 Boundary Conditions Implementation

In this work, we obtain the discrete pressure solutions for cases with polygon grids on homogeneous and heterogenous media. In these cases, equal point sources are located in the grid cells of the first ring and zero Dirichlet boundary conditions are imposed on the boundary of the last polygon. This part presents how we impose Dirichlet boundary conditions.

A simple way to impose Dirichlet boundary conditions is to use an imaginary hexadecagonal ring with $l_{N_r+3/2} = \alpha l_{N_r+1/2}$, where $l_{N_r+1/2}$ is the length of the last hexadecagon in the x -direction and $l_{N_r+3/2}$ is the length of the imaginary hexadecagon in the x -direction. The outer boundary of the ring has the same aspect ratio as the original boundary where we impose the zero pressure. The pressure of each imaginary cell is equal to negative of the

neighboring cell pressure. Fig. 6.2 shows boundary cell i with two neighboring boundary cells $i - 1$ and $i + 1$, three neighboring inner cells $i - j - 1$, $i - j$ and $i - j + 1$ and three imaginary cells $i + j - 1$, $i + j$ and $i + j + 1$. A boundary cell is a cell that shares an edge with the boundary. For the hexadecagonal grid system, j is equal 16. However, the cases we

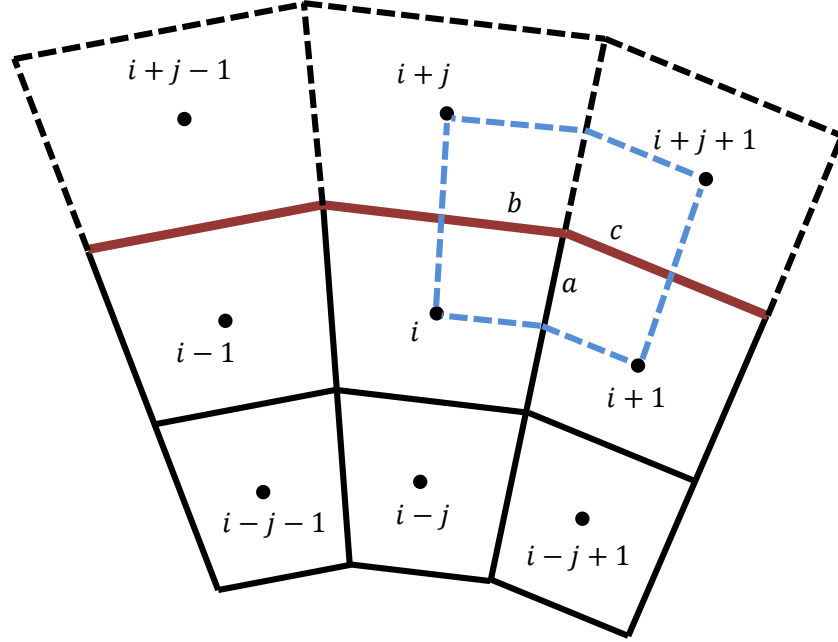


Figure 6.2: A boundary cell with 8 neighboring cells including 3 imaginary cells.

use to analyze the convergence behavior, j is not necessarily equal to 16. The red segments in Fig. 6.2 show the boundary that we wish to impose the zero pressure. For example, we use the interaction region shown in blue in Fig. 6.2 and an MPFA method to compute the transmissibility coefficients for flux between cells i and $i + 1$ through the sub-interface “a” and the flux out of the boundary (in red) from cells i and $i + 1$ through sub-interfaces “b” and “c” The flowrate between cells i and $i + 1$ is written as follows

$$q_{i,i+1} = t_i p_i + t_{i+1} p_{i+1} + t_{i-j} p_{i-j} + t_{i-j+1} p_{i-j+1} + t_{i+j} p_{i+j} + t_{i+j+1} p_{i+j+1}, \quad (6.9)$$

where p_l represents the pressure of cell l and t_l is the transmissibility coefficient of cell l for

flowrate calculation between cells i and $i + 1$. Note that $q_{i,i+1}$ is the flow rate through the interface between cells i and $i + 1$ and not the sub-interface in the interaction region. As we mentioned before, the pressure of each imaginary cell is equal to negative of the neighboring cell pressure, i.e., $p_{i+j} = -p_i$ and $p_{i+j+1} = -p_{i+1}$. Then Eq. 6.11 can be written as follows:

$$q_{i,i+1} = (t_i - t_{i+j})p_i + (t_{i+1} - t_{i+j+1})p_{i+1} + t_{i-j}p_{i-j} + t_{i-j+1}p_{i-j+1}. \quad (6.10)$$

Similarly, the flowrate out of the boundary from cell i can be written as

$$q_{i,i+j} = (t'_i - t'_{i+j})p_i + (t'_{i+1} - t'_{i+j+1})p_{i+1} + (t'_{i-1} - t'_{i-j+1})p_{i-1}, \quad (6.11)$$

where t'_l is the transmissibility coefficient of cell l for flowrate calculation between cells i and $i + j$.

6.1.2 Analytical Solution

Consider an elliptic reservoir with a boundary as

$$\frac{x^2}{a^2} + \frac{y^2}{b^2} = 1, \quad (6.12)$$

where $a = \frac{1}{2}l$ and $b = \frac{1}{2}w$. Here l and w are the lengths of the ellipse in the x and y directions. We define the aspect ratio of the ellipse as l/w . The reservoir is an anisotropic medium with the permeability ratio of k_x/k_y , the source term q at the center and zero pressure on the elliptical outer boundary. The differential equation solution for the steady-state pressure distribution in the ellipse in Cartesian coordinates is given by

$$k_x \frac{\partial^2 p}{\partial x^2} + k_y \frac{\partial^2 p}{\partial y^2} = 0, \quad (6.13)$$

where the pressure is zero on the boundary of the ellipse, i.e.,

$$p = 0 \text{ at } \frac{x^2}{(l/2)^2} + \frac{y^2}{(w/2)^2} = 1. \quad (6.14)$$

Following D. W. Peaceman et al. [34], in Eq. 6.13, we make the change of variables defined by

$$u = (k_y/k_x)^{1/4} x \quad (6.15)$$

and

$$v = (k_x/k_y)^{1/4} y, \quad (6.16)$$

to obtain

$$\frac{\partial^2 p}{\partial u^2} + \frac{\partial^2 p}{\partial v^2} = 0. \quad (6.17)$$

The boundary condition is transformed to

$$p = 0 \text{ at } (k_x/k_y)^{1/2} \frac{u^2}{(l/2)^2} + (k_y/k_x)^{1/2} \frac{v^2}{(w/2)^2} = 1. \quad (6.18)$$

Note that the outer boundary is transformed to an ellipse which has an aspect ratio in the u - v plane that is different than the aspect ratio in the x - y plane. The lengths of the ellipse in the u and v directions are as follows:

$$l' = (k_y/k_x)^{1/4} l \quad (6.19)$$

and

$$w' = (k_x/k_y)^{1/4} w. \quad (6.20)$$

The aspect ratio of the outer boundary in the u - v plane is

$$\frac{l'}{w'} = \left(\frac{k_y}{k_x} \right)^{1/2} \frac{l}{w}. \quad (6.21)$$

Note that if the aspect ratio in the original plane is equal to $\sqrt{k_x/k_y}$, i.e., $l/w = \sqrt{k_x/k_y}$, then $l'/w' = 1$ and hence the outer boundary in the u - v plane is a circle and the solution to Eq. 6.13 in the u - v plane is radial. However, if $l/w \neq \sqrt{k_x/k_y}$, then the outer boundary in the u - v plane is an ellipse and the equipotential lines in the u - v plane are a set of concentric

ellipses, and as we get close to the circular well the equipotential line becomes a circle.

To solve Eq. 6.17 with the boundary condition given by Eq. 6.18, we transform the u - v coordinate to an elliptic coordinate system. After this point, we assume $(k_y/k_x)(l/w)^2 < 1$. However, we can follow a similar procedure for a case with $(k_y/k_x)(l/w)^2 > 1$. We make the change of variables given by

$$u = b \sinh \rho \sin \theta \quad (6.22)$$

and

$$v = b \cosh \rho \cos \theta, \quad (6.23)$$

where ρ is a nonnegative real number identifying each ellipse (similar to r for a circle), θ is a real number between 0 and 2π and b is a constant which is determined later based on the boundary ellipse. Let ρ_e denote the outer boundary ellipse (similar to r_e for a circle). Substituting Eqs. 6.22 and 6.23 into the Pythagorean trigonometric identity, gives

$$\sin^2 \theta + \cos^2 \theta = \frac{u^2}{b^2 \sinh^2 \rho_e} + \frac{v^2}{b^2 \cosh^2 \rho_e} = 1. \quad (6.24)$$

Now we wish to specify ρ_e and b in such a way that the boundary ellipse defined in Eq. 6.18 be the same as the ellipse in Eq. 6.24. Comparing Eq. 6.24 with the boundary ellipse defined in Eq. 6.18, gives

$$\begin{cases} (k_y/k_x)^{1/2} (l/2)^2 = b^2 \sinh^2 \rho_e; \\ (k_x/k_y)^{1/2} (w/2)^2 = b^2 \cosh^2 \rho_e. \end{cases} \quad (6.25)$$

Solving Eq. 6.25 for ρ_e and b , we have

$$\tanh^2 \rho_e = (k_y/k_x) (l/w)^2, \quad (6.26)$$

and

$$b^2 = (k_x/k_y)^{1/2} (w/2)^2 - (k_y/k_x)^{1/2} (l/2)^2. \quad (6.27)$$

Since the change of variables given in Eqs. 6.22 and 6.23 is a conformal mapping [34], Eq. 6.17

can be written in the elliptic coordinate system as follows:

$$\frac{\partial^2 p}{\partial \rho^2} + \frac{\partial^2 p}{\partial \theta^2} = 0. \quad (6.28)$$

The boundary condition given in Eq. 6.18 is transformed to

$$p = 0 \text{ at } \rho = \rho_e. \quad (6.29)$$

D. W. Peaceman et al. [34] showed that the solution to Eq. 6.17 is a set of concentric ellipse isobars in the u - v plane, pressure is constant on any ellipse corresponding to a given fixed ρ and the solution to Eq. 6.28 is only a function of ρ and does not depend on θ . Therefore, if we integrate Eq. 6.28, the following expression for the pressure is obtained:

$$p = C(\rho_e - \rho). \quad (6.30)$$

In Appendix A, it is shown that the constant C is given by:

$$C = \frac{q\mu}{2\pi h (k_x k_y)^{1/2}}. \quad (6.31)$$

Using Eq. 6.31 in Eq. 6.30, the solution to Eq. 6.28 is given by

$$p = \frac{q\mu}{2\pi h (k_x k_y)^{1/2}} (\rho_e - \rho), \quad (6.32)$$

where Eq. 6.26 indicates that

$$\rho_e = \tanh^{-1} \left(\frac{l}{w} \sqrt{\frac{k_y}{k_x}} \right). \quad (6.33)$$

6.1.3 Convergence Behavior

To investigate the convergence behavior of the L-method for the grid refinement system, we compute the discrete L^2 norm of the pressure error. The normalized discrete L^2

norm is defined by the following expression.

$$e = \left(\frac{1}{A} \sum_{i=1}^N A_i (p_{ex,i} - p_i)^2 \right)^{1/2}, \quad (6.34)$$

where, N is the number of cells, A_i is the area of cell i , $A = \sum_i A_i$ and $p_{ex,i}$ is the pressure evaluated analytically from Eq. 6.32 at the same position as the center of the cell i , where we compute p_i numerically. Fig. 6.3 shows the convergence behaviour of the L-method with different permeability ratios. All cases in Fig. 6.3 have the aspect ratio of 1. Note that by

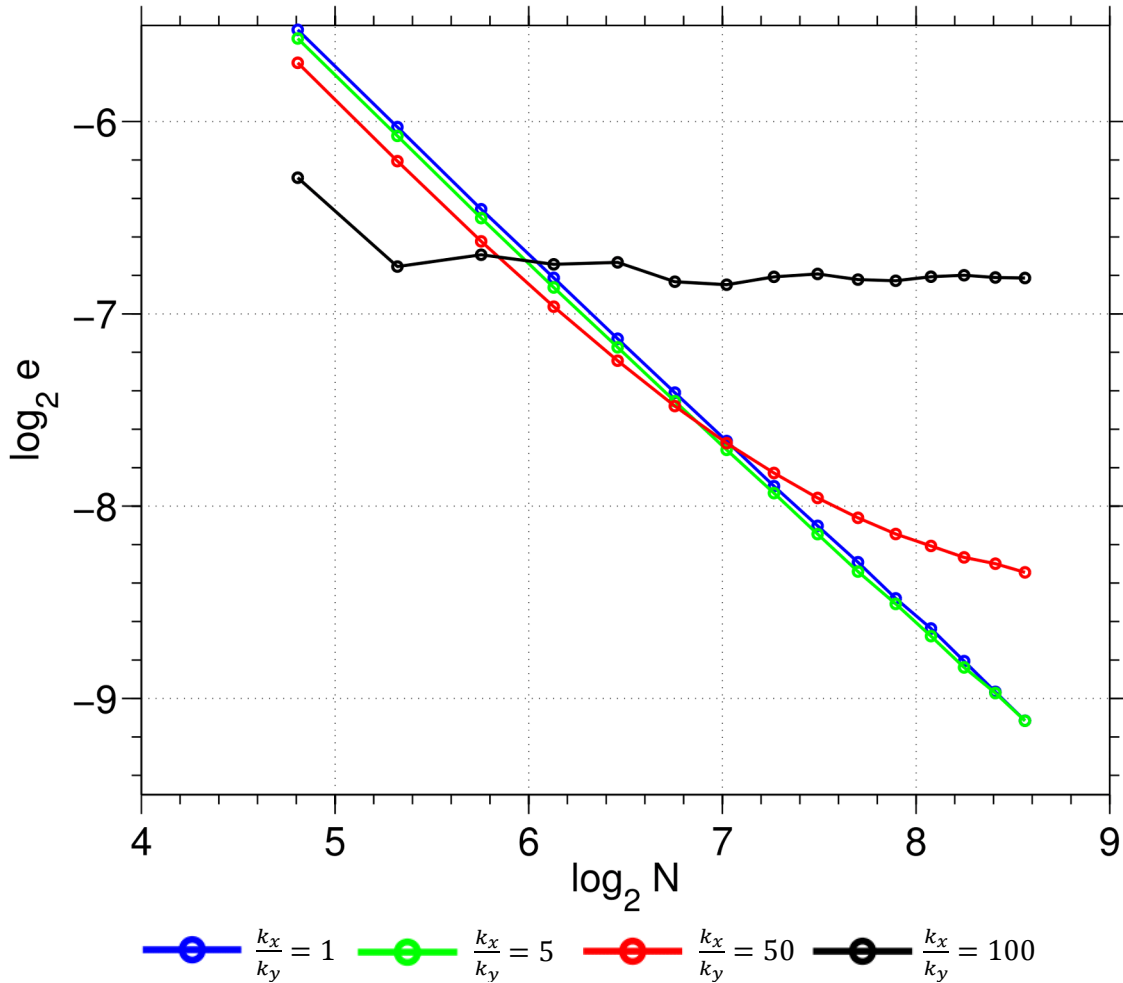


Figure 6.3: Convergence behaviour of the L-method, aspect ratio equals 1.

increasing the number of cells (N), the size of each cell decreases in both directions with the same ratio. If we define h in such a way that $A = h^2$, where A is the area of the cell, then

$N \propto 1/h^2$. The slopes of the cases with the permeability ratio 1 and 5 are close to -1, which indicates the convergence rate of these two cases is close to $\mathcal{O}(h^2)$. However, increasing the permeability ratio to 50 decreases the convergence rate. The case with the permeability ratio 100 does not converge.

Fig. 6.4 shows the convergence behavior of the L-method for two cases with the aspect ratios of 2 and 7. As we see, increasing the aspect ratio, improves the convergence rate of the case with high permeability ratio.

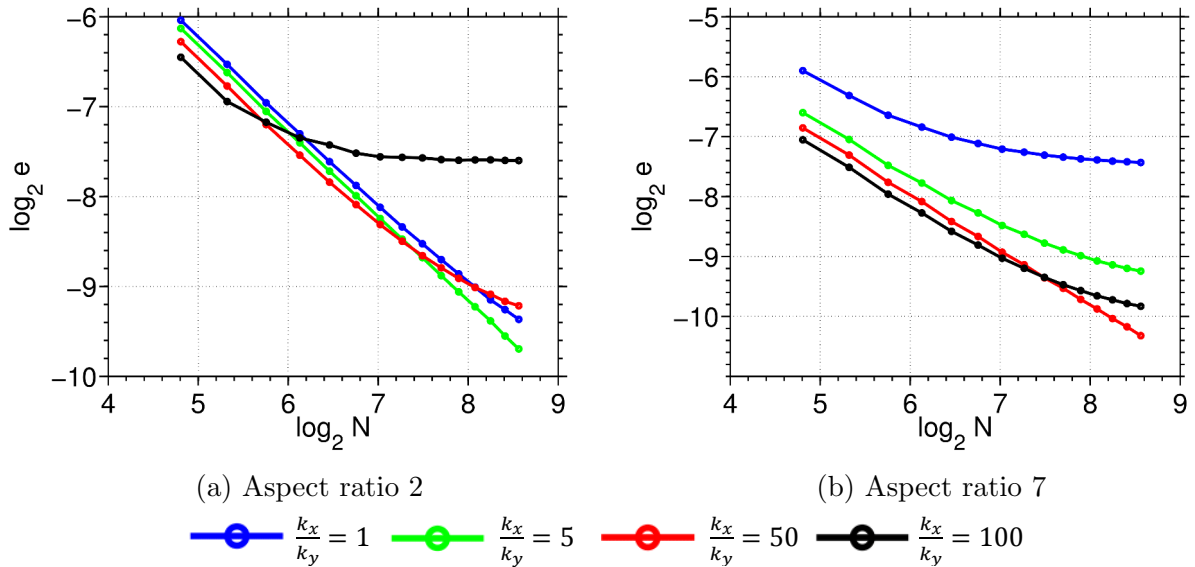


Figure 6.4: Convergence behaviour of the L-method.

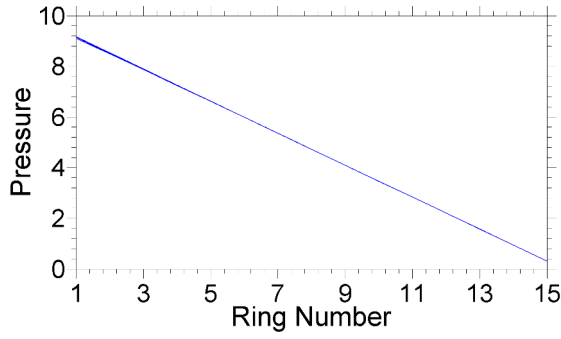
6.2 Numerical Tests for the L-method

To see the effects of the violation of the discrete maximum principle, we have conducted tests on homogeneous and heterogenous media with hexadecagonal grids. In these computations, 16 equal point sources are located in the grid cells of the first ring and zero Dirichlet boundary conditions are imposed on the boundary of the last hexadecagon. To construct a heterogeneous medium, we assume that $\log(k_x)$ of each grid cell varies randomly based on a Gaussian distribution with the mean of 6 and the standard deviation of 1.6. The conditions of Table 5.6 represent sufficient conditions for monotonicity but there exist no proof that they are necessary for monotonicity. Thus, even when they are not satisfied, a

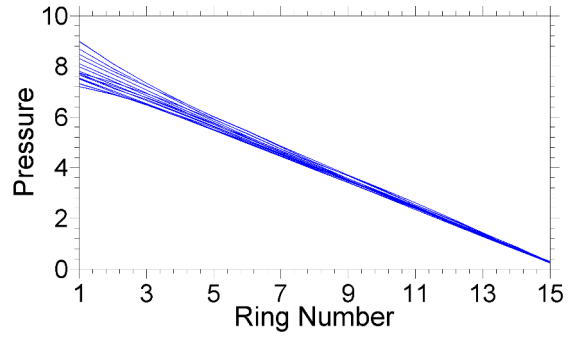
MPFA method may yield non-oscillatory pressure solutions.

Each curve in Figs. 6.5 and 6.6 represents the pressure profile along a particular ray in the r-direction emanating from the center of the refined Cartesian gridblock. When the aspect ratio is equal to the square root of permeability ratio, i.e., when Eq. 5.88 holds, as noted earlier, each ellipse is an equipotential surface and we expect the maximum monotonicity range. In Figs. 6.5a and 6.6c pressures at the center of all 16 cells in each ring of sixteen gridblocks are equal. However, for cases with a high permeability ratio and low aspect ratio, i.e., when $(\Delta x/\Delta y)\sqrt{k_y/k_x}$ is not close to unity, small oscillations can be seen close to the well and a one to the boundary, as shown in Figs. 6.5f and 6.6f. The numerical results for a homogeneous media show that even with a high permeability ratio, no oscillation appears in the near-well region, but we see negative potentials close to the boundaries; see Figs. 6.5c, 6.5e and 6.6e. Results of similar cases with heterogeneities show potential oscillations close to the well region; see Figs. 6.5d, 6.5f and 6.6f.

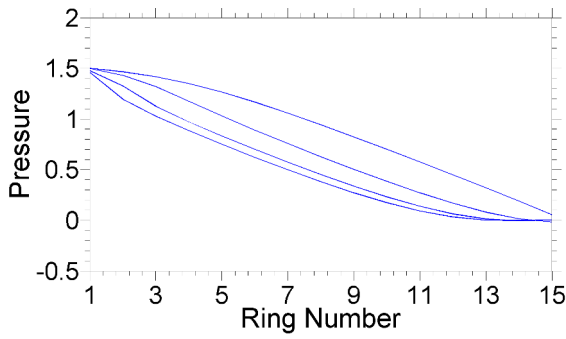
Fig. 6.7 shows the results of similar cases shown in Figs. 6.6d and 6.6f but with different aspect ratio. By modifying the aspect ratio in such a way that $\sqrt{k_x/k_y} = \Delta x/\Delta y$, solutions show no non-physical behavior.



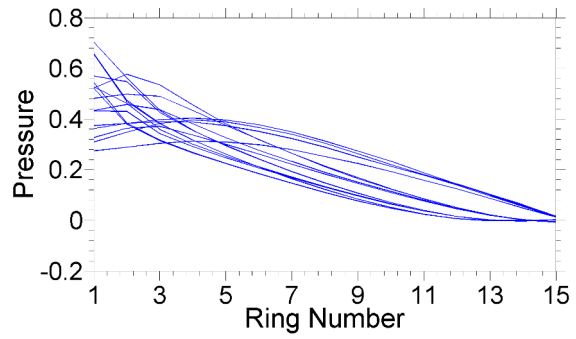
(a) Homogeneous, $k_x/k_y = 1$



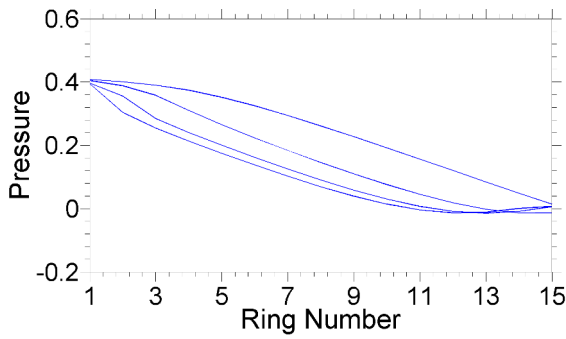
(b) Heterogeneous, $k_x/k_y = 1$



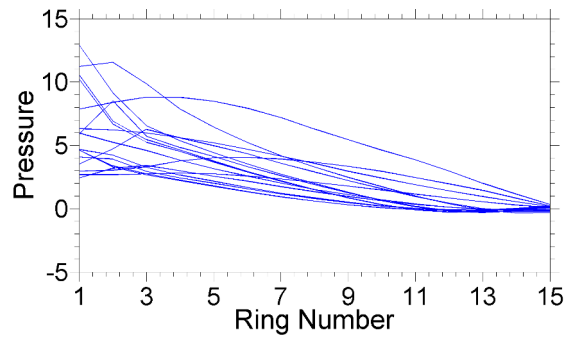
(c) Homogeneous, $k_x/k_y = 20$



(d) Heterogeneous, $k_x/k_y = 20$

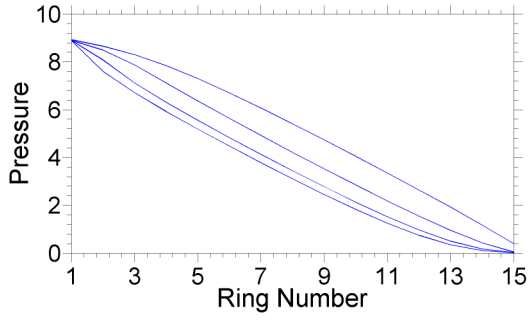


(e) Homogeneous, $k_x/k_y = 100$

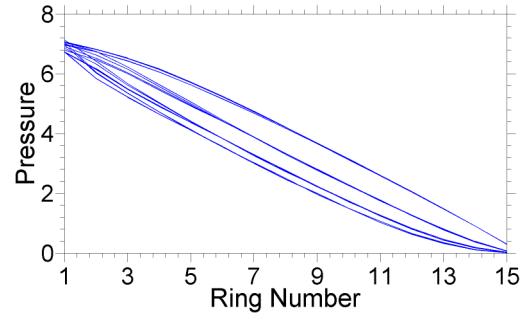


(f) Heterogeneous, $k_x/k_y = 100$

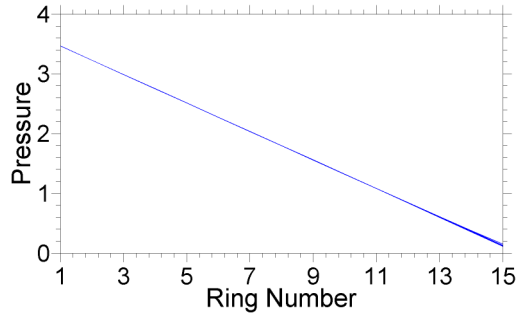
Figure 6.5: Pressure solutions for grid cells with the aspect ratio of 1 and a geometric ratio of 1.3.



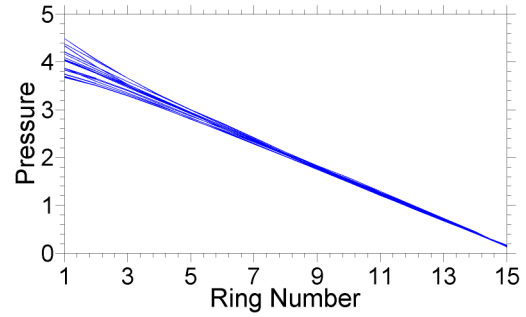
(a) Homogeneous, $k_x/k_y = 1$



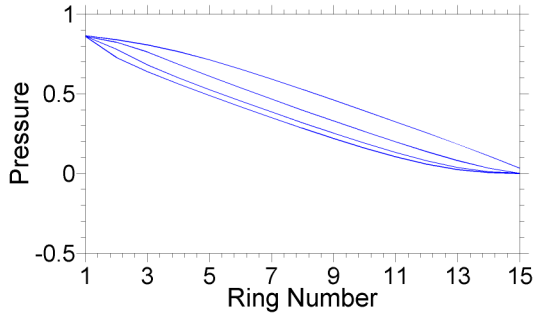
(b) Heterogeneous, $k_x/k_y = 1$



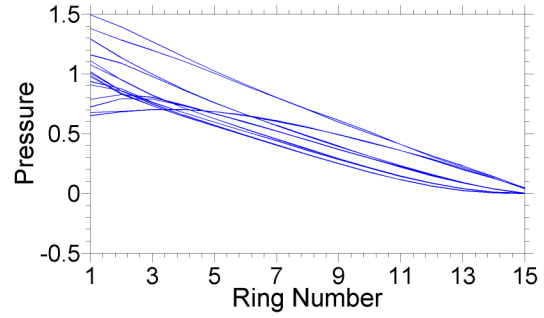
(c) Homogeneous, $k_x/k_y = 9$



(d) Heterogeneous, $k_x/k_y = 9$

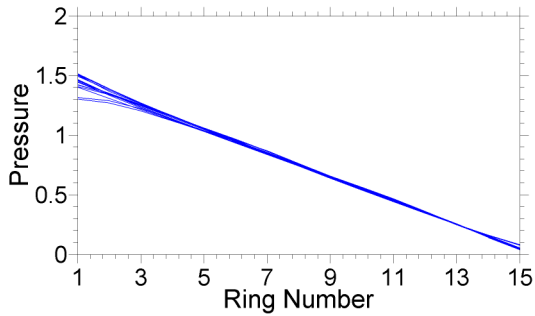


(e) Homogeneous, $k_x/k_y = 100$

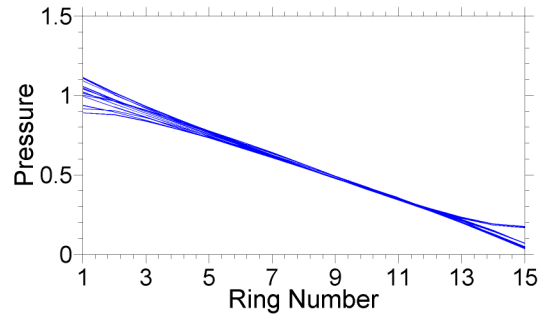


(f) Heterogeneous, $k_x/k_y = 100$

Figure 6.6: Pressure solutions for grid cells with the aspect ratio of 3 and the geometric ratio of 1.3.



(a) $\Delta x/\Delta y = 4.47$, $k_x/k_y = 20$



(b) $\Delta x/\Delta y = 10$, $k_x/k_y = 100$

Figure 6.7: Pressure solutions for grid cells of a heterogeneous medium and the geometric ratio of 1.3, $\sqrt{k_x/k_y} = \Delta x/\Delta y$.

CHAPTER 7

CARTESIAN GRID REFINEMENT

We consider a type of Cartesian refinement where each side of a rectangular cell is connected to either one or two refined cells. The simple case, shown in Fig. 7.1a, consists of 18 base rectangular cells. choosing 16 cells in the bottom row is an example. Connecting cells 3, ..., 18 to cell 2 can cause numerical error in the pressure results. Therefore, to more accurately model flow from cells 3, ..., 18 through cell 2 to cell 1, we refine cell 2 by the following procedure. First, Cell 2 is divided into four equal cells. Then, each fine cell on the right is divided into 4 equal cells. We continue this procedure until each refined grid in the bottom row inside base cell 2 is connected to two neighboring cells (cells 3 to 18). In Fig. 7.1b, the refined Cartesian cells are shown by red. Note that the aspect ratio ($(\Delta x/\Delta y)$ for a vertical well and $(\Delta z/\Delta y)$ for a horizontal well in the x -direction) of the refined cells is equal to the aspect ratio of the base cell. As you can see in this example, each cell has at most two neighbors on each of its side.

7.1 Monotonicity Criteria

We use the MPFA method to compute the flux between refined cells. In the proposed Cartesian refinement, there are two different interaction regions between a collection of grid cells with one common point. Fig. 7.2 shows an interaction region between cells P_1, P_2 and P_3 and Fig. 7.3 shows two interaction regions between cells P_1, P_2, P_3 and P_3, P_4, P_1 . We use the L-method for the interaction regions in Fig. 7.3.

We calculate the transmissibility coefficients of these two interaction regions, based on the assumption that the base cell has the permeability values of k_x and k_y with an aspect ratio of $AR = \Delta x/\Delta y$. Since the aspect ratio of refined cells is equal to the aspect ratio of

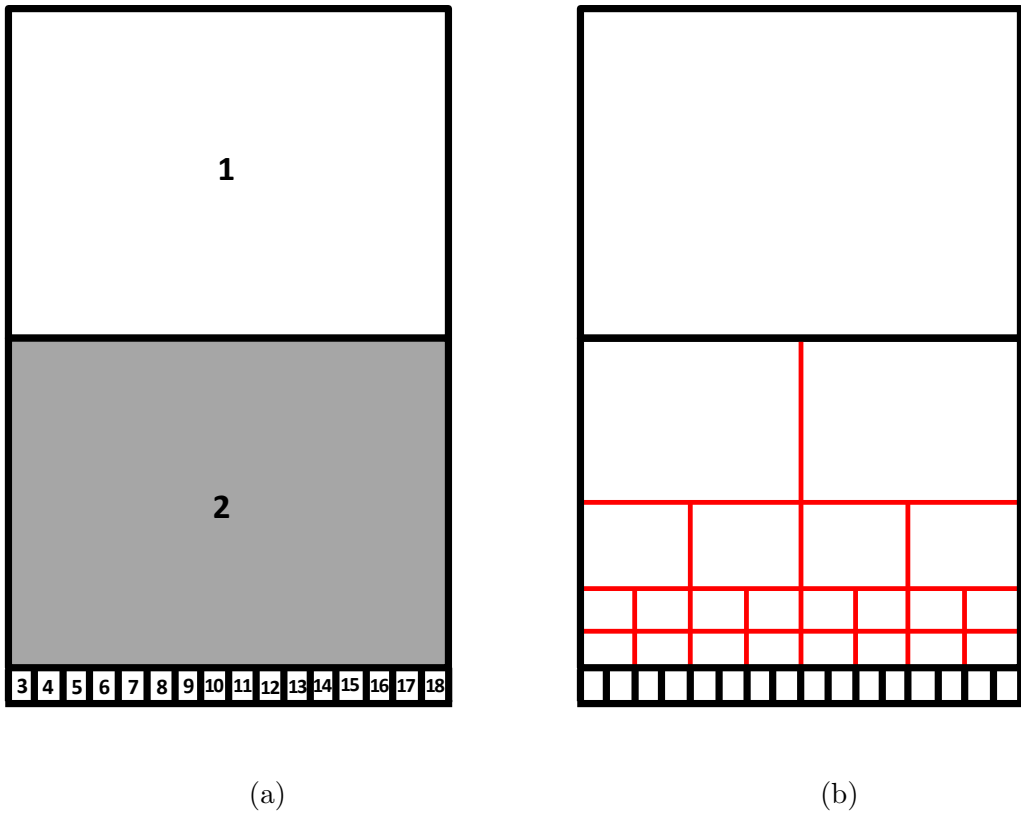


Figure 7.1: 18 rectangular cells in the x - y plane with y in the vertical direction, (a) before and (b) after refinement.

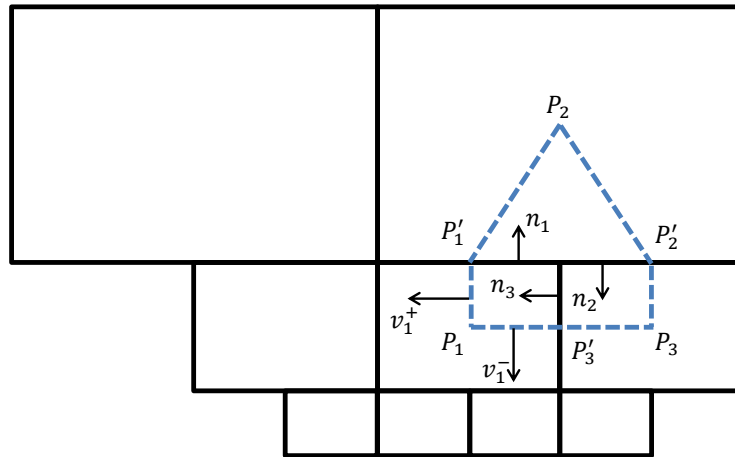


Figure 7.2: An interaction region containing three cells.

the base cell, each refined cell has the same permeability values and aspect ratio.

Considering the triangular interaction region shown in Fig. 7.2, the unit normal vec-

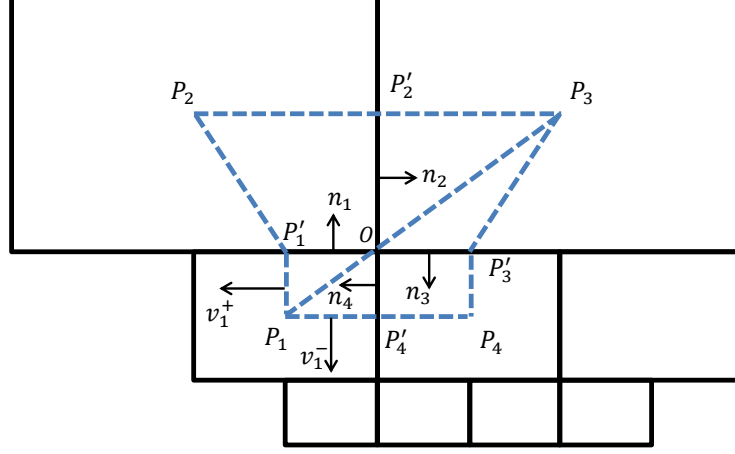


Figure 7.3: An interaction region containing four cells.

tors, n_i , $i = 1, 2, 3$, are simply computed as $n_1 = [0, 1]^T$, $n_2 = [0, -1]^T$ and $n_3 = [-1, 0]^T$. If the width of the cell centered at P_1 is Δx_1 , then vectors v_l^\pm are computed as follows:

$$v_1^- = v_3^+ = \begin{bmatrix} 0 \\ -\Delta x_1/2 \end{bmatrix}, v_1^+ = -v_3^- = \begin{bmatrix} -\Delta x_1/(2AR) \\ 0 \end{bmatrix},$$

$$v_2^- = \begin{bmatrix} -\Delta x_1/AR \\ \Delta x_1/2 \end{bmatrix}, v_2^+ = \begin{bmatrix} \Delta x_1/AR \\ \Delta x_1/2 \end{bmatrix}. \quad (7.1)$$

The area of sub-interfaces are $A_1 = A_2 = \Delta x_1/2$ and $A_3 = \Delta x_1/(2AR)$ and the triangle areas,

$$F_l = \frac{1}{2} \|v_l^-\| \|v_l^+\| \sin(\beta), \quad l = 1, 2, 3, \quad (7.2)$$

where β is the angle between $\|v_l^-\|$ and $\|v_l^+\|$. Then, from Eq. 7.2 we have

$$F_1 = F_3 = \Delta x_1^2/(8AR), \quad (7.3)$$

and,

$$F_2 = \Delta x_1^2/(2AR). \quad (7.4)$$

Following the definition of w_{il}^{pm} in Eq. 4.24, represented as follows:

$$w_{il}^{\pm} = \frac{n_i^T A_i K_l v_l^{\pm}}{2F_l}, \quad (7.5)$$

the non-zero scalar coefficients for the triangular interaction region are as follows:

$$\begin{aligned} w_{23}^+ &= -w_{11}^- = ARk_y, \\ w_{22}^+ &= w_{22}^- = -\frac{AR}{4}k_y, \\ w_{12}^+ &= w_{12}^- = \frac{AR}{4}k_y, \\ w_{31}^+ &= -w_{33}^- = \frac{k_x}{AR}. \end{aligned} \quad (7.6)$$

The rest of the scalar coefficients are zero. We use Eqs. 4.31, 4.32, 4.33 and 4.34 to construct matrices A, B, C and D, as follows:

$$A = \begin{pmatrix} -(w_{11}^+ + w_{11}^-) & 0 & 0 \\ 0 & -(w_{22}^+ + w_{22}^-) & 0 \\ 0 & 0 & -(w_{33}^+ + w_{33}^-) \end{pmatrix} = \begin{pmatrix} ARk_y & 0 & 0 \\ 0 & \frac{AR}{2}k_y & 0 \\ 0 & 0 & \frac{k_x}{AR} \end{pmatrix}, \quad (7.7)$$

$$B = \begin{pmatrix} w_{11}^- & 0 & w_{11}^+ \\ w_{22}^+ & w_{22}^- & 0 \\ 0 & w_{33}^+ & w_{33}^- \end{pmatrix} = - \begin{pmatrix} ARk_y & 0 & 0 \\ \frac{AR}{4}k_y & \frac{AR}{4}k_y & 0 \\ 0 & 0 & \frac{k_x}{AR} \end{pmatrix}, \quad (7.8)$$

$$C = \begin{pmatrix} 0 & -(w_{12}^+ + w_{12}^-) & 0 \\ 0 & 0 & -(w_{23}^+ + w_{23}^-) \\ -(w_{31}^+ + w_{31}^-) & 0 & 0 \end{pmatrix} = - \begin{pmatrix} 0 & \frac{AR}{2}k_y & 0 \\ 0 & 0 & ARk_y \\ \frac{k_x}{AR} & 0 & 0 \end{pmatrix}, \quad (7.9)$$

$$D = \begin{pmatrix} w_{12}^+ & w_{12}^- & 0 \\ 0 & w_{23}^+ & w_{23}^- \\ w_{31}^- & 0 & w_{31}^+ \end{pmatrix} = \begin{pmatrix} \frac{AR}{4}k_y & \frac{AR}{4}k_y & 0 \\ 0 & ARk_y & 0 \\ 0 & 0 & \frac{k_x}{AR} \end{pmatrix}. \quad (7.10)$$

By substituting the matrices in Eqs. 7.7- 7.10 in Eq. 5.37, we have the transmissibility matrix for the interaction region shown in Fig. 7.2 as follows:

$$T_{3 \times 3} = \begin{pmatrix} \frac{1}{6}ARk_y & -\frac{1}{3}ARk_y & \frac{1}{6}ARk_y \\ -\frac{1}{6}ARk_y & \frac{1}{3}ARk_y & -\frac{1}{6}ARk_y \\ -\frac{1}{2}k_x/AR & 0 & \frac{1}{2}k_x/AR \end{pmatrix} \quad (7.11)$$

The transmissibility matrix for the interaction regions shown in Fig. 7.3 are obtain similarly. We use Eqs. 4.54, 4.55, 4.57 and 4.58 to construct matrices A, B, C and D for each interaction region. To compute these matrices, we also need to compute x^\pm , given in Eq. 4.49, for interaction regions between cells (P_1, P_2, P_3) and (P_3, P_4, P_1) denoted respectively as x_1^\pm and x_2^\pm , as follows:

$$x_1^\pm = \frac{v_5 \cdot v_2^\pm}{2F_2}, \quad (7.12)$$

$$x_2^\pm = \frac{v_6 \cdot v_4^\pm}{2F_4}, \quad (7.13)$$

where, v_5 and v_6 , that are not shown in Fig. 7.3, are as follows

$$v_5 = O - P_2 = \begin{bmatrix} \Delta x_1 \\ -\Delta x_1/AR \end{bmatrix}, \quad (7.14)$$

and,

$$v_6 = O - P_4 = \begin{bmatrix} -\Delta x_1/2 \\ \Delta x_1/(2AR) \end{bmatrix}, \quad (7.15)$$

Eqs. 7.16 and 7.17 show the entries of the transmissibility matrices for the both interaction regions in Fig. 7.3, computed from Eq. 4.64. For the interaction region between (P_1, P_2, P_3) ,

we have

$$(T_{3 \times 2})_1 = \begin{pmatrix} \frac{1}{3}ARk_y & -\frac{1}{4}ARk_y & -\frac{1}{12}ARk_y \\ 0 & \frac{1}{2}k_x/AR & -\frac{1}{2}k_x/AR \end{pmatrix}, \quad (7.16)$$

and for the interaction region between (P_3, P_4, P_1) , we have

$$(T_{3 \times 2})_2 = \begin{pmatrix} \frac{1}{12}ARk_y & \frac{1}{4}ARk_y & -\frac{1}{3}ARk_y \\ -\frac{1}{2}k_x/AR & 0 & \frac{1}{2}k_x/AR \end{pmatrix}. \quad (7.17)$$

In the Cartesian grid refinement used in this work (Fig. 5.1), we can divide cells into two categories based on neighboring cells. In both Figs. 7.4 and 7.5, Cell i shares a boundary with two smaller cells on the bottom. Considering these two boundary cells of cell i , the cell on the left is placed in category one and the right one is placed in category two. Figs. 7.4 and 7.5 show the cells from categories one and two in blue.

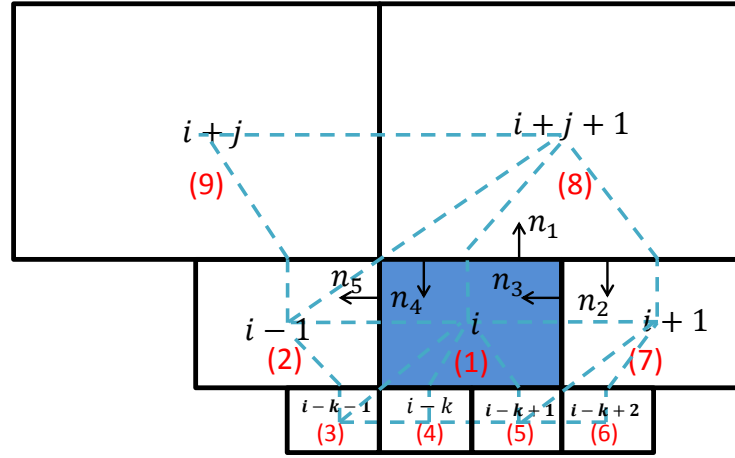


Figure 7.4: A cell from category one and its neighboring cells.

In these two figures, the black indices are parts of the global numbering and indices in parenthesis show the local numbering. For both cases (Figs. 7.4 and 7.5), the four neighboring cells on the bottom are labeled $i-k-1$ to $i-k+2$ and the two cells on the top are labeled $i+j$ and $i+j+1$. k is the number of cells from cell i to its left bottom neighboring cell and j is the number of cells from cell i to its top neighboring cell. Here, variables k and j are

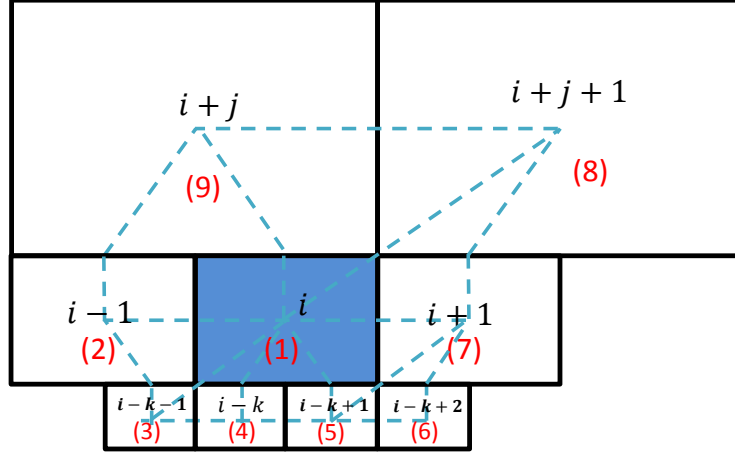


Figure 7.5: A cell from category two and its neighboring cells.

not constant and even when we move from left to right in one row, considering the center cell as cell i , variables k and j are reduced by half.

We write the general form of the mass conservation equation for grid cell i as follows:

$$\sum_{l=1}^9 t_l^i p_l^i = q_i \text{ for } i = 1, 2, \dots, n, \quad (7.18)$$

where t_l^i is the transmissibility of neighboring cell l used to approximate the total flux out of cell i , q_i is the source term of cell i , p_l^i is the pressure of the neighboring cell l of cell i and n is the total number of cells. In both cases shown in Figs. 7.4 and 7.5, there are eight interaction regions between cell i and other neighboring cells including 6 interaction regions where we use the L-method for flux calculations and 2 interaction regions, where we use the O-method. We combine the transmissibility coefficients computed from these interaction regions which are given by Eqs. 7.11, 7.16 and 7.17 to determine t_l^i for each cell.

For example, in category one shown in Fig. 7.4, we determine the effect of cell (8) on the total flux out of cell (1) to calculate t_8^i . Cell (8) is included in two interaction regions. The interaction region between cells (1), (8) and (7) is shown in Fig. 7.4. The entries in the second column of matrix $T_{3 \times 3}$ in Eq. 7.11 are the transmissibility coefficients of the potential of cell (8) in Fig. 7.4. The first entry associated with sub-interface 1 and the third entry associated

with sub-interface 3. Note that the direction of the flux through sub-interface 3 is from cell (7) to cell (1) and to change the flux direction we multiply the third row of matrix $T_{3 \times 3}$ by -1. The interaction region between cells (1), (2) and (8) is shown in Fig. 7.4, where we use the L-method to compute the transmissibility coefficients. Comparing Fig. 7.4 with Fig. 7.3, the interaction region between cells (1), (2) and (8) is similar to the interaction region between cells P_4 , P_1 and P_3 in Fig. 7.3. Then, we use the corresponding transmissibility matrix for this interaction region, $(T_{3 \times 2})_2$, given in Eq. 7.17 to compute the transmissibility coefficients. The entries in the first column of matrix $T_{3 \times 2,2}$ are the transmissibility coefficients of the potential of cell (8) in Fig. 7.4. The first entry associated with sub-interface 4 and the second entry associated with sub-interface 5 in Fig. 7.4. Here, the direction of the flux through sub-interface 4 is from cell (8) to cell (1) and to change the flux direction to out of cell (1), we multiply the first row of matrix $(T_{3 \times 2})_3$ by -1. Therefore, the transmissibility of neighboring cell (8) used to approximate the total flux out of cell i is calculated as follows:

$$t_8^i = -\frac{1}{3}ARk_y - \frac{1}{4}ARk_y = -\frac{7}{12}ARk_y \quad (7.19)$$

Similarly, the other non-zero transmissibilities for the case shown in Fig. 7.4 are as follows:

$$t_1^i = \frac{5}{3}ARk_y + 2k_x/AR \quad (7.20)$$

$$t_2^i = \frac{1}{12}ARk_y - k_x/AR \quad (7.21)$$

$$t_4^i = -\frac{2}{3}ARk_y \quad (7.22)$$

$$t_5^i = -\frac{2}{3}ARk_y \quad (7.23)$$

$$t_7^i = -\frac{1}{4}ARk_y - k_x/AR \quad (7.24)$$

$$t_9^i = -\frac{1}{12}ARk_y \quad (7.25)$$

In the second category shown in Fig. 7.5, the value of t_2^i is interchanged with the value of t_7^i

and the value of t_3^i is interchanged with the value of t_6^i .

We introduce the vector quantities $p = [p_1, p_2, \dots, p_N]^T$ and $q = [q_1, q_2, \dots, q_N]^T$ where p_i is the potential of cell i . Then, Eq. 7.18 can be written in matrix form as $Ap = q$, where A is the matrix of coefficients. Comparing the local ordering and the global ordering of the cells in both categories in Figs. 7.4 and 7.5, the i th row of matrix A is written as

Table 7.1: The nonzero entries of the i th row of matrix A .

Column index	$i-k$	$i-k+1$	$i-1$	i	$i+1$	$i+j$	$i+j+1$
	t_4^i	t_5^i	t_2^i	t_1^i	t_7^i	t_9^i	t_8^i

To derive criteria that ensure matrix A is monotone, we apply Theorem 1 from the “Polygonal Near-Well Grid Refinement” section. Matrix A is split into matrices B and C in such a way that $A = B - C$. We specify matrix B as the tridiagonal part of the matrix A . The nonzero entries of the i th row of the matrix B are shown in Table 7.2.

Table 7.2: The nonzero entries of the i th row of matrix B .

Column index	$i-1$	i	$i+1$
	t_2^i	t_1^i	t_7^i

From the discussion of Poole’s result in section 5.2, matrix $B = [b_{ij}]$ is an M-matrix, if

$$\sum_{j=1}^n b_{ij} > 0 \text{ for } i = 1, 2, \dots, n, \tag{7.26}$$

$b_{ij} \leq 0$ whenever $i \neq j$ and $b_{ii} > 0$ for each i . Therefore, the conditions given in inequalities

$$t_2^i + t_1^i + t_7^i > 0, \tag{7.27}$$

$$t_1^i > 0, \tag{7.28}$$

$$t_2^i, t_7^i \leq 0, \tag{7.29}$$

are sufficient to guarantee that B is an M-matrix and hence $B^{-1} \geq 0$.

Based on the structures of matrices A and B given in Tables. 7.1 and 7.2, the i th row of matrix $C = B - A$ is given by

Table 7.3: The nonzero entries of the i th row of matrix C .

Column index	$i-k$	$i-k+1$	$i+j$	$i+j+1$
	$-t_4^i$	$-t_5^i$	$-t_9^i$	$-t_8^i$

As the last criterion in Theorem 1 in section 5.1, we establish conditions that are sufficient to ensure that $CB^{-1} \geq 0$. We assume that inequalities 7.27, 7.28 and 7.29 hold, so $B^{-1} \geq 0$. Then, conditions $t_l^i \leq 0$ for $l = 4, 5, 8, 9$ ($C \geq 0$) are sufficient to guarantee $CB^{-1} \geq 0$. These conditions are changed to strict inequalities to ensure CB^{-1} is irreducible. The final criteria that guarantee matrix A is monotone are

$$t_2^i + t_1^i + t_7^i > 0, \quad (7.30)$$

$$t_1^i > 0, \quad (7.31)$$

$$t_l^i < 0 \text{ for } l = 2, 4, 5, 7, 8, 9. \quad (7.32)$$

Substituting transmissibilities from Eqs. 7.20 to 7.25 into inequalities 7.27, 7.28 and 7.29 shows all inequalities hold for all AR , k_x and k_y , except for $t_2^i < 0$. To ensure $t_2^i < 0$, AR , k_x and k_y must be such that

$$t_2^i = \frac{1}{12}ARk_y - k_x/AR < 0, \quad (7.33)$$

or equivalently,

$$\left(\frac{\Delta x}{\Delta y}\right)^2 \frac{k_y}{k_x} < 12. \quad (7.34)$$

Therefore, if Eq. 7.34 holds, the MPFA method used to compute the flux in the proposed Cartesian refinement is guaranteed to be monotone. Eq. 7.34 is valid when the cells are refined in the y -direction, as shown in Fig. 7.1. To determine the sufficient monotonicity criteria for Cartesian grid refinement in the x -direction, as shown in Fig. 7.6, we can simply replace the x -axis with y -axis. Therefore, following the inequality in Eq. 7.34 for refinement

in the y -direction, the sufficient monotonicity criteria for Cartesian grid refinement in the x -direction is given as follows:

$$\left(\frac{\Delta y}{\Delta x}\right)^2 \frac{k_x}{k_y} < 12. \quad (7.35)$$

Considering both refinements in the x and y directions, using Eqs. 7.34 and 7.35, we have

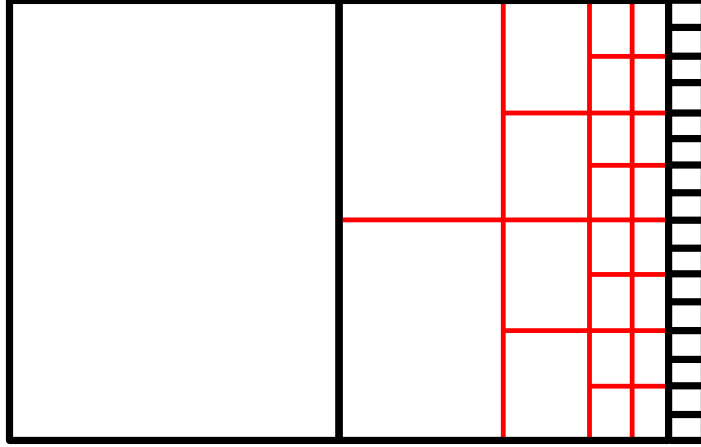


Figure 7.6: Cartesian grid refinement in the x -direction.

the following sufficient condition that guarantees the refinement is monotone:

$$\frac{1}{12} < \left(\frac{\Delta x}{\Delta y}\right)^2 \frac{k_y}{k_x} < 12. \quad (7.36)$$

Comparing the inequality in Eq. 7.36 with the monotonicity regions of hexadecagonal grids using the L-method shown in Fig. 5.16a shows that if the L-method for a hexadecagonal grid is inside the monotonicity region, then the inequality 7.36 holds. Therefore, if a case with hybrid grid refinement is inside or close to the monotonicity regions of the L-method shown in Fig. 5.16a, the Cartesian grid refinement is guaranteed to be monotone.

7.2 Convergence

To investigate the convergence behavior of the L-method for the hybrid grid refinement system presented in Fig. 3.2 and represented here as Fig. 7.7c, we follow a similar procedure shown in Chapter 6, as follows. We modify the grid refinement system by adjusting N_θ based on N_r , in such a way that the width (average length of the two bases) to

height ratio of trapezoidal cells stays constant. For a given N_r , we compute N_θ using Eq. 6.8, represented as follows:

$$N_\theta = \left\lceil \frac{\pi}{\tan^{-1} \left(\gamma \left(1 - \frac{2(l_w)^{1/N_r}}{(l_{max})^{1/N_r} + (l_w)^{1/N_r}} \right) \right)} \right\rceil. \quad (7.37)$$

However, there is a limitation in the number of divisions in the angular direction in the polygonal grid refinement. The hybrid refinement is constructed by combining the polygonal and Cartesian refined cells. The base coarse gridblock containing a well, can be refined into any even number of gridblocks greater than or equal to four with the number of refinement in the θ -direction equal to 2^i , where i is a positive integer greater than or equal to 2. Fig. 7.7 shows 4 examples of grid refinements with $i = 2, 3, 4, 5$.

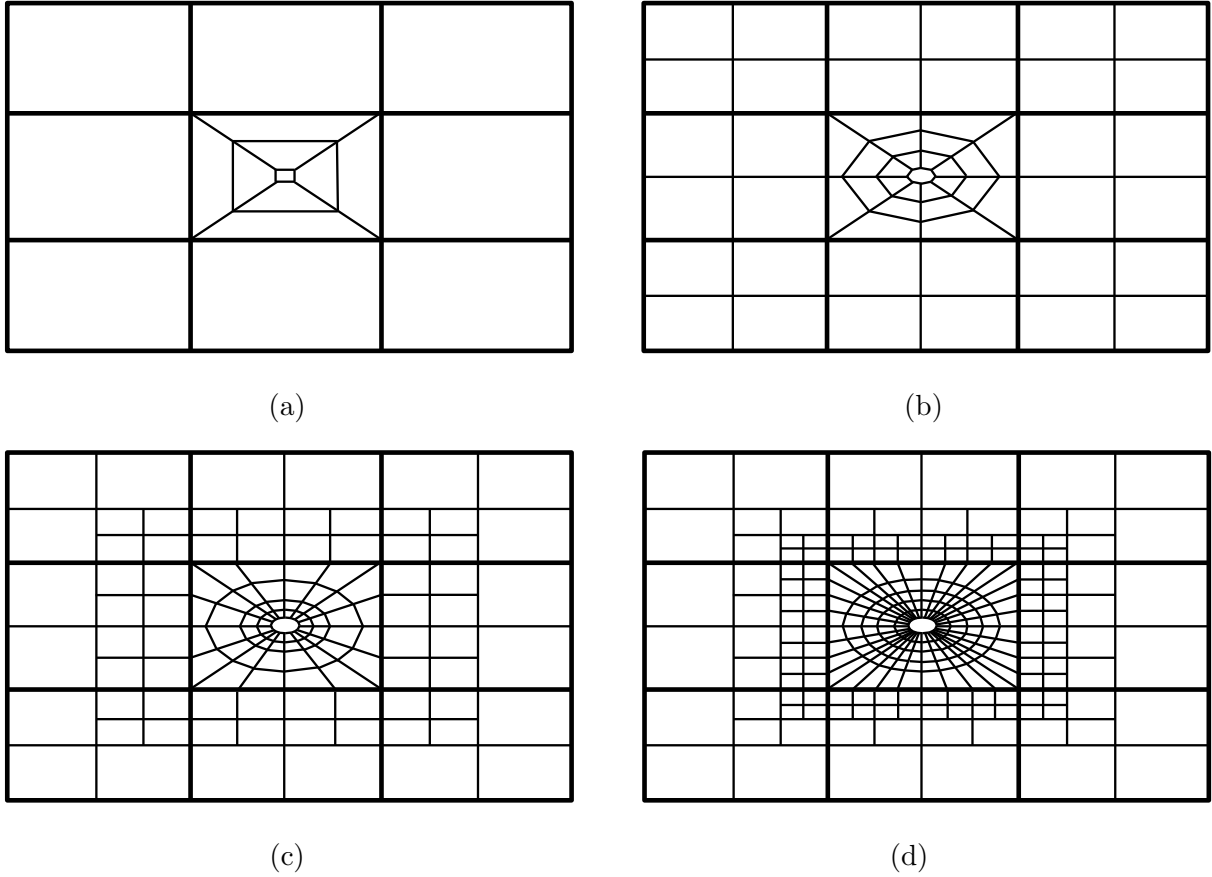


Figure 7.7: Hybrid grid refinements with (a) 4, (b) 8, (c) 16 and (d) 32 divisions in the θ direction.

We use Eq. 6.32, represented in Eq. 7.38, to obtain the analytical solution.

$$p = \frac{q\mu}{2\pi h (k_x k_y)^{1/2}} (\rho_e - \rho), \quad (7.38)$$

where

$$\rho_e = \tanh^{-1} \left(\frac{l}{w} \sqrt{\frac{k_y}{k_x}} \right). \quad (7.39)$$

However, this solution considers an elliptical boundary with zero pressure. The cases shown in Fig. 7.7 have rectangular boundaries. To have a more accurate discrete solution, we add 16 cells around the hybrid grid cells, shown in light green in Fig. 7.8. The outer boundaries of these cells are specified in such a way that all vertices are located on the outer elliptical boundary given by Eq. 6.12. To implement the zero pressure on the boundary, we follow the procedure presented in section 6.1.1, where we use imaginary cells around the boundary.

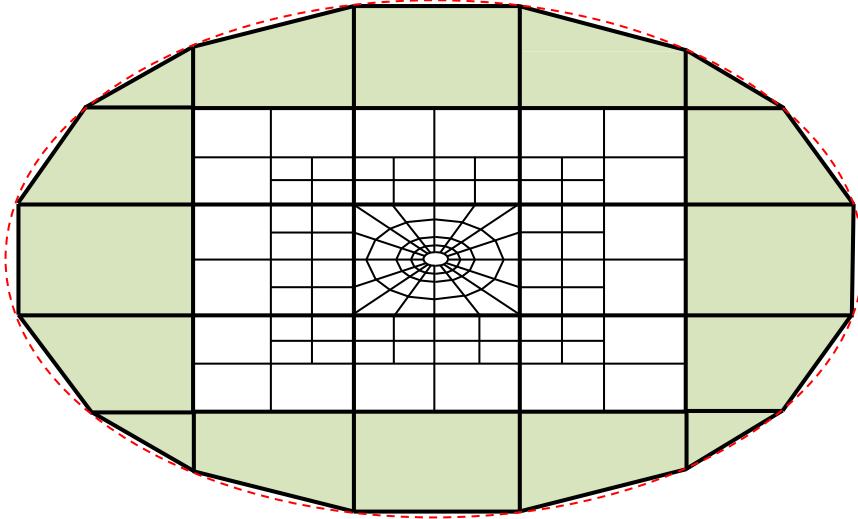


Figure 7.8: A hybrid grid refinement with 16 divisions in the θ direction with the modified boundary.

To investigate the convergence behavior of the L-method for the grid refinement system, we compute the normalized discrete L^2 norm of the pressure error, which is defined

by Eq. 6.34 and represented as follows:

$$e = \left(\frac{1}{A} \sum_{i=1}^N A_i (p_{ex,i} - p_i)^2 \right)^{1/2}, \quad (7.40)$$

where, N is the number of cells, A_i is the area of cell i , $A = \sum_i A_i$ and $p_{ex,i}$ is the pressure evaluated analytically from Eq. 7.38 at the same position as the center of the cell i , where we compute p_i numerically.

Fig. 7.9 shows the convergence behaviour of the L-method with the aspect ratios of 1, 2, 4 and 10. In Fig. 7.9a, the convergence rate of the cases with the permeability ratio of 1 and 5 are close to $O(h^2)$ and the case with the permeability ratio of 100 does not converge. We see a similar behavior in the discrete L^2 norm of the pressure error as we saw in Figs. 6.3 and 6.4, where considering only the polygonal grid in the well gridblock. However, for this hybrid grid system, as the permeability ratio gets far from the ideal value, $k_x/k_y = (\Delta x/\Delta y)^2$, the convergence rate diverges faster from the $O(h^2)$, compared to the case in section 6.1.3, where we only consider the polygonal part of the grid system.

A case with a given aspect ratio has the ideal permeability ratio, if

$$R \equiv \frac{\Delta x}{\Delta y} \sqrt{\frac{k_y}{k_x}} = 1. \quad (7.41)$$

The ideal permeability ratios (where $R = 1$) of the two cases shown in Figs. 7.9a and 7.9d, are 1 and 100 respectively. The case with $\Delta x/\Delta y = 100$ and $k_x/k_y = 1$ in Fig. 7.9a and the case with $\Delta x/\Delta y = 1$ and $k_x/k_y = 10$ in Fig. 7.9d have the same $R = 10$. However, the first case has a better convergence behavior compared to the other case. We showed before in Fig. 5.13 that as we increase the aspect ratio from 1 to 5, the permeability range where the L-method is guaranteed to be monotone increases from (1-5) to (6-100).

7.3 Numerical Tests for the L-method

We conduct similar tests presented in Chapter 6, on the hybrid grid refinement system. Here, 16 equal point sources are located in the grid cells of the first ring and zero Dirichlet

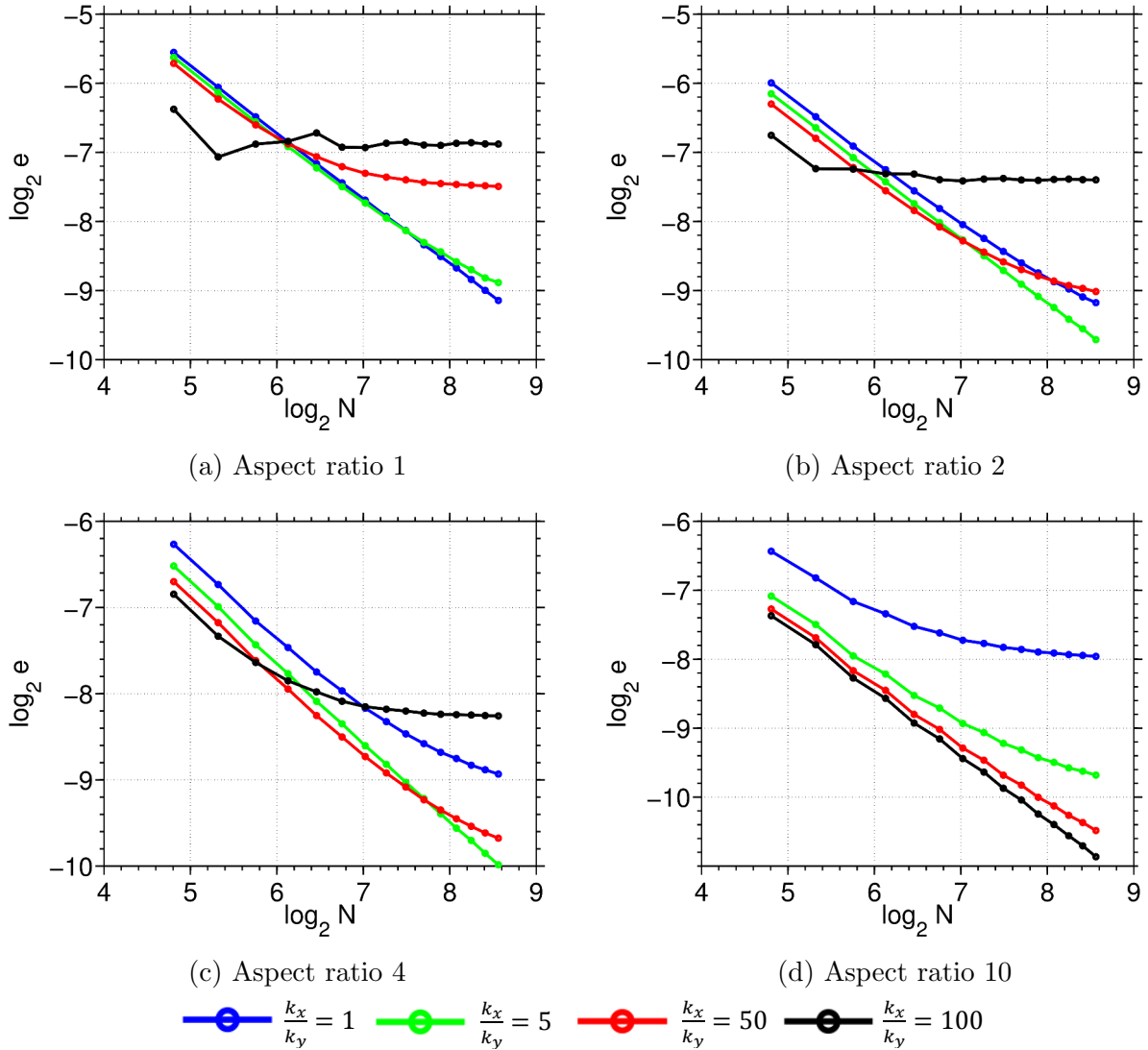


Figure 7.9: Convergence behaviour of the L-method, for various values of aspect ratio ($\Delta x/\Delta y$) and permeability ratio (k_x/k_y).

boundary conditions are imposed on the elliptical shaped boundary. Red dashed lines in Fig. 7.10 specify 16 paths emanating from the center of the inner ring of gridblocks where the sources are located. We use these paths to show how the pressure changes as the distance from the well changes. Ideally, these paths for an isotropic medium should be a set of straight lines from the center to the boundary, but this is not possible in the Cartesian refinement region, because, the paths need to go through the grid points where the pressure solution is obtained. Otherwise, it is possible that a path goes from a point with a lower pressure to a point with a higher pressure as we get far from the well, which means pressure curves

can have local minima or maxima, while the pressure solution is monotone and we don't expect to see any oscillation in the pressure solution. For cases with low heterogeneity, these paths can be chosen in such a way that regardless of the permeability ratio, they represent the pressure behavior around the well correctly. Considering the well location as the origin, the plane is divided into four quadrants by the coordinate axes, as shown in Fig. 7.10. If permeability is defined along the grid block axes, as long as the slope of the line segments in quadrants 1 and 3 are positive and in quadrants 2 and 4 are negative, the paths represent the pressure behavior correctly. This is due to the fact that in quadrants 1 and 3, the tangent at any point on any elliptical equipotential is negative, which means as long as the line segment is positive, pressure decreases along the line segment.

We plot the pressure of grid cells versus the distance from the well on a semi-log graph. For heterogeneous media, we assume that $\log(k_x)$ of each refined grid cell varies randomly based on a Gaussian distribution with the mean of 6 and the standard deviation of 1.6. Fig. 7.11 shows the pressure solutions for grid cells with the aspect ratio $\Delta x/\Delta y = 1$ and the geometric ratio $r_{i+1/2}/r_{i-1/2} = 1.3$ with different permeability ratios.

In Figs. 7.11a and 7.12c pressures at different points where have the same distance from the center are equal. However, for cases with a high permeability ratio and low aspect ratio, i.e., when $(\Delta x/\Delta y)\sqrt{k_y/k_x}$ is not close to unity, small oscillations can be seen close to the well and a one to the boundary, as shown in Figs. 7.11f and 7.12f. In Figs. 7.11c, 7.11e and 7.12e, even with a high permeability ratio, no oscillation appears in the near-well region, but we see negative potentials close to the boundaries. Results of similar cases with heterogeneities show potential oscillations close to the well region; see Figs. 7.11d, 7.11f and 7.12f. Comparing these results with the results shown in Fig. 6.5, we see similar pressure behaviors, except in regions close to the boundary. This is due to the paths we have chosen for each curve; see Fig. 7.8. Fig. 7.12 shows the pressure solutions behaviors for grid cells with the aspect ratio $\Delta x/\Delta y = 3$ and the geometric ratio $r_{i+1/2}/r_{i-1/2} = 1.3$. These results are similar to the results from the polygon part of the grid refinement system, shown in Fig. 6.6. In Fig. 7.13, we modify the aspect ratio so that $\sqrt{k_x/k_y} = \Delta x/\Delta y$, and then the pressure

solutions show no non-physical oscillations.

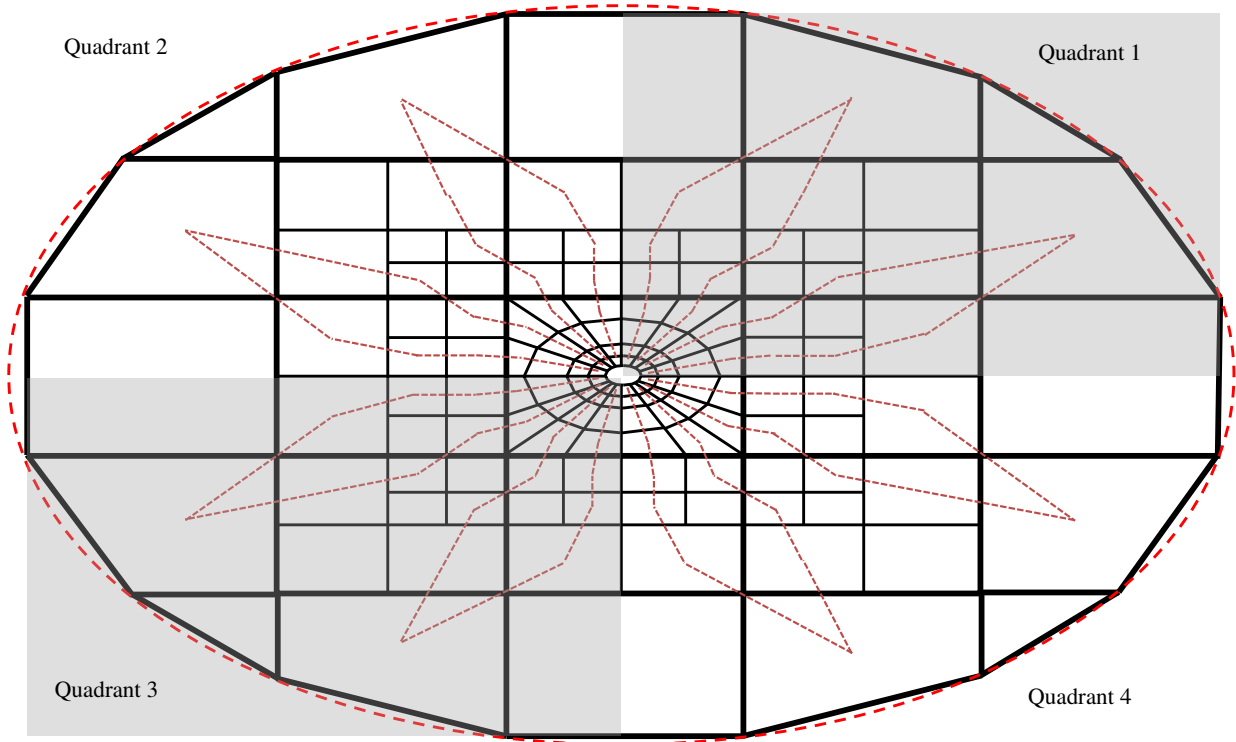


Figure 7.10: The hybrid grid system with paths emanating from the center.

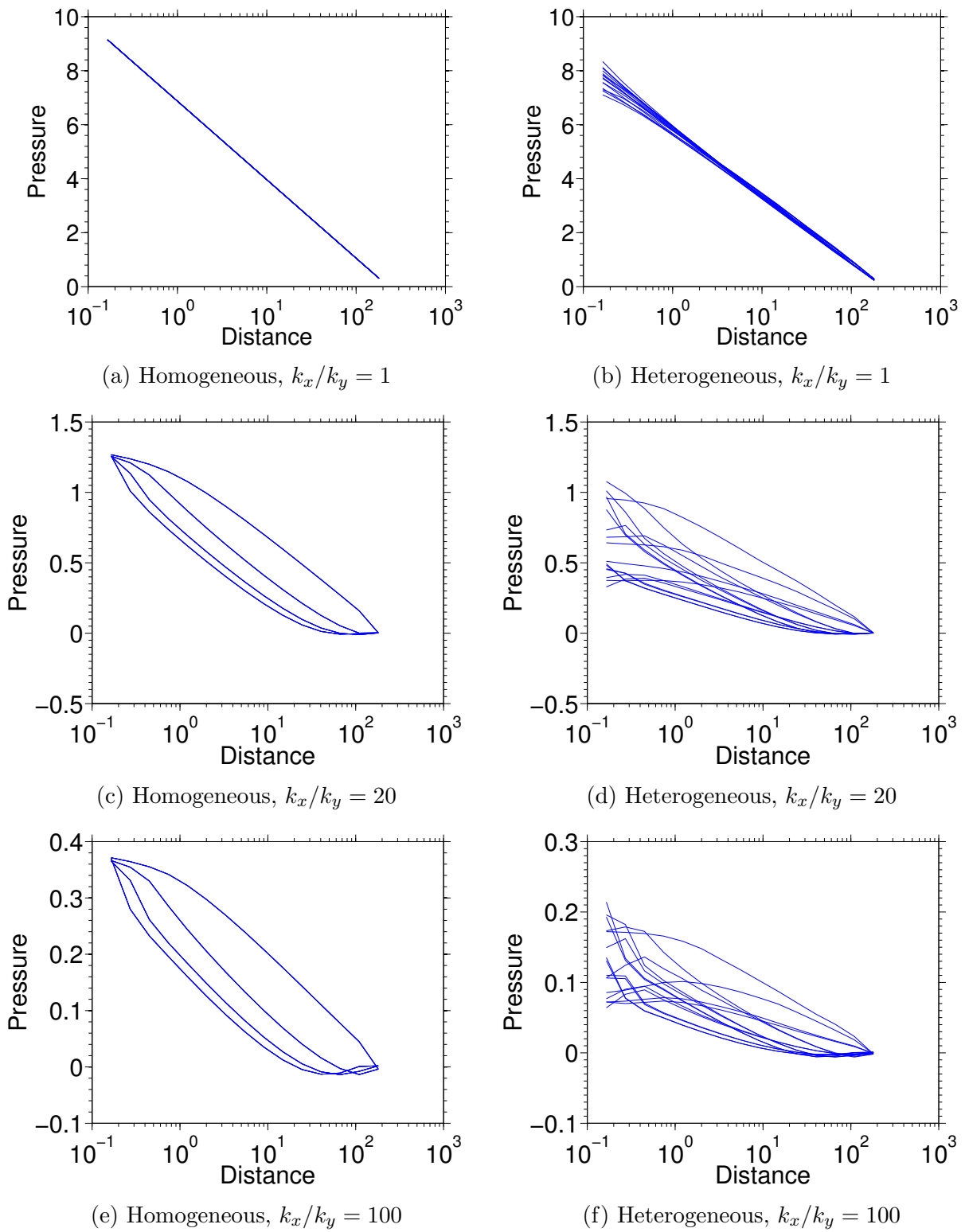


Figure 7.11: Pressure solutions for grid cells with the aspect ratio $\Delta x/\Delta y = 1$ and a geometric ratio of $\alpha = r_{i+1/2}/r_{i-1/2} = 1.3$.

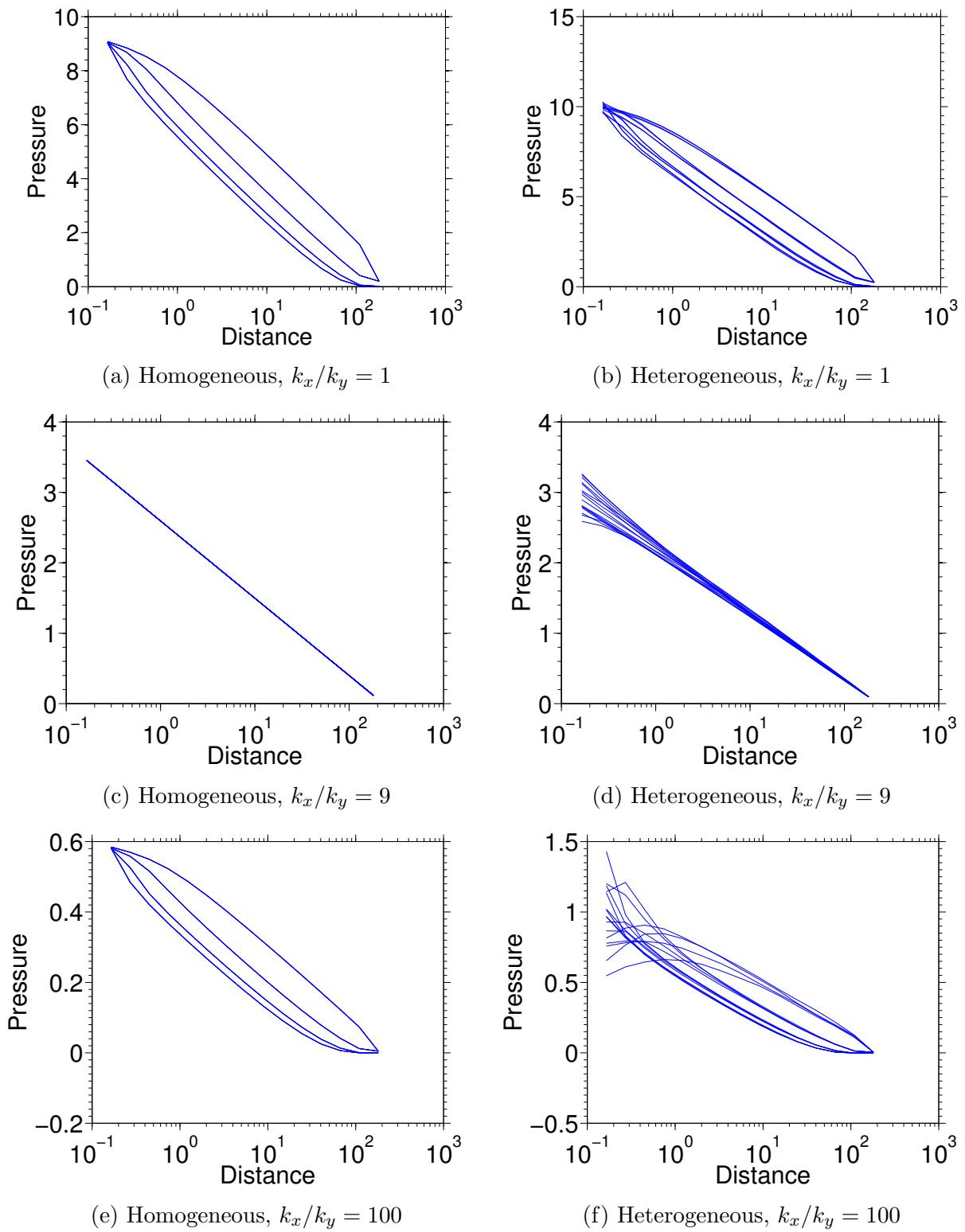
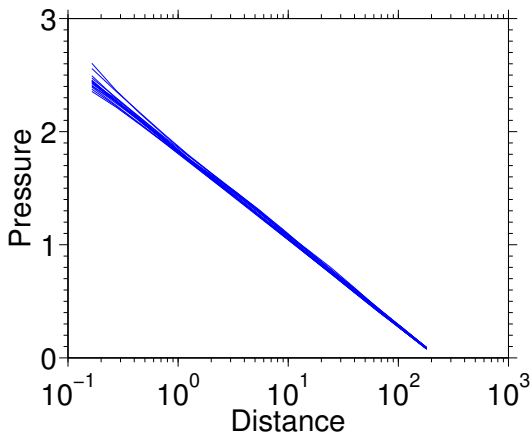
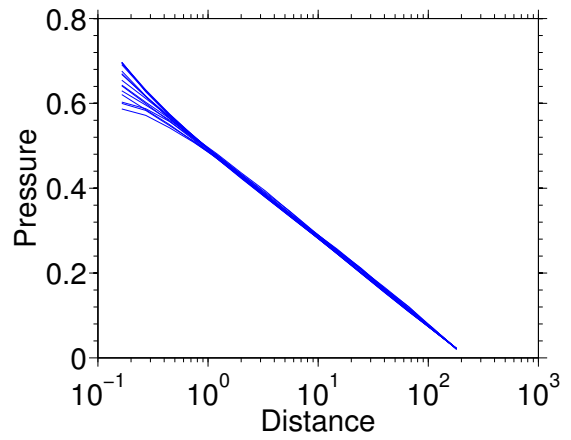


Figure 7.12: Pressure solutions for grid cells with the aspect ratio $\Delta x/\Delta y = 3$ and a geometric ratio of $\alpha = r_{i+1/2}/r_{i-1/2} = 1.3$.



(a) $\Delta x/\Delta y = 4.47, k_x/k_y = 20$



(b) $\Delta x/\Delta y = 10, k_x/k_y = 100$

Figure 7.13: Pressure solutions for grid cells of a heterogenous medium and the geometric ratio of 1.3, $\sqrt{k_x/k_y} = \Delta x/\Delta y$.

CHAPTER 8

GRID REFINEMENT ACCURACY IN WELL TESTING

8.1 Single Phase Production-Buildup

In this section, we analyze the accuracy of the proposed grid refinement method (Fig. 3.2) using a well testing example for a bounded, single-phase oil reservoir. The case pertains to a 19,000 ft \times 10,250 ft \times 100 ft reservoir with a Cartesian 19 \times 41 \times 5 uniform grid. A horizontal well of half length $l_w = 1000$ ft in the x -direction and the radius of 0.5 ft is perforated in grid cells (10, 21, 3) and (11, 21, 3). The well gridblocks are refined into 15 hexadecagonal grids in the radial direction with 16 divisions in the angular direction. Note that this refinement is in the y - z plane for the horizontal well case. The initial reservoir pressure is 2000 psi and initial water saturation is equal to irreducible water saturation given by $S_{iw} = 0.2$. The reservoir fluid is a mixture of four components with 10% carbon dioxide (CO_2), 10% methane ($C1$), 40% propane ($C3$) and 40% normal butane ($nC4$). The well is set to a constant liquid production rate of $qB = 20,000$ RB/day for 10 days followed by a two day pressure buildup test. The reservoir fluid stays single-phase liquid during the test. The case under study is a homogeneous reservoir with porosity 0.2 and $k_x = k_y = 500$ md and $k_z = 50$ md.

Δp curve is a log-log plot of Δp which is the difference between the initial reservoir pressure and the bottom hole pressure at the same datum, versus the flowing time. The $d\Delta p/d \ln t$ curve is the derivative of the pressure drop with respect to the natural logarithm of time. Following D. Bourdet et al. [10], it is calculated numerically as follows:

$$\left(\frac{d\Delta p}{d \ln t} \right)_i = \frac{t_i}{t_{i+1} - t_{i-1}} \left(\frac{\Delta p_i - \Delta p_{i-1}}{t_i - t_{i-1}} (t_{i+1} - t_i) + \frac{\Delta p_{i+1} - \Delta p_i}{t_{i+1} - t_i} (t_i - t_{i-1}) \right). \quad (8.1)$$

In the diagnostic plot of buildup data, we plot $\Delta p = p_{ws}(\Delta t) - p_{wf,s}$ and $d\Delta p/d \ln t_e$ versus shut-in time Δt . Here, t_e is Agarwal's equivalent time defined by $t_e = (t\Delta t)/(t + \Delta t)$, where t is the producing time. Throughout, $p_{ws}(\Delta t)$ denotes the shut-in pressure as a function of shut-in time, Δt , and $p_{wf,s}$ denotes the pressure at the instant of shut-in.

PA. Goode et al. [21] and A. S. Odeh et al. [32] proposed that four transient flow regimes can be observed in the pressure response of horizontal wells acting in finite reservoirs, including early radial flow, early linear flow, late pseudo-radial flow and late linear flow. After the last transient flow time period, a pseudo-steady state regime can be observed. S. Al-Rbeawi et al. [7] showed that these five regimes, are expected to develop on a drawdown test of sufficient lengths if

$$0.1 < \frac{L_w}{x_e} < 0.5, \quad (8.2)$$

$$0.1 < \frac{L_w}{y_e} \sqrt{\frac{k_y}{k_x}} < 0.5, \quad (8.3)$$

and

$$\frac{L_w}{h} \sqrt{\frac{k_z}{k_x}} \leq 20. \quad (8.4)$$

Here, L_w is half length of the horizontal well, x_e is half the distance to the boundary in the x direction, y_e is half the distance to the boundary in the y direction, h is the formation thickness, and the horizontal well is in the x direction. In this example ($L_w = 1000$ ft, $x_e = 9500$ ft, $y_e = 5,125$ ft), $\frac{L_w}{x_e} = 0.105$, $\frac{L_w}{y_e} \sqrt{\frac{k_y}{k_x}} = 0.195$, and $\frac{L_w}{h} \sqrt{\frac{k_z}{k_x}} = 3.162$. Since these values satisfy Eqs. 8.2, 8.3 and 8.4, we expect to observe all five regimes. Fig. 8.1 shows the log-log diagnostic plot of drawdown and buildup data.

All five flow regimes can be seen in the pressure derivative of drawdown data shown in Fig. 8.1, but because of producing time effect, only the first radial and first linear flow regimes are seen on the diagnostic plot of buildup data. PA Goode et al. [21] and A.S. Odeh[32] developed a set of equations to calculate the permeability values and the distance to the boundaries in the x-direction. We use the slope of Δp vs. t in a log-log plot during

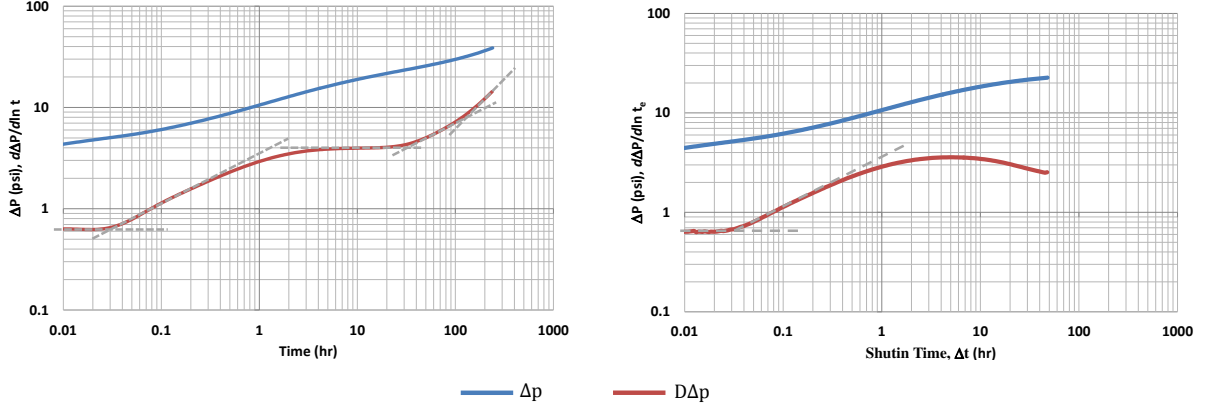


Figure 8.1: Log-log diagnostic plot of drawdown (left) and buildup (right) data.

the early radial flow regime to calculate:

$$\sqrt{k_z k_y} = \frac{70.6q\mu_o B}{k_{ro}(S_{iw})mL}, \quad (8.5)$$

where m is the value of pressure derivative during the early radial flow regime and L is length of the horizontal well. From the simulation results, $\mu_o = 0.121$ cp and $k_{ro}(S_{iw}) = 0.8$ and from the pressure derivative of drawdown data during the first radial flow regime shown in Fig. 8.1, $m = 0.67$. Thus, Eq. 8.5 gives $\sqrt{k_z k_y} = 159.4$ md, as opposed to the true value of $\sqrt{k_z k_y} = 158.1$ md.

Note that Fig. 8.1 indicates the first linear flow exists for $0.04 < t < 0.4$ or equivalently $0.2 < \sqrt{t} < 0.63$. We use the slope of Δp vs. \sqrt{t} on the Cartesian plot of Fig. 8.2 during the early linear flow regime to calculate k_y as follows:

$$\sqrt{k_y} = \frac{8.128qB}{mLh} \sqrt{\frac{\mu_o}{k_{ro}(S_{iw})\phi c_t}}. \quad (8.6)$$

From the simulation results, $c_t = 1.1 \times 10^{-5}$ 1/psi and from the slope of Δp vs. \sqrt{t} during the early linear flow in Fig. 8.2, $m=9.5$. Then, $k_y = 503$ md, and since we estimated $\sqrt{k_z k_y} = 159.4$ md, $k_z = 50.8$ md, as opposed to the true value of $k_z = 50$ md.

The slope of Δp vs. t in a log-log plot during the pseudo-radial flow regime gives

$$\sqrt{k_x k_y} = \frac{70.6q\mu_o B}{k_{ro} m h}, \quad (8.7)$$

where m is the value of pressure derivative during the pseudo-radial flow regime. From the pressure derivative of drawdown data during the pseudo-radial flow shown in Fig. 8.1, $m = 4.0$. Then, $\sqrt{k_x k_y} = 498$ md. From the previous part, we estimated $k_y = 503$ md, then, $k_x = 493$ md, as opposed to its true value of $k_x = 500$ md.

From the log-log diagnostic plot of drawdown data in Fig. 8.1 that the second linear flow period occurs for $36 < t < 100$ or equivalently $6 < \sqrt{t} < 10$ or more precisely for $6 < \sqrt{t} < 10\sqrt{\text{hr}}$, as shown in the Δp versus \sqrt{t} plot of Fig. 8.2. To calculate the distance from the well to the boundaries in the x -direction, A.S. Odeh [32], we use

$$x_e = \frac{8.128qB}{2hm} \sqrt{\frac{\mu_o}{k_y k_{ro} \phi c_t}}, \quad (8.8)$$

where, the slope of Δp vs. \sqrt{t} during the late linear flow, obtained from Fig. 8.2, is equal 1.05. Then, Eq. 8.8 gives $x_e = 9,077$ ft, where as the true value of x_e is 9,500 ft.

8.1.1 Validation with an Analytical Solution

To validate the well testing results of this example, we use the analytical solutions given by Kuchuk et al. [29]. The implementation of the analytical solutions we use here can treat both vertical and horizontal wells producing in an infinite transversely isotropic reservoir with closed top and bottom boundaries. However, the case in this example is a finite reservoir. We modify the boundaries of the case in the x and y directions by increasing the number of cells in the two directions, so that during the 10 days production and 2 days buildup, the reservoir acts as an infinite isotropic reservoir. The case pertains to a 29,000 ft \times 30,250 ft \times 100 ft reservoir with a Cartesian 29 \times 121 \times 5 uniform grid. Fluid properties, initial conditions and other properties of the reservoir are the same as in the preceding example. Fig. 8.3 compares the log-log diagnostic plot of drawdown and buildup data computed from

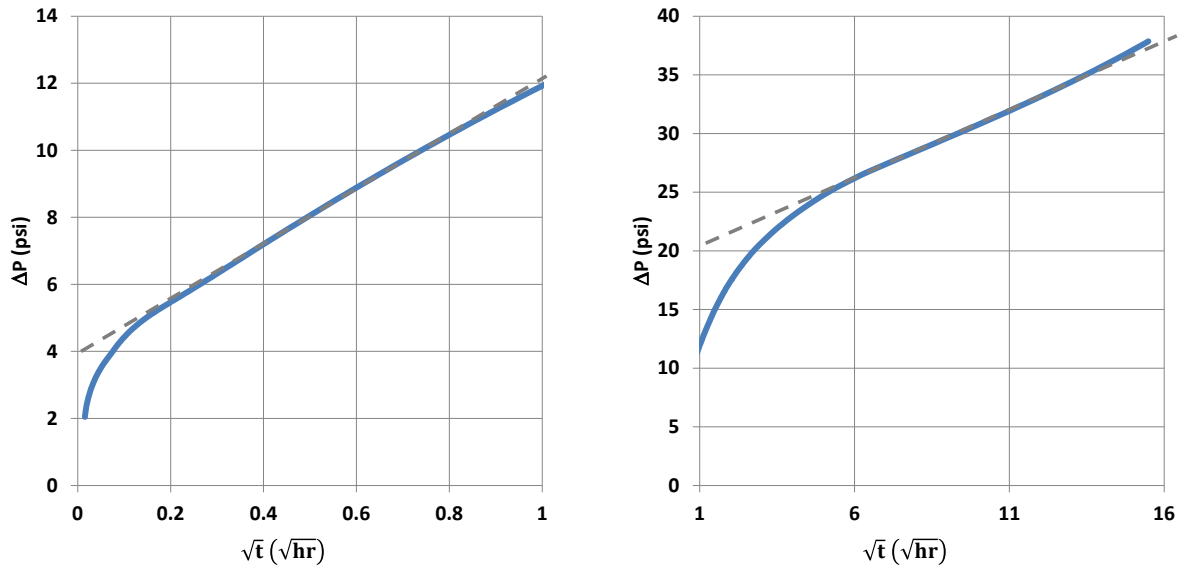


Figure 8.2: Complete drawdown period.

the results of our compositional simulator (CS) and the analytical solution. The pressure and pressure derivative in the both drawdown and buildup periods indicate that the results from our simulator and the analytical solution are in good agreement.

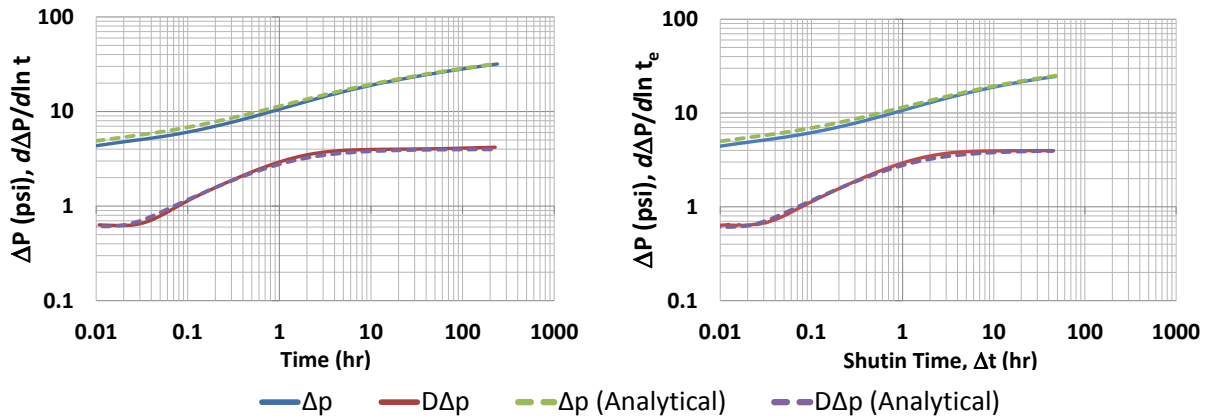


Figure 8.3: Log-log diagnostic plot of drawdown (left) and buildup (right) data.

8.2 Violation of Monotonicity

In the first example in section 8.1, the permeability ratio in the plane perpendicular to the well direction, k_y/k_z , is 10. For this example, the aspect ratio is $\Delta y/\Delta z = 12.5$ and

the geometric ratio is 1.45, so the parameters do not fall within the monotonicity range given by Fig. 5.16. (In order to be in the monotonicity region, with the geometric ratio of 1.45, the results of Fig. 5.16 indicates that $\Delta y/\Delta z$ should be between 0.15 and 6.5). However, the well-testing analysis gives accurate results without any oscillation in the pressure or pressure derivative. Also note that for a horizontal well we define

$$R \equiv \frac{\Delta z}{\Delta y} \sqrt{\frac{k_y}{k_z}}. \quad (8.9)$$

and for the example, $R = 0.25$.

In the second test, we increase the aspect ratio to 50 by decreasing the number of cells in the y-direction to 11. Fig. 8.4 shows the log-log diagnostic plot of drawdown and buildup data. Since the second test has the same reservoir properties and the production

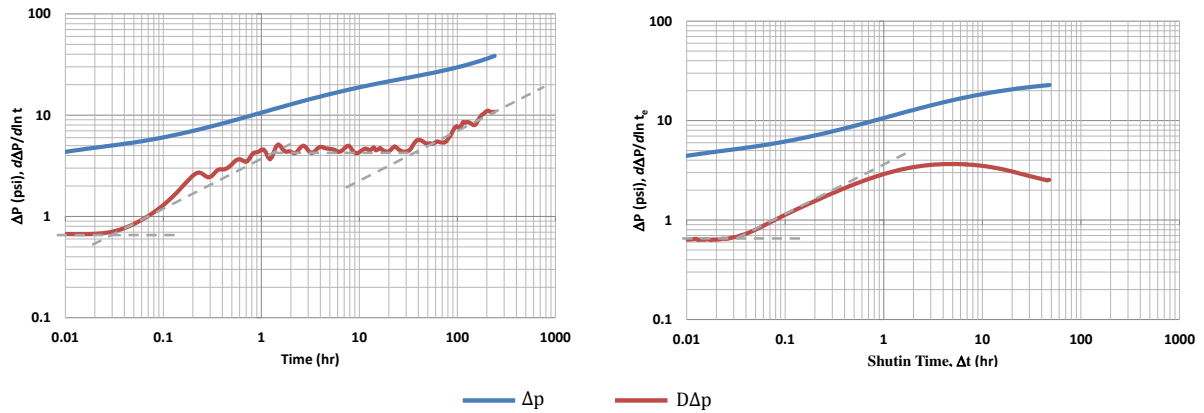


Figure 8.4: Log-log diagnostic plot of drawdown (left) and buildup (right) data.

rate as the first test, we expect to see the same welltesting results. Although, the well flowing pressure response from test 2 looks visually identical to the one from test 1, the pressure derivative curve during the drawdown period shows oscillations from 10 minutes onward. Although oscillatory behavior in the pressure derivative curve does not imply oscillations in the wellbore pressure, a further investigation revealed that there are nonphysical fluctuations in the grid cell pressures for the polygonal grid around the wellbore.

8.3 Injection-Falloff

We consider a reservoir with 500 ft length, 9150 ft width and 350 ft thickness. This model consists of a $5 \times 61 \times 7$ grid with a horizontal well located in the center of the reservoir and parallel to the shorter side, i.e., in the x -direction. The hexadecagonal grid structure is used to refine the grid cells intersected by the well. The length of the well is equal to the length of the reservoir in the x -direction, so the only flow regimes possible are early radial, linear and pseudo-steady state. The skin factor is set equal to zero. Lee-Eakin (LE) is used as the viscosity model and non-Darcy flow is not considered. the reservoir fluid at initial conditions is liquid. The initial reservoir pressure at the reference depth (7067.5 ft) is 5500 psi, the average initial water saturation is equal to irreducible water saturation given by $S_{iw} = 0.2$ and the reservoir fluid is a mixture of ten components listed in Table 8.1.

Table 8.1: The initial reservoir fluid composition at the reference depth.

Component	Mole Percent	Component	Mole Percent
N ₂	1.0194	CO ₂	0.2302
C ₁	54.8065	C ₂	8.2977
C ₃	4.4832	IC ₄	0.9975
NC ₄	2.2909	IC ₅	0.8440
NC ₅	1.2606	C ₆₊	25.7700

The reservoir fluid is liquid throughout the simulation. The case under study is divided into seven homogeneous layers with equal thicknesses (50 ft), porosity (0.2) and permeability values (100 md in the x and y directions and 10 md in the z -direction).

8.3.1 Single Phase Oil Injection

To investigate the flow regimes in a single phase fluid system, we inject oil with the same composition as the reservoir fluid, with the specified rate of $qB = 10,000$ RB/day for five days followed by a two-day pressure fall-off test. Fig. 8.5 shows the log-log diagnostic plot of oil injection and fall-off pressure data. The three flow regimes, early radial, linear and pseudo-steady state can be observed in the diagnostic plot of the injection period. We use Eq. 8.5 during the radial flow regime to estimate $\sqrt{k_y k_z}$. Here m , the slope of Δp vs. t in the log-log plot, is 15.9, $\mu_o = 0.286$ and $k_{ro}(S_{wi}) = 0.8$. Then, Eq. 8.5 gives $\sqrt{k_y k_z} = 31.55$ md, where as the true value is 31.62 md.

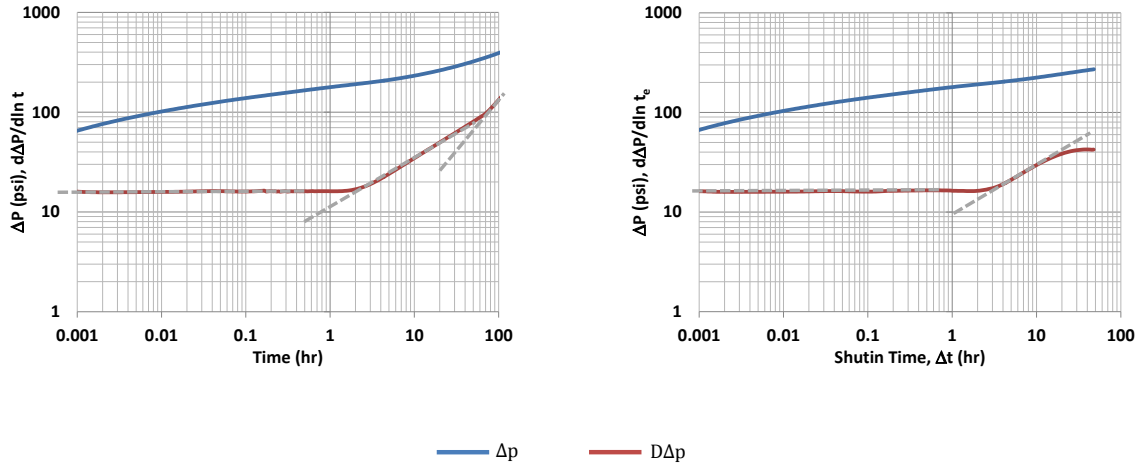


Figure 8.5: Log-log diagnostic plot of oil injection (left) and falloff (right) data, oil injection into an oil reservoir.

From the simulation results, the total compressibility is 0.73×10^{-5} 1/psi. Similar to the first example, using the slope of Δp vs. \sqrt{t} in Fig. 8.6 during the linear flow ($m = 23.14$) and Eq. 8.6, we obtain $k_y = 98.65$ md as opposed to the true value of $k_y = 100$ md.

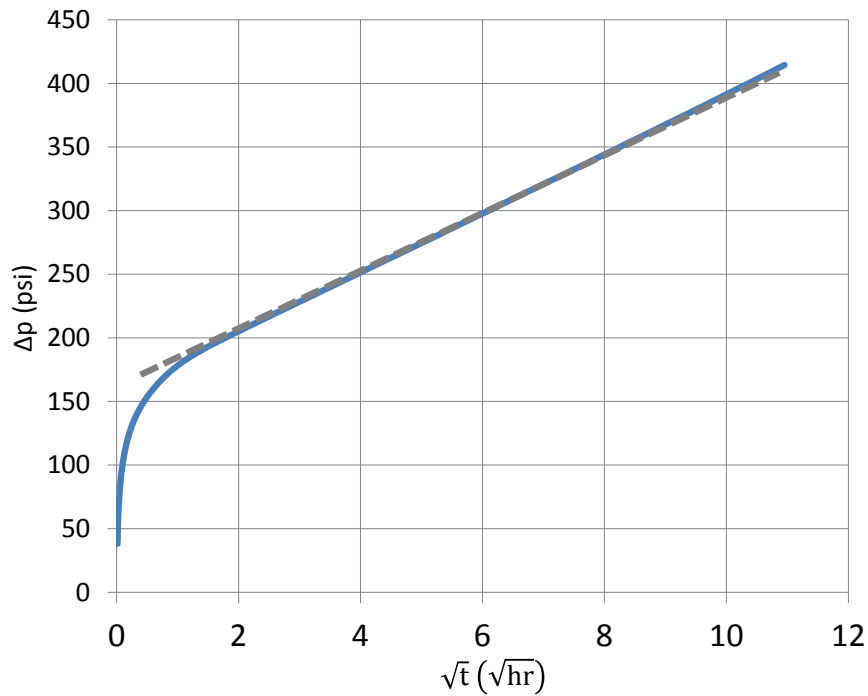


Figure 8.6: Complete oil injection period.

8.3.2 Water Injection

In this case, water is injected with the specified rate of 10,000 RB/day for five days followed by a two days pressure fall-off. Fig. 8.7 shows the log-log diagnostic plot of water injection and fall-off data. The first horizontal dashed line from the left, in the injection

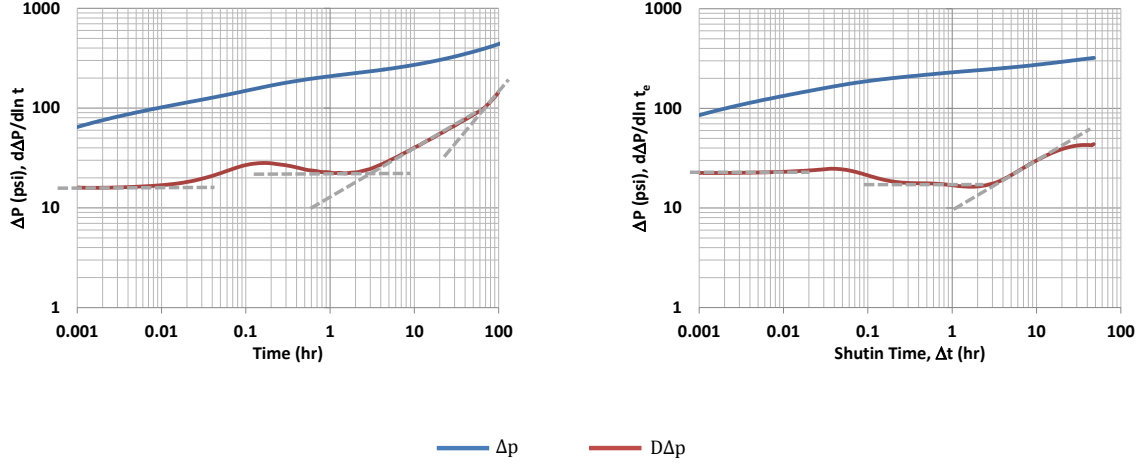


Figure 8.7: Log-log diagnostic plot of water injection (left) and falloff (right) data.

diagnostic plot in Fig. 8.7, represents the value of the pressure derivative calculated from the mobility of oil and the second horizontal line shows the pressure derivative calculated from the water mobility. From Fig. 8.7, the slope of the first horizontal dashed line is $m_1 = 14.7$ and the slope of the second horizontal line is $m_2 = 22$. Using the following equation:

$$\lambda_t \sqrt{k_x k_y} = \frac{70.6qB}{mh}, \quad (8.10)$$

if $m = m_1 = 14.7$ and $\lambda_t = \lambda_o = 2.97$ 1/cp, we estimate $\sqrt{k_y k_z} = 32.34$ md and if $m = m_2 = 22$ and $\lambda_t = \lambda_w = 2.06$ 1/cp, $\sqrt{k_y k_z} = 31.15$ md. The true value of $\sqrt{k_y k_z} = 31.62$ md.

In the fall-off plot, the first horizontal dashed line represents the value of the pressure derivative calculated from the mobility of water and the second horizontal line represents the value of the pressure derivative calculated from the mobility of oil. The dashed line with the half slope in the both injection and fall-off plots, represents the linear flow in the y -direction.

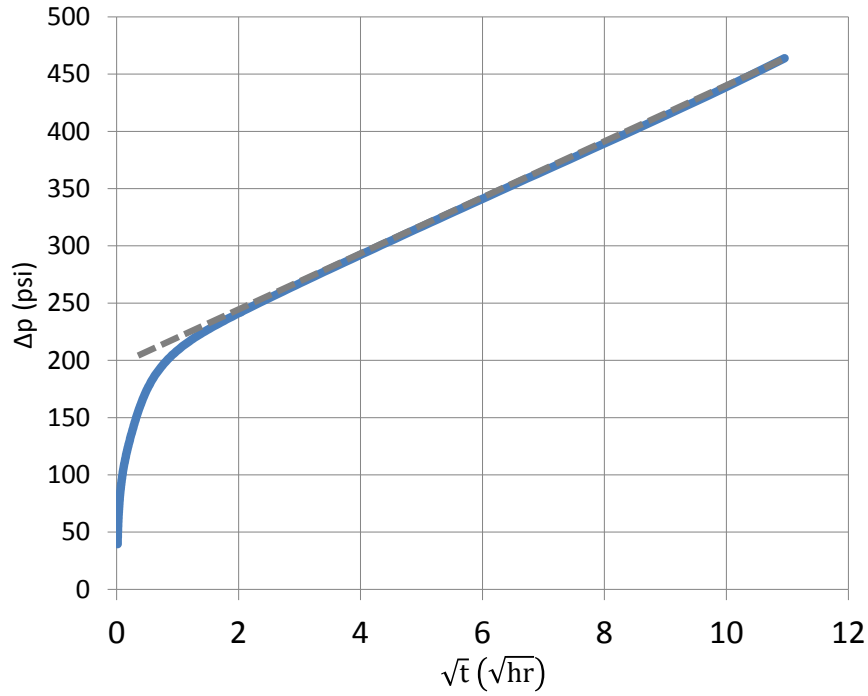


Figure 8.8: Complete water injection period.

We use the slope of Δp vs. \sqrt{t} in Fig. 8.8 during the linear flow and the true value of k_y , to compute the total mobility as follows:

$$\sqrt{\lambda_t} = \frac{8.128qB}{mLh} \sqrt{\frac{1}{k_y \phi c_t}}. \quad (8.11)$$

Here the slope of Δp vs. \sqrt{t} is $m = 24.27$ and the total compressibility is $c_t = 0.64 \times 10^{-5}$ 1/psi. Using Eq. 8.11, the total mobility is 2.81 1/cp. Note that the mobility values of oil and water are respectively equal to 2.97 1/cp and 2.06 1/cp.

As we can see in Fig. 8.7, a hump appears in the pressure derivative of injection data between 0.01 and 1 hours. Since we do not see a similar behaviour in the fall-off results, this hump is unlikely to be due to any inconsistency in transmissibility calculations. In order to investigate the behaviour, we plot the total mobility of the cells in the first ring around the well as a function of time (Fig. 8.9). As we compare this figure with the pressure derivative results of the injection data, it is clear that the hump in the derivative of injection data is

due to the varying total mobility in the first gridblock.

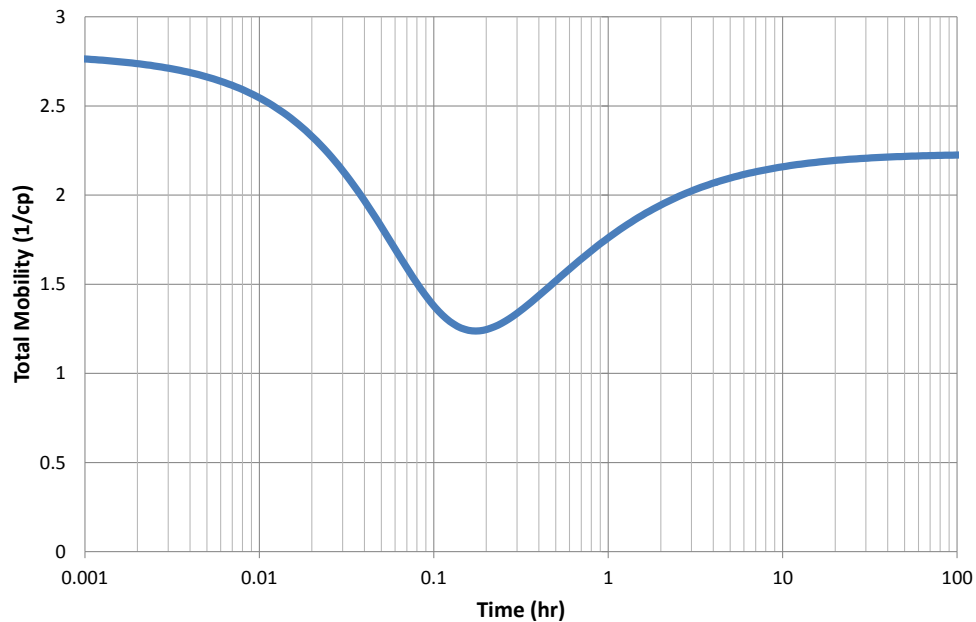


Figure 8.9: Total mobility value of the cells in the first ring around the well as a function of injection time.

8.3.3 Effect of Near-Well Cells

To remove the effect of total mobility in the first gridblock on the pressure derivative plot, we decrease the size of the grids around the well. In this case, the radius of the first 16 grid cells around the well, r_1 , is reduced from 2 ft to 0.65 ft. The number of grids in the radial direction is increased from 20 to 40. Fig. 8.10 shows the resulting log-log diagnostic plot of water injection and fall-off data. By decreasing the radius of the first 16 grid cells, the hump moves to very early times and the early radial regime represents the oil mobility. Note that the size of near-well grid cells does not affect the two radial regimes in the fall-off period and we can see both radial regimes due to the oil and water mobilities, i.e., the log-log diagnostic plots of fall-off data in Figs. 8.7 and 8.10 are identical.

8.3.4 CO_2 Injection

Consider the same reservoir as in water injection fall-off example. CO_2 gas, with

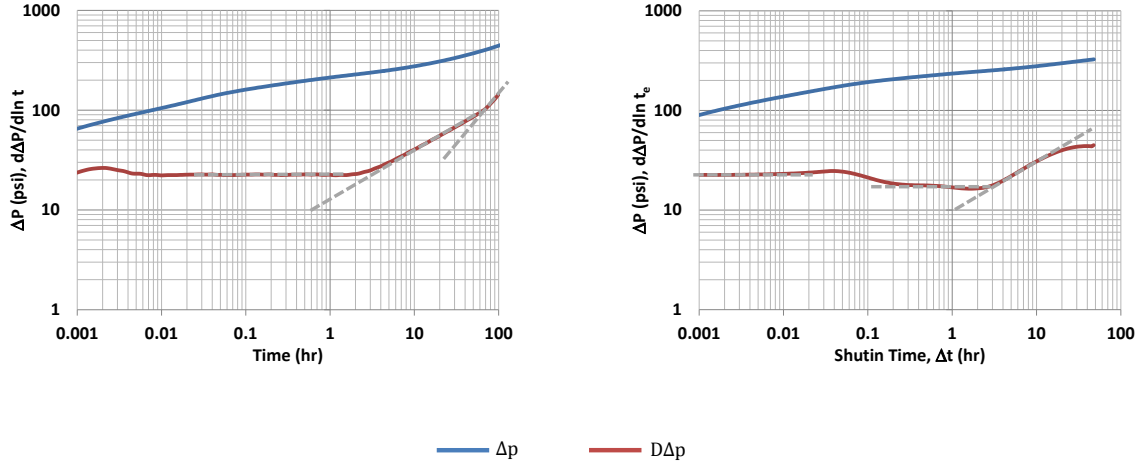


Figure 8.10: Log-log diagnostic plot of water injection (left) and falloff (right) data.

the same temperature as the reservoir temperature (100° F), is injected with the specified rate of 100,000 Mscf/day for five days followed by a two days pressure fall-off. Fig. 8.11 shows the pseudo-pressure diagnostic plot of CO₂ injection and fall-off data. Since CO₂ gas is injected into a single phase liquid reservoir, we use the CO₂ properties to compute the pseudo-pressure as follows:

$$m(p) = 2 \int_{p_b}^p \frac{p'}{\mu z} dp', \quad (8.12)$$

where p_b is an arbitrary base pressure in psi, μ is the gas viscosity in cp and the pseudo-pressure $m(p)$ is in psi²/cp. However, we do not know how pseudo pressure should be defined for this two-phase problem. The pressure derivative of the injection data is slightly oscillatory between 0.05 and 2 hours. However, these oscillations are not significant and the pressure derivative curve can be analysed without further smoothing. The falloff derivative is relatively smooth.

Assuming no skin, we conjecture the pseudo-pressure drop at the horizontal wellbore, for an injection test during early-radial flow

$$\Delta m(p) = m(p_{wf}) - m(p_i) = \frac{1637 q_{sc} T}{k_g L_w} \log \left(\frac{4t_D}{e^\gamma} \right), \quad (8.13)$$

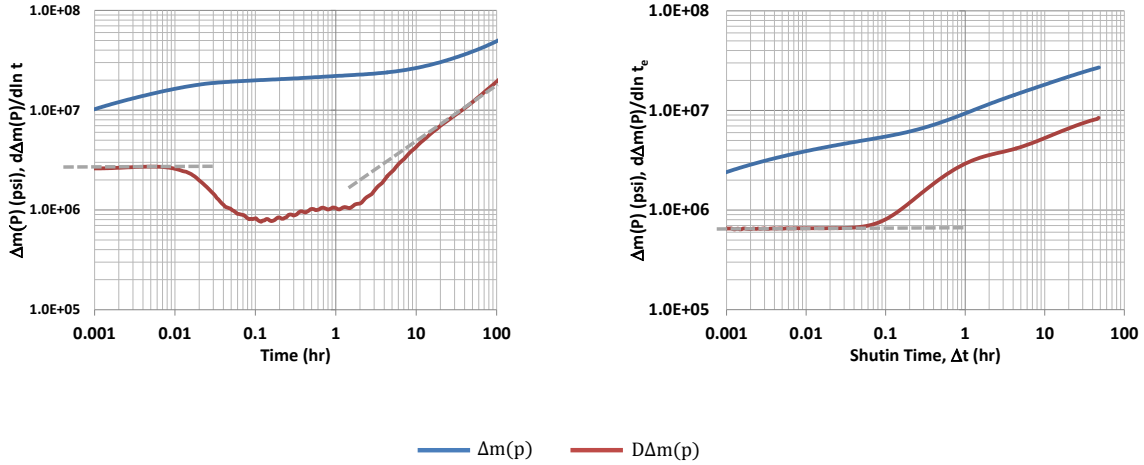


Figure 8.11: Log-log diagnostic plot of CO₂ injection (left) and falloff (right) data.

where q_{sc} is the injection rate of CO₂ in Mscf/day, T is the reservoir temperature in degree Rankine, $k_g = \sqrt{k_y k_z} k_{rg}(1 - S_{or})$ is the gas permeability in md, L_w is the wellbore length in ft, $\gamma = 0.5772$ is Euler's constant and t_D is the dimensionless time which is given by

$$t_D = \frac{2.637 \times 10^4 k_g (1 - S_{or}) t}{\mu_i c_{t_i} \phi r_w^2}, \quad (8.14)$$

where t is the injection time in hrs, μ_i is the initial viscosity of CO₂ in cp and c_{t_i} is the total compressibility at initial pressure in 1/psi. We use the slope of $\Delta m(p)$ vs. t in a semi-log plot during the early radial flow regime to compute the gas permeability as follows:

$$k_g = \frac{1637 q_{sc} T}{m L_w}. \quad (8.15)$$

From Fig. 8.12, the slope of the semi-log line $m = 7.6 \times 10^6$. In this example, the reservoir temperature is 100° F, $q_{sc} = 100$ Mscf/day and the wellbore length is 500 ft. Then, $k_g = 24.1$ md, where as $k_{rg}(S_g = 1 - S_{or}) = 0.7$, so the true value of $\sqrt{k_y k_z} = 31.6$ md.

8.3.5 Violation of Sufficient Monotonicity Criteria

Considering the grid geometry and the permeability ratio of the case under study in section 3.2, so the L-method satisfies the sufficient monotonicity criteria. We increase the

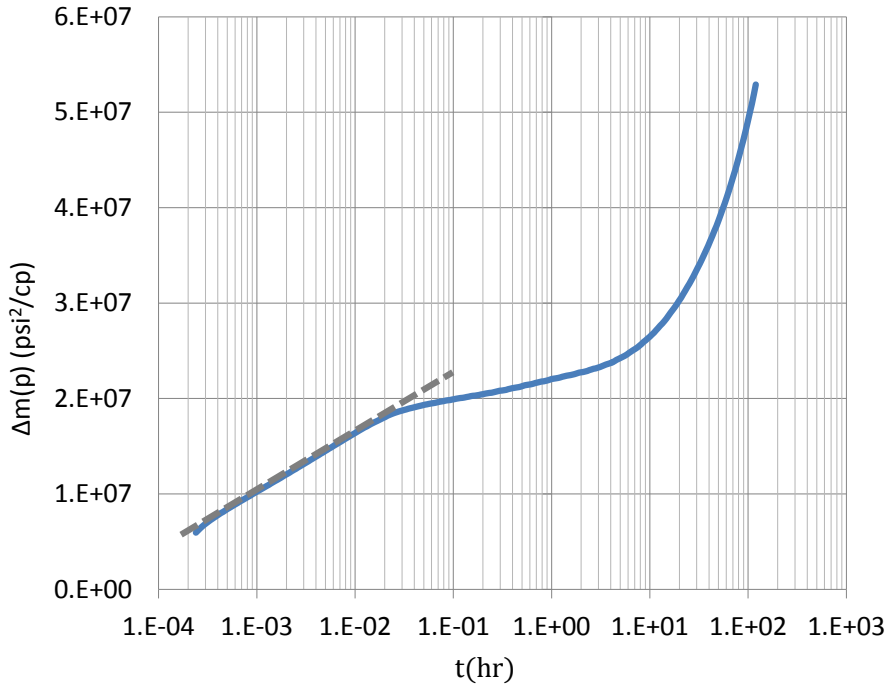


Figure 8.12: Semi-log plot - CO₂ injection.

number of cells in the y -direction to 549, so the parameters do not fall within the monotonicity range ($(\Delta z/\Delta y)\sqrt{k_y/k_z} = 9$), which from Fig. 5.16 requires that $(\Delta z/\Delta y)\sqrt{k_y/k_z} < 2.19$. We rerun the three cases, oil, water and CO₂ injections with the new grid system. The log-log diagnostic plots of the oil and water injections are almost identical to the ones in the preceding example, shown in Figs. 8.5 and 8.10. However, for the modified CO₂ injection case the reservoir simulator did not converge after 0.02 hours. We rerun the CO₂ injection case with fewer cells in the y -direction. Fig. 8.13 shows the injection and fall-off data plots for a case with the aspect ratio of $\Delta y/\Delta z = 1$. So that $(\Delta z/\Delta y)\sqrt{k_y/k_z} = 3$ and referring back to Fig. 5.16a, the parameters are still out of the monotonicity region. The pseudo-pressure derivative of the CO₂ injection data is comparable with the one in Fig. 8.11, but after 0.05 hours becomes noisy.

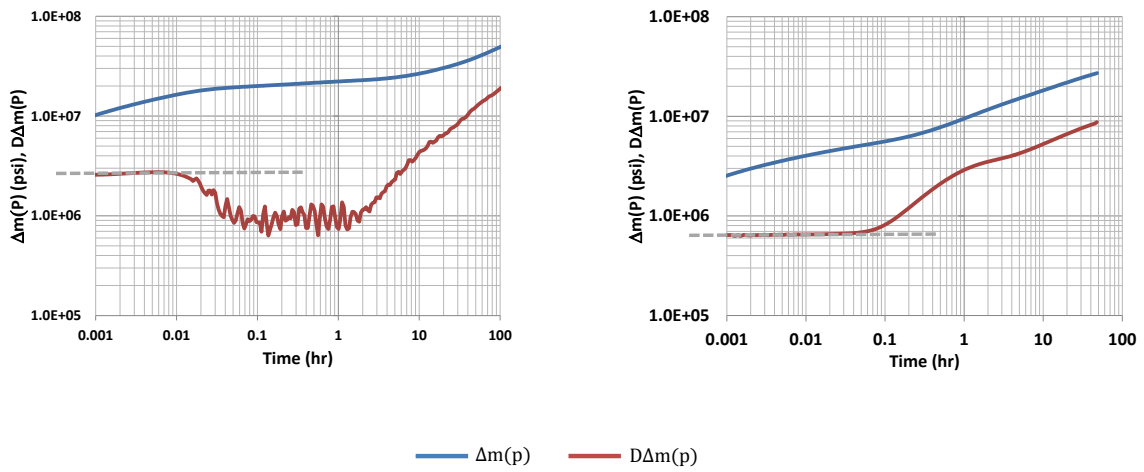


Figure 8.13: Log-log diagnostic plot of CO₂ injection (left) and falloff (right) data.

CHAPTER 9

SUMMARY AND CONCLUSIONS

In this work, we developed a new near-well grid refinement within a base coarse Cartesian grid system in order to obtain a reservoir simulator that yields solutions sufficiently accurate for well-testing purposes. Each base rectangular gridblock, penetrated by a horizontal or vertical well, is refined into a set of irregular hexadecagons and the area between each two adjacent hexadecagons is divided into 16 trapezoidal grids. Each rectangular gridblock adjacent to a well gridblock is refined into a set of rectangular grids. The structure of hexadecagonal grids is adjusted based on the near-well elliptical flow pattern to simulate the flow behavior more accurately. The grid is able to accurately reflect radial or elliptical flow in the near wellbore without causing the inconsistency in the pressure solutions that occurs when an r - θ refinement in the well gridblock is employed.

We provided sufficient monotonicity conditions for the MPFA methods for our hexadecagonal based gridding scheme for both the O and L methods. We investigated the monotonicity regions of the L-method as functions of permeability anisotropy and grid geometry properties, including the aspect ratio.

Given any aspect ratio, the L-method satisfies the sufficient monotonicity conditions for a wide range of the geometric and permeability ratios than does the O-method. The largest range of geometric values for which the monotonicity holds is obtained when $(\Delta y/\Delta x) \sqrt{k_x/k_y}$ (vertical well) or $(\Delta y/\Delta z) \sqrt{k_z/k_y}$ (horizontal well) is equal to unity, when the axis of the horizontal well is always parallel to the x -axis.

For any aspect ratio, the geometric ratio of 1.4 has the largest monotonicity range, when there is no skin zone, but the presence of a skin zone causes a slight increase in the optimal value of the geometric ratio.

The skin zone around the well decreases the monotonicity regions for MPFA method, including the L-method. However, the skin zone does not have a significant effect on the monotonicity regions when the aspect ratio is close to the square root of permeability ratio.

Our numerical results showed that if a case is out of the monotonicity region but not far from the region, solutions show no non-physical behavior, i.e., exhibit the behavior of a monotone scheme.

By comparing results from our simulator with results based on an analytical solution for horizontal well, we show that our simulator can yield sufficiently accurate solutions so that the simulator based on MPFA can be used as a forward model when analyzing well-test pressure data by nonlinear regression analysis.

BIBLIOGRAPHY

- [1] I Aavatsmark, T Barkve, Ø Bøe, and T Mannseth. Discretization on non-orthogonal, curvilinear grids for multi-phase flow. In *ECMOR IV-4th European Conference on the Mathematics of Oil Recovery*, 1994.
- [2] I. Aavatsmark, T. Barkve, O. Boe, and T. Mannseth. Discretization on unstructured grids for inhomogeneous, anisotropic media. part i: Derivation of the methods. *SIAM Journal on Scientific Computing*, 19(5):1700–1716, September 1998.
- [3] I. Aavatsmark, T. Barkve, O. Bøe, and T. Mannseth. Discretization on unstructured grids for inhomogeneous, anisotropic media. part ii: Discussion and numerical results. *SIAM Journal on Scientific Computing*, 19(5):1717–1736, 1998.
- [4] I. Aavatsmark and G.T. Eigestad. Numerical convergence of the MPFA O-method and U-method for general quadrilateral grids. *International journal for numerical methods in fluids*, 51(9-10):939–961, 2006.
- [5] I. Aavatsmark, G.T. Eigestad, and R.A. Klausen. Numerical convergence of the MPFA O-method for general quadrilateral grids in two and three dimensions. In *Compatible spatial discretizations*, pages 1–21. Springer, 2006.
- [6] I. Aavatsmark, G.T. Eigestad, B.T. Mallison, and J.M. Nordbotten. A compact multipoint flux approximation method with improved robustness. *Numerical Methods for Partial Differential Equations*, 24(5):1329–1360, 2008.
- [7] Salam Jabbar Hussain Al Rbeawi and Djebbar Tiab. Transient Pressure Analysis of Horizontal Wells in a Multi-Boundary System. In *SPE Production and Operations Symposium*. Society of Petroleum Engineers, 2011.

- [8] Khalid Aziz and Antonin Settari. A new iterative method for solving reservoir simulation equations. *Journal of Canadian Petroleum Technology*, 11(01), 1972.
- [9] Khalid Aziz and Antonin Settari. *Petroleum reservoir simulation*. Chapman & Hall, 1979.
- [10] Dominique Bourdet, J.A. Ayoub, and Y.M. Pirard. Use of pressure derivative in well test interpretation. *SPE Formation Evaluation*, 4(02):293–302, 1989.
- [11] Qian-Yong Chen, Jing Wan, Yahan Yang, and Rick T Miffin. Enriched multi-point flux approximation for general grids. *Journal of Computational Physics*, 227(3):1701–1721, 2008.
- [12] Tianhong Chen. *New Methods for Accurate Upscaling with Full-Tensor Effects*. PhD thesis, Stanford University, Stanford, California, USA, 2009.
- [13] M.C.H. Chien, S.T. Lee, and W.H. Chen. A new fully implicit compositional simulator. In *Proceedings of SPE Reservoir Simulation Symposium, 10-13 February 1985, Dallas, Texas*, 1985.
- [14] Michael G Edwards and Clive F Rogers. A flux continuous scheme for the full tensor pressure equation. In *ECMOR IV-4th European Conference on the Mathematics of Oil Recovery*, 1994.
- [15] Michael G Edwards and Clive F Rogers. Finite volume discretization with imposed flux continuity for the general tensor pressure equation. *Computational Geosciences*, 2(4):259–290, 1998.
- [16] Michael G Edwards and Hongwen Zheng. A quasi-positive family of continuous darcy-flux finite-volume schemes with full pressure support. *Journal of Computational Physics*, 227(22):9333–9364, 2008.

- [17] Michael G Edwards and Hongwen Zheng. Double-families of quasi-positive darcy-flux approximations with highly anisotropic tensors on structured and unstructured grids. *Journal of Computational Physics*, 229(3):594–625, 2010.
- [18] Richard E Ewing, BA Boyett, DK Babu, and RF Heinemann. Efficient use of locally refined grids for multiphase reservoir simulation. In *SPE Symposium on Reservoir Simulation*. Society of Petroleum Engineers, 1989.
- [19] P. Forchheimer. Wasserbewegung Durch Boden. *Zeitschrift des Vereines Deutscher Ingenieure*, 45(1781), 1901.
- [20] Fahim Forouzanfar, Adolfo P Pires, Albert C Reynolds, et al. Formulation of a transient multi-phase thermal compositional wellbore model and its coupling with a thermal compositional reservoir simulator. In *SPE Annual Technical Conference and Exhibition*. Society of Petroleum Engineers, 2015.
- [21] PA Goode et al. Pressure drawdown and buildup analysis of horizontal wells in anisotropic media. *SPE Formation Evaluation*, 2(04):683–697, 1987.
- [22] D Gunasekera, J Cox, P Lindsey, et al. The generation and application of k-orthogonal grid systems. In *SPE Reservoir Simulation Symposium*. Society of Petroleum Engineers, 1997.
- [23] Z.E. Heinemann, C.W. Brand, Margit Munka, and Y.M. Chen. Modeling reservoir geometry with irregular grids. *SPE Reservoir Engineering*, 6(02):225–232, 1991.
- [24] Bernd Heinrich. *Finite difference methods on irregular networks*. Springer, 1987.
- [25] Eberhard Hopf, Cathleen S Morawetz, James Serrin, and I.G. Sina. *Selected Works of Eberhard Hopf: With Commentaries*, volume 17. American Mathematical Soc., 2002.
- [26] IMEX. *Users Guide*. Computer Modelling Group Ltd., 2010.

- [27] Eirik Keilegavlen and Ivar Aavatsmark. Monotonicity for MPFA methods on triangular grids. *Computational Geosciences*, 15(1):3–16, 2011.
- [28] Eirik Keilegavlen, Jan M. Nordbotten, and Ivar Aavatsmark. Sufficient criteria are necessary for monotone control volume methods. *Applied Mathematics Letters*, 22(8):1178–1180, 2009.
- [29] FJ Kuchuk et al. Pressure behavior of horizontal wells in multilayer reservoirs with crossflow. *SPE Formation Evaluation*, 11(01):55–64, 1996.
- [30] Sissel Slettemark Mundal, Eirik Keilegavlen, and Ivar Aavatsmark. Simulation of anisotropic heterogeneous near-well flow using mpfa methods on flexible grids. *Computational Geosciences*, 14(4):509–525, 2010.
- [31] J.M. Nordbotten, I. Aavatsmark, and G.T. Eigestad. Monotonicity of control volume methods. *Numerische Mathematik*, 106(2):255–288, 2007.
- [32] Aziz S Odeh, DK Babu, et al. Transient flow behavior of horizontal wells, pressure draw-down, and buildup analysis. In *SPE California Regional Meeting*. Society of Petroleum Engineers, 1989.
- [33] Donald W Peaceman et al. Interpretation of well-block pressures in numerical reservoir simulation (includes associated paper 6988). *Society of Petroleum Engineers Journal*, 18(03):183–194, 1978.
- [34] Donald W Peaceman et al. Interpretation of well-block pressures in numerical reservoir simulation with nonsquare grid blocks and anisotropic permeability. *Society of Petroleum Engineers Journal*, 23(03):531–543, 1983.
- [35] Oswaldo A. Pedrosa. *Use of a Hybrid Grid in Reservoir Simulation*. PhD thesis, Stanford University, Stanford, California, USA, 1985.
- [36] Oswaldo A. Pedrosa and Khalid Aziz. Use of a hybrid grid in reservoir simulation. *SPE Reservoir Engineering*, 1(6):611–621, 1986.

- [37] George D. Poole. Generalized M-matrices and applications. *Mathematics of Computation*, 29(131):903–910, 1975.
- [38] Schlumberger. ECLIPSE reservoir simulation software: Reference manual. *Schlumberger Software, London, UK*, 2011.
- [39] Richard S Varga. On a discrete maximum principle. *SIAM Journal on Numerical Analysis*, 3(2):355–359, 1966.
- [40] Markus Wolff, Yufei Cao, Bernd Flemisch, Rainer Helmig, and Barbara Wohlmuth. Multi-point flux approximation l-method in 3d: numerical convergence and application to two-phase flow through porous media. *Radon Ser. Comput. Appl. Math., De Gruyter*, 12:39–80, 2013.

APPENDIX A
SOLUTION ON LAPLACE'S EQUATION

Since we assume that the fluid is incompressible, the flow across any circumference is constant. We integrate the normal velocity around an elliptical isobar to determine the flow rate. Following [34],

$$q = -h \int_{\rho} (v \cdot n) ds, \quad (\text{A.1})$$

where, h is the reservoir thickness, v is the fluid velocity, n is the unit normal to the ellipse and s is the arc length around the ellipse. Here, n and s are in the x - y plane. ρ for each ellipse is constant, then,

$$q = -h \int_0^{2\pi} (v \cdot n) \left(\frac{\partial s}{\partial \theta} \right)_{\rho} d\theta. \quad (\text{A.2})$$

If we define β as the angle between vector n and the x -axis, then $n = [\cos \beta, \sin \beta]$, and

$$v \cdot n = v_x \cos \beta + v_y \sin \beta, \quad (\text{A.3})$$

We compute v_x and v_y using Darcy's Law, as follows:

$$v_x = -\frac{k_x}{\mu} \left(\frac{\partial p}{\partial x} \right)_y, \quad (\text{A.4})$$

where,

$$\left(\frac{\partial p}{\partial x} \right)_y = \left(\frac{\partial p}{\partial \rho} \right)_{\theta} \left(\frac{\partial \rho}{\partial x} \right)_y + \left(\frac{\partial p}{\partial \theta} \right)_{\rho} \left(\frac{\partial \theta}{\partial x} \right)_y \quad (\text{A.5})$$

From Eq. 6.30, $(\partial p / \partial \rho)_{\theta} = C$ and since pressure on each ellipse is constant, $(\partial p / \partial \theta)_{\rho} = 0$.

We substitute Eqs. 6.22 and 6.23 into Pythagorean trigonometric identity and combine it

with Eqs 6.15 and 6.16 to have:

$$\frac{x^2(k_y/k_x)^{1/2}}{b^2 \sinh^2 \rho} + \frac{y^2(k_x/k_y)^{1/2}}{b^2 \cosh^2 \rho} = 1. \quad (\text{A.6})$$

By differentiating both sides of the equation with respect to x , we have:

$$\sqrt{\frac{k_y}{k_x}} \frac{x \sinh \rho - x^2 \cosh \rho (\partial \rho / \partial x)_y}{\sinh^4 \rho} - \sqrt{\frac{k_x}{k_y}} \frac{y^2 \cosh \rho (\partial \rho / \partial x)_y}{\cosh^4 \rho} = 0, \quad (\text{A.7})$$

and it would simplified to

$$\left(\frac{\partial \rho}{\partial x} \right)_y = \frac{x}{\frac{x^2 \cosh \rho}{\sinh \rho} + \frac{k_x y^2 \sinh^3 \rho}{k_y \cosh^3 \rho}}. \quad (\text{A.8})$$

After Eqs. 6.15, 6.16, 6.22 and 6.23 are inserted into Eq. A.8, we get

$$\left(\frac{\partial \rho}{\partial x} \right)_y = \frac{1}{b} \frac{(k_y/k_x)^{1/4} \cosh \rho \sin \theta}{\sin^2 \theta + \sinh^2 \rho}. \quad (\text{A.9})$$

By substituting Eqs. A.5 and A.9 into Eq. A.4, we get

$$v_x = -\frac{C k_x (k_y/k_x)^{1/4} \cosh \rho \sin \theta}{\mu b (\sin^2 \rho + \sin^2 \theta)} \quad (\text{A.10})$$

and similarly,

$$v_y = -\frac{C k_y (k_x/k_y)^{1/4} \sinh \rho \cos \theta}{\mu b (\cosh^2 \rho - \cos^2 \theta)} \quad (\text{A.11})$$

We compute β from the following equation.

$$\tan \beta = -\left(\frac{\partial x}{\partial y} \right)_\rho = -\left(\frac{\partial x}{\partial \theta} \right)_\rho / \left(\frac{\partial y}{\partial \theta} \right)_\rho, \quad (\text{A.12})$$

where, from Eqs. 6.15 and 6.22,

$$\left(\frac{\partial x}{\partial \theta} \right)_\rho = \frac{dx}{du} \left(\frac{\partial u}{\partial \theta} \right)_\rho = (k_x/k_y)^{1/4} b \sinh \rho \cos \theta, \quad (\text{A.13})$$

and, from Eqs. 6.16 and 6.23,

$$\left(\frac{\partial y}{\partial \theta}\right)_\rho = \frac{dy}{dv} \left(\frac{\partial v}{\partial \theta}\right)_\rho = -(k_y/k_x)^{1/4} b \cosh \rho \sin \theta. \quad (\text{A.14})$$

So, substitution of Eqs. A.13 and A.14 into Eq. A.12 yield

$$\tan \beta = - \left(\frac{k_x}{k_y}\right)^{1/2} \frac{\tanh \rho}{\tan \theta}. \quad (\text{A.15})$$

Substitution of expressions for v_x , v_y and β into Eq. A.3 then gives

$$v \cdot n = \frac{(k_x k_y)^{3/4} C / \mu b}{(k_y \cosh^2 \rho \sin^2 \theta + k_x \sinh^2 \rho \cos^2 \theta)^{1/2}} \quad (\text{A.16})$$

$\left(\frac{\partial s}{\partial \theta}\right)_\rho$ can be written as

$$\left(\frac{\partial s}{\partial \theta}\right)_\rho = \sqrt{\left(\frac{\partial x}{\partial \theta}\right)_\rho^2 + \left(\frac{\partial y}{\partial \theta}\right)_\rho^2}, \quad (\text{A.17})$$

and substitution of Eqs. A.13 and A.14 gives

$$\left(\frac{\partial s}{\partial \theta}\right)_\rho = b \sqrt{(k_x/k_y)^{1/2} \sinh^2 \rho \cos^2 \theta + (k_y/k_x)^{1/2} \cosh^2 \rho \sin^2 \theta}, \quad (\text{A.18})$$

By combining Eqs. A.16 and A.18, we have

$$(v \cdot n) \left(\frac{\partial s}{\partial \theta}\right)_\rho = \frac{C(k_x k_y)^{1/2}}{\mu}. \quad (\text{A.19})$$

Finally,

$$q = \frac{2\pi h(k_x k_y)^{1/2} C}{\mu}. \quad (\text{A.20})$$

So,

$$C = \frac{q\mu}{2\pi h(k_x k_y)^{1/2}}. \quad (\text{A.21})$$